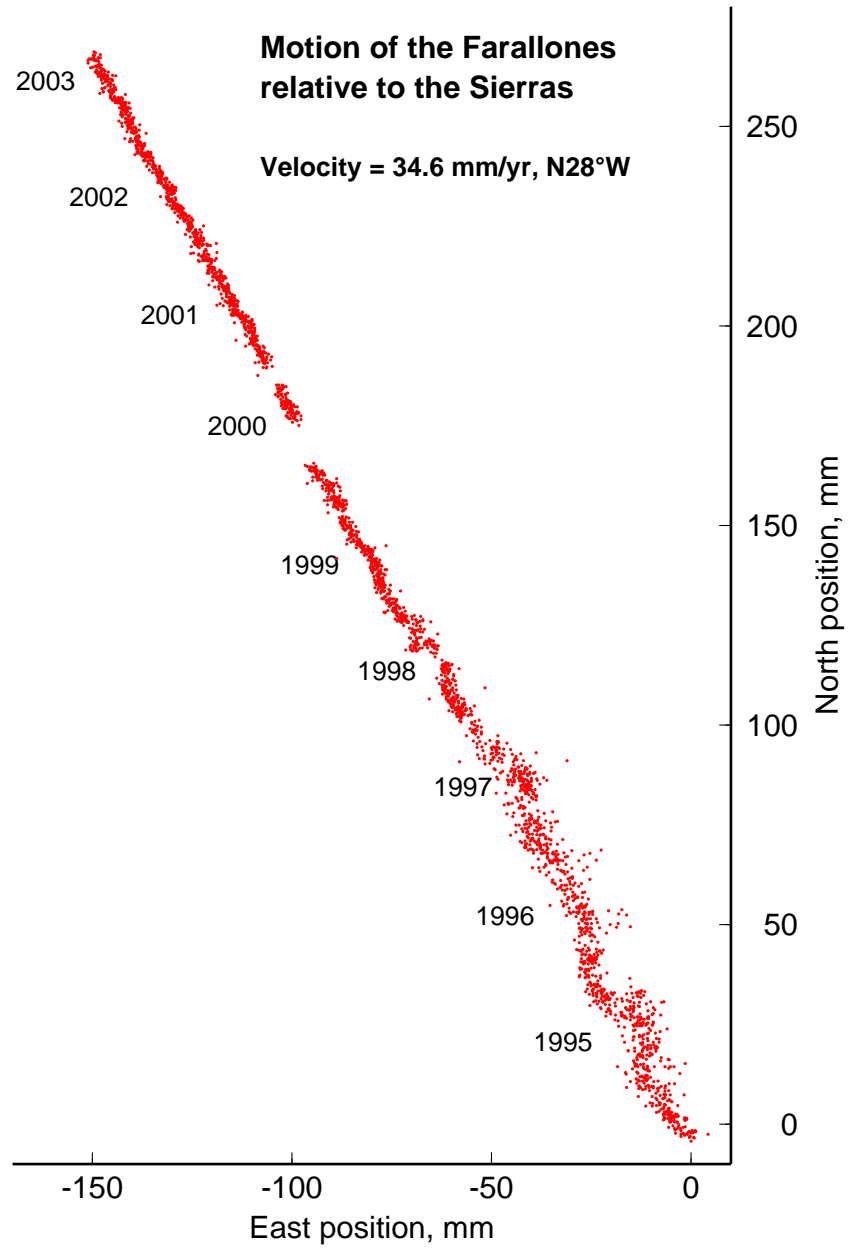


Part III  
Ongoing Research Projects



## Chapter 13

# Finite Source Modeling of Great Earthquakes

Douglas Dreger

### 0.1 Introduction

The  $M_w$  7.9 Denali fault, Alaska, earthquake, which occurred on November 03, 2002 at 22:12:41.0 UTC initiated on the north dipping Susitna Glacier fault with a reverse sense of motion that apparently triggered primarily strike-slip faulting over approximately 300 km of the Denali-Totschunda fault system (*Eberhart-Phillips et al.*, 2003). This complex fault geometry is similar in many respects to that of the San Andreas fault system, and therefore the study of this great earthquake provides needed insight into processes by which earthquakes may grow into large, multi-segmented ruptures involving complex fault geometries. Central to such study is a detailed analysis of the kinematic source process, and investigation of dynamic rupture models to obtain insight into the complex fault interaction. Teaming with Professor Oglesby (UCR), and Drs. Harris (USGS Menlo Park), Ratchkovski (UA, Fairbanks), and Hansen (UA, Fairbanks) we investigate the connection between the Denali rupture kinematics and the dynamic source process. This work has been submitted for publication in GRL (*Dreger et al.*, 2003).

### 0.2 Kinematic Source Modeling

Three data sets were employed to constrain the kinematic rupture process: observed surface offsets reported by the Denali Earthquake Field Geology Team (*Eberhart-Phillips et al.*, 2003), continuous and campaign-mode GPS data (*Hreinsdóttir et al.*, 2003), and local and regional distance seismic waveforms. The seismic data from 8 recorders, operated by several groups (e.g. US Geological Survey, the University of Alaska, Fairbanks, and the Alyeska Corporation) provide control on the spatial and temporal pattern of mainshock slip. The seismic station coverage is sparse necessitating the use of GPS data from

38 stations from the continuous Alaska Deformation Array and campaign-mode collections.

The 5-segment fault geometry used for the inversion accounts for the arcuate structure of the Denali-Totschunda fault system (Figure 13.1a), as well as the north-dipping structure of the Susitna Glacier fault, which was identified as the initial rupture plane based on a oblique-reverse first motion focal mechanism obtained by the Alaska Earthquake Information Center. The strike and dip of segment 1, representing the Susitna Glacier fault, was 262 and 48 degrees, respectively. The strikes of segments 2-5 were 83, 102, 117, and 143 all with 90 degree dip since relocated aftershocks do not clearly delineate a non-vertical dip. Each fault segment of the model has a width of 30 km, and the lengths of segments 1-5 are 30, 30, 50, 136, and 100 km, respectively. Segments 1 and 2 share a common hypocenter located at 63.520 N, 147.530 W, and a depth of 7.5 km, and they spatially overlap.

The inversion method that we used is based on the multiple time window approach of *Hartzell and Heaton* (1983). Each of the fault segments was discretized by 3.75 km by 3.75 km subfaults. We applied slip positivity, moment minimization, and Laplacian smoothing constraints (e.g. *Kaverina et al.*, 2002), and allow for spatially variable rake. The slip rise time was taken to be 2 seconds. Three time windows, each overlapping by 1 second, were employed allowing the slip rise time to vary between 2 to 4 seconds.

The seismic data were corrected for instrument response, integrated to displacement, and bandpass filtered using a two-pass, fourth-order Butterworth filter with corners of 0.01 and 0.5 Hz, and then resampled to 2 sps. GPS displacements processed and distributed by *Hreinsdóttir et al.* (2003) were used.

Seismic Green's functions were computed using a velocity model from *Ratchkovski and Hansen* (2002), which is appropriate for the region using a frequency-wavenumber integration approach. Green's functions for the GPS data were computed for a half-space elastic structure using the method of *Okada* (1985), assuming a

shear elastic stiffness of  $3.52 \times 10^{10}$  Pa, which corresponds to the value at 8 km depth in the velocity model used to compute the seismic Green's functions.

It was possible to fit the GPS and seismic data sets quite well with respective variance reductions of 99.4% and 44.3%. The preferred slip model is shown in Figure 13.1b. The slip on Susitna Glacier fault (S1) is confined to depths less than the intersection depth (7.5 km) with the vertical Denali fault. The slip on this portion of the fault sums to a seismic moment of  $3.12 \times 10^{19}$  Nm equivalent to  $M_w$  7.0. Following the initial reverse event very little slip accumulated on the Denali fault for a distance of about 50 km to the east (S2 & S3) consistent with surface slip reports (*Eberhart-Phillips et al.*, 2003). The main Denali segment (S4) of the rupture model has 3 shallow asperities, which are principally strike-slip. The bulk of the slip is shallow (less than 10 km) consistent with the depth of relocated aftershocks (e.g. *Ratchkovski et al.*, 2003). The kinematic model presented in Figure 13.1b includes a 15 km jump in the rupture front at the Denali/Totschunda junction that is an important feature of the dynamic rupture models described below. The jump is not constrained by the seismic data however it qualitatively improves the model in the sense that the amplitude of deep slip is reduced. Slip on the Totschunda fault (S5) in the kinematic model has relatively low amplitude, and is unfortunately poorly constrained by both the GPS and seismic data sets. The total scalar seismic moment was found to be  $8.45 \times 10^{20}$  Nm, and the average and peak slips were 2.14 and 9.94 m.

A relatively high rupture velocity of 3.3 km/s was required to place the recovered strike-slip asperities far enough east to correlate with surface slip observations, which is consistent with the findings of *Frankel et al.* (2002). An average rupture velocity of 3.3 km/s also maximizes the level of fit to the seismic waveform data. Direct measurement of the S-wave arrival time at the closest recording station, site PS10 only 3 km from the fault, requires a rupture velocity of at least 3.3 km/s. It is evident from those records that a typical rupture velocity of  $0.8\beta$  is much too slow. A 3.3 km/s rupture velocity represents 98% of the shear wave velocity at 8 km depth with respect to the velocity model we used. Infrasound recordings also suggest a relatively high rupture velocity (approximately 3.3 km/s) over the length of the Denali fault from just west of the trans-Alaska oil pipeline to the Denali/Totschunda junction in the east (*Olson et al.*, 2003).

Interestingly, the western region of the fault that requires a possibly super-shear rupture velocity also has very low levels of slip suggesting that this portion of the fault may be relatively weak. The teleseismic model of *Ozacar et al.* (2003) also shows that this region had little slip, and they report that a low Bouguer gravity anomaly in this region indicates that the low density rocks in this

region are weak; a claim also supported by the lack of aftershocks (e.g. *Ratchkovski et al.*, 2003). The dynamic modeling also required this section of the Denali fault to be weak in order to allow slip to transfer from the Susitna Glacier to the Denali fault.

Static stress drop was computed from the kinematic slip model using the relation,  $\Delta\sigma = 2.44 * M_0 / A^{1.5}$ , which assumes a circular fault model for each subfault. Moment ( $M_0$ ) and area (A) were obtained for each of the 5 fault segments by integrating only those subfaults with non-zero slip. The stress drop varies considerably over the fault with values of 2.9, 1.0, 3.2, 5.2 and 2.4 MPa for segments 1-5, respectively.

### 0.3 Dynamic Source Modeling

To dynamically model the Denali event, we use the 3-D finite element method (*Oglesby*, 1999; *Whirley and Englemann*, 1993) and a slip-weakening friction law. The material and computational parameters used in our models are;  $V_p$  6.25 km/s,  $V_s$  3.55 km/s, density 2790 kg/m<sup>3</sup>, shear stress 8.46 Mpa, normal stress 27.63 Mpa, static friction 0.6, dynamic friction 0.12, and critical slip-weakening distance 0.624 m. The fault geometry and finite element mesh are shown in Figure 13.1c, and the discretization on the fault is 2 km by 2 km. The fault geometry is a slight simplification of that used in the kinematic models, with the Susitna Glacier fault having the same strike as the Denali fault, and meeting the Denali fault at its deepest extent. Unfortunately, the large size of the fault system requires a coarse discretization of 2-km along the fault, which in turn means that we cannot resolve the slip weakening distance of 0.624 m in our models. However, as will be argued below, this lack of resolution does not significantly affect the major features of our models. For simplicity, we use a homogeneous, infinite-Q half-space in the dynamic models, corresponding to an intermediate depth in the velocity mode used in the kinematic modeling.

The key ingredient in our dynamic models is the fault stress. *Ratchkovski and Hansen* (2002) show that the maximum principal stress is oriented approximately 85 degrees from the strike of the main Denali fault segment. However, we find it difficult to produce rupture with correct timing on all fault segments using such a simple stress field. A stress field that rotates with the fault strike is one means of solving this problem, but for simplicity we choose a principal compressive stress oriented 65 from the strike of the main Denali segment. The stress field in the western part of the fault, at the intersection between the Susitna Glacier and Denali faults, is likely to be very complicated, due to the complex fault geometry in this region. For computational reasons a simpler fault geometry in this area is used. For both these reasons, we do not attempt to use a single regional stress field to produce fault stresses in this region. Rather, for

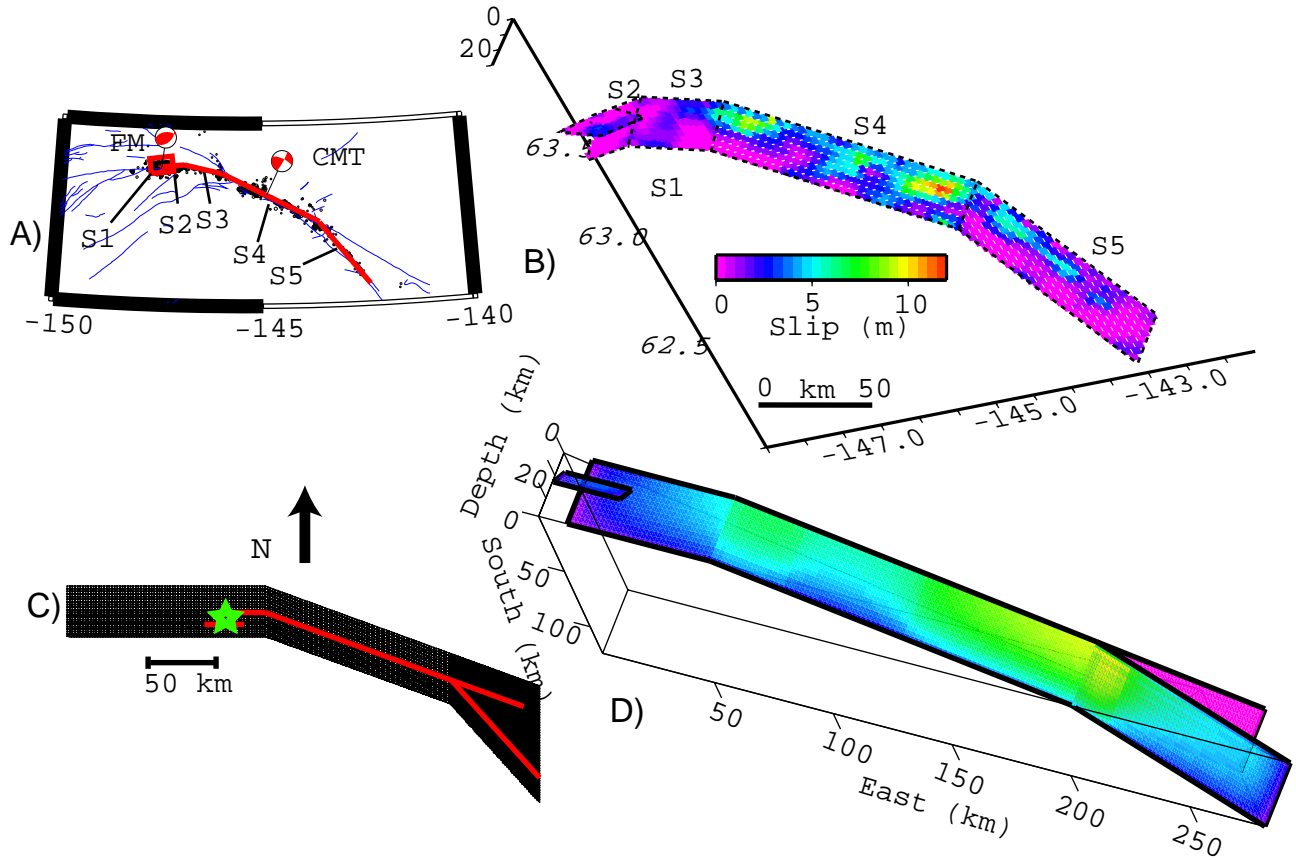


Figure 13.1: . A) 5-segment fault model, the first motion (FM) and Harvard CMT solutions for the mainshock, and regional faults (blue lines). B) 3D projection of the kinematic slip model. C) Map view of fault geometry (red) and finite element mesh used in dynamic models. The mesh is embedded in a much larger buffer mesh to eliminate spurious reflections from the model boundaries. The imposed epicenter is shown by the green star. D) Final slip distribution for the preferred dynamic model. Color version of this figure is found in Chapter IV

simplicity, we impose shear and normal stresses that give a stress drop of approximately 30 bars on the Susitna Glacier fault and 15 bars on the western 50 km of the Denali Fault. This difference in stress drop is consistent with the kinematic observations. To better match the slip distribution of the earthquake we reduce the initial shear and normal stress by 50% between 82 and 130 km along the main Denali Segment, reduce the shear stress by 50% on the Totschunda fault starting 20 km from the branching point and continuing to the end of the segment, and reduce the shear stress to zero in the top 2 km of the Totschunda and eastern Denali faults.

The slip for our preferred dynamic model is shown in Figure 13.1d. The seismic moment in this model is  $7.28 \times 10^{20}$  Nm, corresponding to  $M_w$  7.9. While we do not match the fine details of the kinematic model, we match many of the main features, including patches of high slip at both ends of the main Denali branch. The modeled surface slip matches the mapped surface slip

quite well in both pattern and amplitude. Most importantly, rupture propagates to the Totschunda fault, and abandons the Denali fault at the branch in the east, although the rupture propagates (with relatively low slip) for about 40 km. In our model, this propagation pattern is a direct result of the more favorable orientation of the Totschunda fault with respect to the discussed regional stress field, coupled with the dynamic effect that slip on the Totschunda fault sends the eastern Denali segment into a stress shadow (e.g. *Kame et al.* (2003); *Bhat et al.* (2002)) Another interesting feature of the dynamic model is that rupture propagation is discontinuous: Due to the more favorable orientation of the Totschunda fault near the western branch, stress waves from the Denali fault trigger slip on the Totschunda segment approximately 14 km ahead of the primary rupture front. Experiments with finer fault discretization in the branching region show similar jumping patterns, indicating that the discontinuous rupture is not an artifact of

our low spatial resolution. Minor changes to the stress field produce slightly different jumping lengths, but the main effect remains. Interestingly, stress fields that do not produce jumping rupture also tend to allow significant slip on the eastern Denali segment, in conflict with observations.

## 0.4 Conclusions

Regional seismic waveforms, continuous and campaign-mode GPS data, and surface slip measurements were used to obtain a kinematic model of the rupture process of the November 3, 2002  $M_w$  7.9 Denali, Alaska, earthquake. The event initiated as a  $M_w$  7.0 reverse slip event on the north-dipping Susitna Glacier fault with subsequent right-lateral slip distributed over approximately 300 km of the Denali fault system. Near-shear rupture velocity was inferred from direct measurement of S-wave arrival time and the kinematic modeling. The average and maximum slips were found to be 2.14 m and 9.94 m. Static stress drop varies from 1 to 5.2 MPa over the 5-segment fault model. The dynamic models point toward the possibility of discontinuous rupture propagation in this event. Such discontinuous rupture propagation has been implied in kinematic models of earlier events (e.g., the 1984 Morgan Hill event (*Beroza and Spudich, 1988*)), but in this case the dynamic source of the effect is identified in terms of the fault geometry rather than heterogeneity in strength on a planar fault. In addition to qualitatively improving the kinematic slip model for this event, discontinuous rupture propagation may help to explain some of the apparent rapid rupture propagation, and aid in the abandonment of the Denali segment, in agreement with observations.

## 0.5 Acknowledgements

We thank Jeff Freymueller and Sigrun Hreinsdóttir for providing their GPS solutions for both the continuous and campaign-mode sites, and Mark Murray for his help with GPS solutions at the initial stages of this study.

## 0.6 References

Beroza, G.C., and P. Spudich, Linearized inversion for fault rupture behavior: application to the 1984 Morgan Hill, California, earthquake, *Bull. Seism. Soc. Am.*, *93*, 6275-6296, 1988.

Bhat, H.S., R. Dmowska, J.R. Rice, and N. Kame, Testing theory for fault branching: Denali to Totschunda, Alaska, November 3, 2002, *EOS Trans. AGU*, *83*, Fall Meet. Suppl., Abstract S72F-1364, 2002.

Dreger, D. S., D. Oglesby, R. Harris, N. Ratchkovski, and R. Hansen, Kinematic and dynamic rupture models of the November 3, 2002  $M_w$  7.9 Denali, Alaska, earthquake, *Geophys. Res. Lett.*, *submitted*, 2003.

Eberhart-Phillips, D., et al., The 2002 Denali fault earthquake, Alaska: A large magnitude, slip-partitioned event, *Science*, *300*, pp. 1113-1118, 2003 DOI 10.1126/science.1082703.

Frankel, A. D., N. N. Biswas, A. H. Martirosyan, U. Dutta, and D. E. McNamara, Rupture Process of the M7.9 Denali Fault, Alaska, Earthquake Determined from Strong-Motion Recordings, *EOS Trans. AGU*, *83*, Fall 2002 AGU meeting S72F-1340, 2002.

Hartzell, S. H., and T. H. Heaton, Inversion of strong ground motion and teleseismic waveform data for the fault rupture history of the 1979 Imperial Valley, California, earthquake, *Bull. Seism. Soc. Am.*, *73*, 1553-1583, 1983.

Hreinsdóttir, S., J. T. Freymueller, H. J. Fletcher, C. F. Larsen, and R. Brügmann, Coseismic slip distribution of the 2002 MW7.9 Denali fault earthquake, Alaska, determined from GPS measurements, *Geophys. Res. Lett.*, *30*, 1670, doi:10.1029/2003GL017447, 2003.

Kame, N., J.R. Rice, and R. Dmowska, Effects of pre-stress state and rupture velocity on dynamic fault branching, *J. Geophys. Res.*, *108*, 2265, doi:10.1029/2002JB002189, 2003.

Kaverina, A., D. Dreger, and E. Price, The combined inversion of seismic and geodetic data for the source process of the 16 October, 1999,  $M_w$  7.1 Hector Mine, California, earthquake, *Bull. Seism. Soc. Am.*, *92*, 1266-1280, 2002.

Okada, Y., Surface deformation due to shear and tensile faulting in a halfspace, *Bull. Seism. Soc. Am.*, *75*, 1135-1154, 1985.

Oglesby, D.D., Earthquake dynamics on dip-slip faults, Ph. D. thesis, *University of California, Santa Barbara*, 1999.

Olson, J.V., C.R. Wilson, and R.A. Hansen, Infrasound associated with the 3 November, 2002 Denali Fault, Alaska earthquake, *Geophys. Res. Lett.*, *submitted*, 2003.

Ozakar, A.A., S.L. Beck, and D.H. Christensen, Source process of the 3 November 2002 Denali fault earthquake (central Alaska) from teleseismic observations, *Geophys. Res. Lett.*, *30*, 1638, doi:10.1029/2003GL017272, 2003.

Ratchkovski, N. A., and R. A. Hansen, New constraints on tectonics of interior Alaska: earthquake locations, source mechanisms, and stress regime, *Bull. Seism. Soc. Am.*, *92*, 998-1014, 2002.

Ratchkovski, N.A., A. Hansen, J.C. Stachnik, T. Cox, O. Fox, L. Rao, E. Clark, M. Lafeyers, S. Estes, J.B. MacCormack, T. Williams, and K.R. Kore, Aftershock sequence of the MW 7.9 Denali, Alaska, earthquake of 3 November, 2002 from the regional seismic network data, *Seism. Res. Lett.*, *in press*, 2003.

Whirley, R.G., and B.E. Engelmann, DYNA3D: A Nonlinear, Explicit, Three-Dimensional Finite Element Code for Solid and Structural Mechanics - User Manual,

*University of California, Lawrence Livermore National  
Laboratory, 1993.*

## Chapter 14

# Accuracy of the Hypocenter Location and Fault Plane Orientation for Near Realtime Finite Fault Inversion

Wu-Cheng Chi, Asya Kaverina, and Doug Dreger

### 0.1 Introduction

Recently there has been a push within the seismological community to produce maps of ground shaking intensity in near real time for emergency response purposes. In densely instrumented regions, such as Southern California, Japan, and Taiwan, these maps can be generated using ground-truth measurements. However, other approaches are needed for regions with sparse station coverage. One of them is to derive finite source parameters in near real time, then forward model the ground shaking in the regions of interest (e.g. *Dreger and Kaverina, (2000)*). To successfully predict ground motion we need to have good waveform fits at all azimuths from the hypocenter. An initial set of good source parameters will dramatically reduce the time required to derive a good slip model and enable us to generate synthetic ground shaking information. It is also beneficial to have correct finite source information soon after the earthquake. The information then can help to identify the causative fault plane, design temporary portable seismic networks to monitor the aftershocks surrounding the main event, and forward calculate the stress perturbation due to the earthquake.

We inverted strong motion data for the finite source parameters of 6 large aftershocks of the 1999 Chi-Chi, Taiwan earthquake. The locations and origin times are depicted in Figure 1. For each event, we derived a preferred model by testing different focal mechanisms, hypocenters, and other source parameters in more than 1000 inversions. We documented how the fits between the observed waveforms and the corresponding synthetics deteriorated as the hypocenter and focal mechanism deviate from those of the preferred model. These results will

help to determine how accurate these parameters must be if we wish to derive slip models in near real-time for generating ShakeMaps.

### 0.2 Data Analyses and Results

More than 6 Chi-Chi, Taiwan Earthquake aftershocks with  $M_w$  5.8-6.4 were well-recorded by a strong motion network maintained by the Central Weather Bureau of Taiwan. They provided an unprecedented opportunity to study the finite source process of moderate sized earthquakes. Each aftershock was recorded by more than 200 strong motion stations. We use only data from stations that had no apparent timing errors and provide good azimuthal coverage. We have converted each waveform from digital counts to  $\text{cm/s}^2$ , removed the mean offset, integrated from acceleration to velocity, and band-pass filtered between 0.02 and 0.5 Hz with a four-pole acausal Butterworth filter before resampling the data to 10 sps. Using a frequency-wave number code from Chandan Saikia (*Saikia, 1994*), we calculated a catalog of Green's functions for an average 1D velocity model taken from a 3D tomographic study by *Rau and Wu (1995)*. This 1D model had been tested in routine regional moment tensor studies of local and regional events and performed well for the finite fault inversions of Chi-Chi mainshock and aftershock. The Green's functions were then subjected to the same signal processing as the observed waveforms. We used strong motion data to invert the representation theorem for parameters of the finite source using a method pioneered by *Hartzell and Heaton (1983)*. For each event we tested a range of values for each of the source parameters: the slip vector, fault orientation, location, hypocentral depth, rupture velocity, and dislocation rise time. In this modeling we assumed that the rupture velocity and dislocation rise time were constant and did not vary spatially. For each event, we performed more than 1000 sensitivity tests by

varying the source parameters used in the inversions and we documented the influence these parameters have on the slip model and the waveform fits. The preferred models derived after these extensive tests usually gave more than 20% improvement in waveform fits.

We found that, if the deviation in hypocenters and focal mechanisms were less than 5 km and  $20^\circ$ , respectively, we generally recovered more than 80% of the preferred model's synthetic waveform fit, measured by variance reduction. The length of 5 km (Figure 14.1) is similar, and maybe related, to the widths of the slip patches we modeled. For the thrust events, the input dip angle of the fault must be correct to within  $20^\circ$ . For the strike-slip event, the input fault strike must also be within  $20^\circ$  of the true strike (Figure 14.2).

### 0.3 Conclusion

For each of the six Chi-Chi, Taiwan aftershock events, we performed more than 1000 sensitivity tests by varying the source parameters used in the inversions and we documented the influence these parameters have on the slip model and the waveform fits. Good waveform fits can mostly be achieved if the errors in hypocenters and focal mechanisms are within 5 km and  $20^\circ$ , respectively. However, in some cases good waveform fits can also be achieved outside of the preferred ranges of the input source parameters. These results provide the criteria needed to evaluate the performance of the seismic network if we want to invert the finite fault parameters of magnitude 6 earthquakes in real time and use the source model to forward-model the ShakeMaps, which can be used by the seismic response authorities for seismic mitigation purposes.

### 0.4 Acknowledgements

We thank Dr. Willie Lee for providing the strong motion data from Central Weather Bureau (CWB) of Taiwan and Dr. Win-Gee Huang for the strong motion data from IES, Academia Sinica of Taiwan. We thank CWB for providing their aftershock seismicity data. This research is funded by NSF Grant EAR-0000893 and PEER Lifelines 1E06.

### 0.5 References

Dreger, D., and A. Kaverina, Seismic remote sensing for the earthquake source process and near-source strong shaking: A case Study of the October 16, 1999 Hector Mine Earthquake, *Geophys. Res. Lett.*, it 27, 13,1941-1944, 2000.

Hartzell, S.H., and T.H. Heaton, Inversion of strong ground motion and teleseismic waveform data for the fault rupture history of the 1979 Imperial Valley, California, Earthquake, *Bull. Seism. Soc. Am.*, 73, 1553-1583, 1983.

Rau, R.-J., and F. Wu, Tomographic imaging of lithospheric structures under Taiwan, *Earth Planet. Sci. Lett.*, 133, 517-532, 1995.

Saikia, C.K., Modified frequency-wave-number algorithm for regional seismograms using Filon's quadrature-modeling of L(g) waves in eastern North America, *Geophys. J. Int.*, 118, 142-158, 1994.

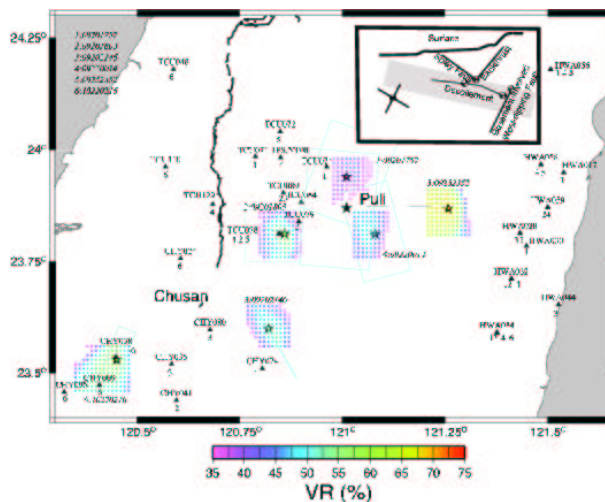


Figure 14.1: Preferred locations of the aftershock events studied are marked as stars. The origin times for these events are shown at the upper left corner. The dot color shows the variance reduction derived from inversions using that particular location as epicenter. It shows how rapidly the waveform fits, measured by variance reduction (VR), deteriorate if the epicentral information is incorrect. In general, the VR will drop 20% if the epicenter is off by 5 km. Results for Event 5 are shifted to the east for clear presentation. The blue rectangles are the fault dimensions of the preferred slip models. The cross section in the upper right corner shows a schematic with possible rupture scenarios for the aftershocks we studied.

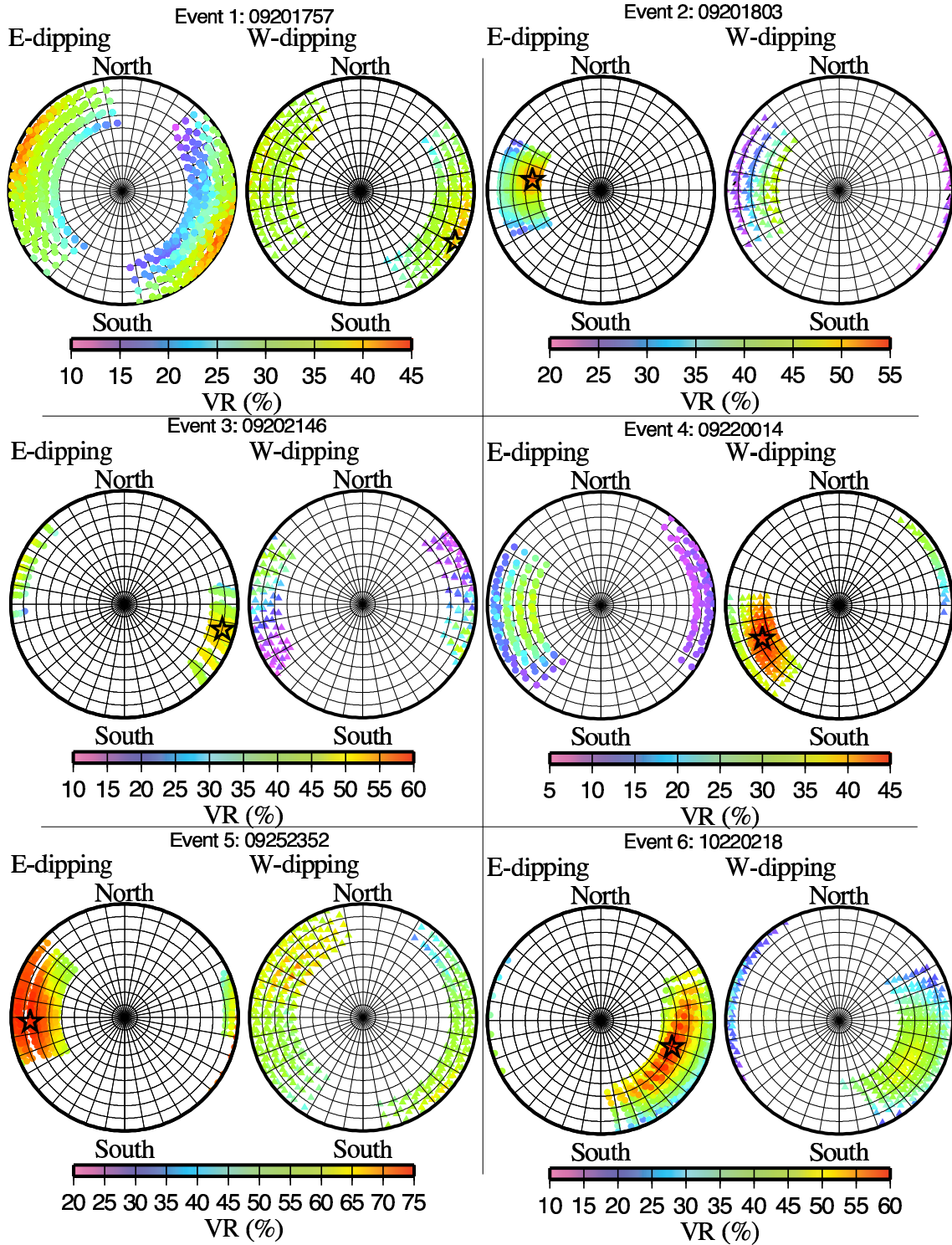


Figure 14.2: The results of sensitivity tests on the focal mechanism for each event. The P axis of each focal mechanism tested is plotted in lower hemisphere stereonet projection. The left stereonet shows the east-dipping fault planes, the right ones the west-dipping planes. The color shows the variance reduction. Note VR deteriorates fastest when the plunge of the P axis changes, implying the waveform fits are most sensitive to the dip, and possibly rake, of the focal mechanism for the thrust events. For the strike-slip aftershock (Event 3), VR is more sensitive to strike. We interpreted this to be the result of the amplitude of the S wave radiation pattern, which controls the inversion results. The star shows the P axis of the preferred focal mechanism. Overall, the waveform fits are pretty good if the fault orientation is accurate within 20 degrees.

## Chapter 15

# Historical Earthquake Re-analysis Project

Robert A. Uhrhammer

### 0.1 Introduction

The objective of this USGS NEHRP funded two-year project, that commenced in March, 2000, is to characterize the spatial and temporal evolution of the San Francisco Bay Region (SFBR) seismicity during the initial part of the earthquake cycle as the region emerges from the stress shadow of the great 1906 San Francisco earthquake.

The fundamental problem is that the existing BSL seismicity catalog for the SFBR, which spans most of the past century (1910-present), is inherently inhomogeneous because the location and magnitude determination methodologies have changed, as seismic instrumentation and computational capabilities have improved over time. As a result, the SFBR seismicity since 1906 is poorly understood. Creation of a SFBR catalog of seismicity that is homogeneous, that spans as many years as possible, and that includes formal estimates of the parameters and their uncertainty is a fundamental prerequisite for probabilistic studies of the SFBR seismicity.

The lack of a homogeneous catalog of earthquake for the SFBR which spans most of the past century, the availability of the invaluable BSL seismological archive, the interest in the Working Group on California Earthquake Probabilities (WGCEP, 1999), the funding of an initial effort with support from the USGS-PG&E CRADA, and the purchase and loan of a high-resolution wide-format digitizer by the USGS, combine to provide both an incentive and an unique opportunity to systematically re-process, using modern algorithms, the BSL seismographic records and data for SFBR earthquakes and to produce a homogeneous catalog of earthquakes for the region.

Our approach is to systematically re-analyze the data acquired from the archive to develop a homogeneous

SFBR catalog of earthquake location, local magnitude ( $M_L$ ), moment magnitude ( $M_w$ ), and seismic moment tensor (mechanism), including formal uncertainties on all parameters which extends as far back in time as the instrumental records allow and which is complete above appropriate threshold magnitudes. We anticipate being able to compile a new SFBR catalog of location and  $M_L$  which spans 1927 to the present and is complete at the  $M_L \sim 3$  threshold, and of  $M_w$  which spans 1911 to the present and which is complete at the  $M_w \sim 4.5$  threshold.

### 0.2 Previous Effort

During the summer of 1998, the USGS funded two students, via a USGS-PG&E CRADA, to transcribe the data from the original BSL reading/analysis sheets to computer readable form. With this funding, they were able to transcribe the reading/analysis sheets for SFBR earthquakes, working back in time from 1983 through 1944 (1984 onward was already in a computer database).

The Wood-Anderson maximum trace amplitude data used in the determination of  $M_L$  were not registered on the original reading/analysis sheets kept in the BSL archive, so we read the maximum trace amplitudes recorded by the Wood-Anderson seismograms in order to calculate  $M_L$  and its uncertainty. The manpower intensive task of reading the maximum trace amplitudes registered by the Wood-Anderson seismograms for Berkeley (BRK), Mt. Hamilton (Lick Observatory; MHC), Palo Alto (Banner Station; PAC), and San Francisco (USF) that are kept on store in the BSL seismogram archive in Edwards Stadium, which began with the 1950 Wood-Anderson records and worked backward in time and finished with the earliest Wood-Anderson records (circa 1927), was completed in June 2001. At the same time we also completed the process of transcribing the data from the original reading/analysis sheets to computer readable flat files bank through 1927.

We finished transcribing the 1910-1927 data (pre-Wood-Anderson instrument) data from the original read-

ing/analysis sheets to computer readable flat files in December 2001. Prior to the advent of the Wood-Anderson seismographs, there were only two seismic stations operating in the Berkeley network, namely at the Student Observatory on the Berkeley Campus (BRK) and at the Lick Observatory at Mt. Hamilton (MHC). During the pre-1927 era, the primary seismic instrumentation at BKS and MHC consisted of Bosch-Omori and Wiechert seismographs which operated at low magnification (100x) and recorded on smoked paper.

We began the time consuming task of scanning and digitizing selected pre-1932 seismograms in September 2001. Obtaining digital representations of the Bosch-Omori and Wiechert smoked paper seismograms is crucial particularly because the earliest smoked paper records, kept on store in the Berkeley Seismogram Archive, are becoming quite brittle and difficult to handle. We have been scanning these seismograms mostly on a flat bed scanner because some of the records could be damaged if they are passed through the rollers in the large format scanner. In February, 2002, the project received a six-month no-cost extension to complete this labor intensive scanning and digitizing effort.

See previous Annual Reports for more detailed information.

### 0.3 Progress During the Past Year

The task of scanning and digitizing the pre-1933 seismograms was completed in August 2002. Figure 15.1 compares the E-component signals recorded by co-sited Bosch-Omori, Galitzin, and Wood-Anderson seismometers located at BRK on the Berkeley campus. The quality of these images is fairly typical of the types of images that can be obtained by scanning the old paper seismograms kept on store in the BSL seismogram archive. A comparison of the Bosch-Omori, Galitzin, and Wood-Anderson records for ten SFBR earthquakes which occurred in 1931 and 1932, when all three types of instruments were on operation at Berkeley, was used to empirically calibrate the magnitude estimates for SFBR events which occurred prior to the installation of the Wood-Anderson seismographs.

We found that the existing earthquake location algorithms do not provide robust solutions when using the potentially imprecise data available from the sparse four-station pre-1960 SFBR seismic network. Consequently, a fuzzy logic based algorithm was developed to facilitate the determination of robust earthquake locations (Uhrhammer, 2001). The algorithm inherently has a high tolerance for imprecision in the observed data and it can yield robust sparse network solutions without requiring that the problematic observed data be either identified, down-weighted, or removed. This characteristic also renders the algorithm ideally suited for use in automated systems, such as the REDI Project, which provide rapid

earthquake information.

The ultimate goal of this project has been the development of a uniform and internally consistent catalog of SFBR seismicity for instrumentally recorded earthquakes which have occurred during the past century in the region and to make the data and the results of this study available on-line via the Northern California Earthquake Data Center at <http://quake.geo.berkeley.edu>.

As a part of this goal, we also developed a calibration procedure for obtaining robust earthquake locations throughout a time when the number of SFBR seismic stations evolved from the initial two stations (BRK and MHC) at the turn of the last century to the more than 100 seismic stations at present (Uhrhammer, 2003). The complex geology and faulting observed in the SFBR results in seismic wave propagation times which scatter significantly over differing propagation paths in the region.

The final effort to place all the raw and processed data on the NCEDC is underway. The goal is to have all the raw data and the results in a searchable format and to be available on-line circa September 2003.

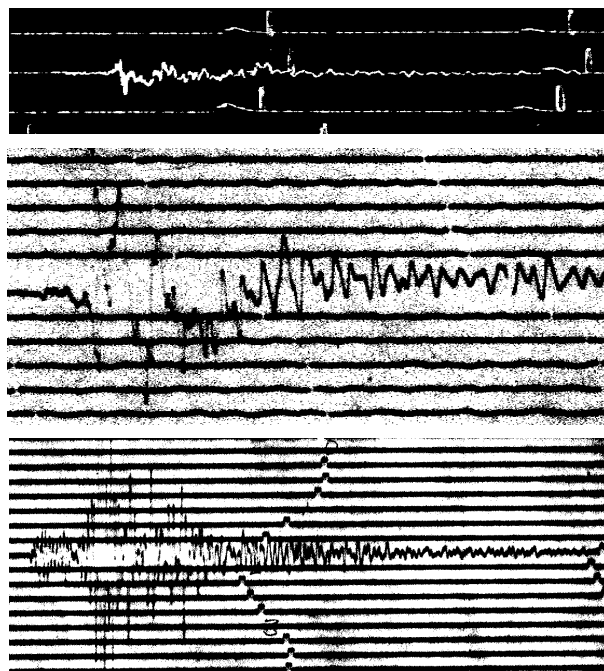


Figure 15.1: Example of scanned seismograms. Shown are the BRK E-component Bosch-Omori (top), Galitzin (middle), and Wood-Anderson (bottom) seismograms for a  $M_L$  4.5 earthquake which occurred on June 14, 1932 at 09:44:13 UT. The epicenter is located along the San Andreas Fault approximately 2 km N of Castle Rock State Park and 71 km SSE of Berkeley. For reference, the distance between adjacent traces is 10 mm, 2.5 mm and 2.5 mm on the original Bosch-Omori, Galitzin, and Wood-Anderson seismograms, respectively.

## 0.4 Acknowledgements

We thank William Bakun of the USGS who encouraged us to pursue this project. UC Berkeley students Tom Fournier and Gabe Trevis participated in this project during the past year and we thank them for their efforts.

This project was supported by the USGS, through the NEHRP External Grants Program.

## 0.5 References

Bolt, B. A. and R. D. Miller, Catalog of Earthquakes in Northern California and Adjoining Areas: 1 January 1910 - 31 December 1972, *Seismographic Stations, University of California, Berkeley*, iv + 567 pp., 1975.

Uhrhammer, R. A., The San Francisco Bay Region Historical Earthquake Re-analysis Project: A progress report and locating pre-1960 instrumentally recorded earthquakes using a fuzzy-logic-based algorithm, *Seism, Res, Lett.*, 72, 245, 2001.

Uhrhammer, R. A., Historical Earthquake Re-analysis Project: San Francisco Bay Region, *Seis. Research Lett.*, 74, p. 217, 2003.

# Chapter 16

## Northern California Seismicity Project

Robert A. Uhrhammer

### 0.1 Introduction

The Northern California Seismicity Project (NCSP) is a counterpart to the San Francisco Bay Region (SFBR) - Historical Earthquake Re-analysis Project (HERP) reported in the research section on HERP. The initial objective of this project which commenced in August, 2000, is to transcribe the pre-1984 data for  $M_L \geq 2.8$  earthquakes which have occurred in Northern and Central California (NCC) (outside of the SFBR covered by HERP), from the original reading/analysis sheets, kept on store in the Berkeley Seismological Archives, to a computer readable format.

As is the case with HERP, characterization of the spatial and temporal evolution of NCSP seismicity during the initial part of the earthquake cycle as the region emerges from the stress shadow of the great 1906 San Francisco earthquake is the long term goal. The problem is that the existing BSL seismicity catalog for the SFBR, which spans most of the past century (1910-present), is inherently inhomogeneous because the location and magnitude determination methodologies have changed, as seismic instrumentation and computational capabilities have improved over time. As a result, NCC seismicity since 1906 is poorly understood.

Creation of a NCC seismicity catalog that is homogeneous, that spans as many years as possible, and that includes formal estimates of the parameters and their uncertainty is a fundamental prerequisite for probabilistic studies of the NCC seismicity. The existence of the invaluable BSL seismological archive, containing the original seismograms as well as the original reading/analysis sheets, coupled with the recently acquired BSL capability to scan and digitize historical seismograms at high resolution allows the application of modern analytical algorithms towards the problem of determining the source parameters of the historical SFBR earthquakes.

### 0.2 Background and Motivation

Although the 1910 to present BSL catalog of earthquakes for NCC appears to be a simple list of events, one must remember that it really is a very complex data set. It is easy to misinterpret observed variations in seismicity if we do not understand the limitations of this catalog. The existing 1910 to present BSL catalog of earthquakes for NCC is inhomogeneous in that it suffers from the three types of man-made seismicity changes identified by *Habermann*, 1987, namely detection changes, reporting changes, and magnitude shifts. The largest change in the detection capability of the BSL seismic station network occurred starting circa 1927 with the installation of the Wood-Anderson and Benioff seismometers at several sites in NCC (see Figure 16.1) and the resulting increase in sensitivity lowered the threshold for detection of NCC earthquakes by about 2  $M_L$  units. The most significant reporting change occurred circa 1942 when the BSL began determining  $M_L$  for some earthquakes and by 1948  $M_L$  was routinely determined and reported for all SFBR earthquakes listed in the BSL Bulletin (*Romney and Meeker*, 1949). A magnitude shift occurred in 1954 when the response of the Wood-Anderson seismographs changed (owing to changing the free period from 1.0 to 0.8 seconds) (*Bolt and Miller*, 1975).

The lack of a homogeneous catalog of earthquake for the SFBR which spans most of the past century, the availability of the invaluable BSL seismological archive, the interest in the Working Group on California Earthquake Probabilities (WGCEP, 1999), the funding of an initial effort with support from the USGS-PG&E CRADA, and the purchase and loan of a high-resolution wide-format digitizer by the USGS, combine to provide both an incentive and a unique opportunity to systematically re-process, using modern algorithms, the BSL seismographic records and data for SFBR earthquakes and to produce a homogeneous catalog of earthquakes for the region.

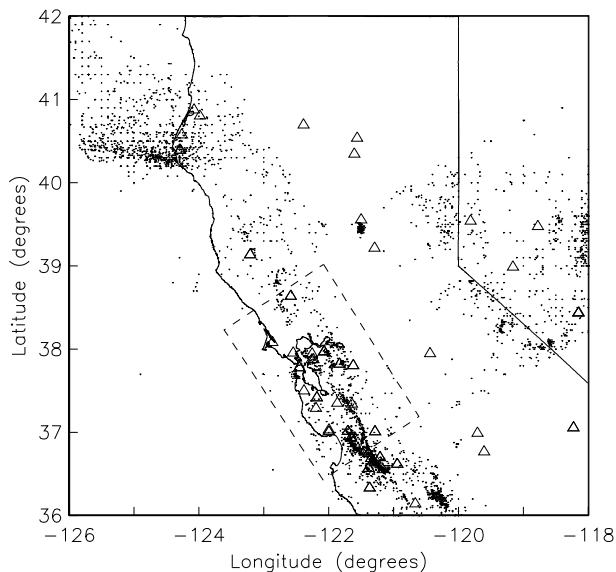


Figure 16.1: Map of the NCC Region showing the 1951-1983  $M_L \geq 2.9$  seismicity (small dots). The triangles are the seismic stations, operated by Berkeley and adjacent networks between 1951 and 1983, for which data are available. Events occurring in the dashed inset box are being transcribed and analyzed via HERP (see the previous section).

### 0.3 Current Effort

To expedite the transcription process, we converted all relevant available data from the online NCEDC event catalogs and the in-house phase data to the flat transcription file format as shown in Figure 16.2 for the years 1978 through 1983. We also acquired a copy of the International Data Center (ISC) CDROM which contains events and associated station data published in the ISC Bulletins from January 1964 through December 1977 (Version 1.2). This ISC data set includes event and station data contributed by Berkeley and the CDROM also contains an algorithm to search the database and extract and translate the ISC coded phase Berkeley data to a readable print format for years 1963 through 1977. This enabled us to start with transcription files that contained approximately half of the data that is on the original reading/analysis sheets for the years 1964 through 1983. The primary data from the original reading/analysis sheets, that was not included in this process, was the Wood-Anderson maximum trace amplitude data that is crucial for the determination of local magnitude.

During the past year two students worked on the process of transcribing the data from the original BSL reading/analysis sheets to computer readable form. They started by transcribing the original reading/analysis sheets from 1963 and they have been working back in time. The data from 1952 through 1983 has now been

```

NEIS 1977/01/09 23:24:39 39.50N 121.64W 2 14 Northern California
NEIS M-L3.3(BRK), AFTER BRK.
NEIS IO=V MM AT DOBBINS. ALSO FELT AT GRIDLEY, GOLD RUN, RACKERBY,
BRK 1977/01/09 23:24:39 39.50N 121.64W 2 3.4L Northern California
ISC *1977/01/09 23:24:37 39.55N 121.53W 2 15 Northern California

ORV 0.02 84 -iP Pn 23:24:42.00 -2.6
KPK 0.17 80 iPN Pn 23:24:44.10 -2.7
MIN 0.79 356 +iP/PKP Pn 23:24:56.00 0.4
WDC 1.29 323 +iP/PKP Pn 23:25:02.60 -0.1
WCN 1.39 99 iPN Pn 23:25:05.10 0.9
BKS 1.76 198 +iP/PKP Pn 23:25:09.00 -0.5
BKS S/(SKS) 23:25:30.00 -2.9
JAS 1.82 152 +iP/PKP Pn 23:25:10.20 -0.1
ARN 2.20 181 ePN Pn 23:25:15.60 -0.2
MHC 2.21 183 iP/PKP Pn 23:25:16.00 0.1
SAO 2.78 178 P/PKP Pn 23:25:24.00 -0.1
MNV 2.86 112 eP/PKP Pn 23:25:26.00 0.9
FRI 2.93 150 +iP/PKP Pn 23:25:26.90 0.7
BMN 3.42 74 ePN Pn 23:25:34.30 1.1
TNP 3.67 112 ePN Pn 23:25:37.40 0.7
EUR 4.30 89 iP Pn 23:25:46.00 0.4 A1.56E01 T 0.4
EUR i 23:26:53.80

```

Figure 16.2: Example of printer file of data for Berkeley network data extracted from ISC CDROM.

transcribed.

We are currently transcribing reading/analysis sheet data from 1951. Since none of the data on the pre-1964 reading/analysis sheets exists in a computer readable form, all data has to be transcribed and consequently it takes more time to transcribe each event. Also, the pre-1951 reading/analysis sheets data do not contain Wood-Anderson maximum trace amplitude data which is used in the calculation of local magnitude so that the original Wood-Anderson seismograms will have to be retrieved from the archive and the amplitudes read. This quite labor intensive component of the project is planned for the coming year.

```

E 010977 232439.5 39-30.1 121-38.6 2.0 3.4
C 5KM SOUTHWEST OF OROVILLE, CALIFORNIA
F MMI V at Oroville
F Also felt at Gridley, Gold Run, Rackerby, Marysville and
F Brownsville
P BKS Ben Z e P c 232509.0
P BKS Ben E e S - 232529.5
A BKS WA - 0.65 0.7
P MIN Ben Z i P c 232456.0
A MIN WA - 5.2 6.0
P PCC Ben Z e (P) - 232515
A PCC Ben 11 - -
P MNV Ben Z e P - 232526.-
P PRI Ben Z e - - 232538
P ORV Ben Z i P d 232442.0
P JAS Ben Z e P c 232510.2
P WDC Ben Z i P c 232502.6
P BRK Ben Z e (P) - 232510
A BRK Ben 6 - -
P SAO Ben Z e (P) - 232524.2
P FRI Ben Z e P c 232526.9
P MHC Ben Z e P (c) 232516.0
A MHC WA - 0.35 0.25
P GCC Ben Z e - - 232520
P PRS Ben Z e (P) - 232530.8
P LLA Ben Z e - - 232527
A LLA Ben 19 - -
P FHC Ben Z e - - 232518
X

```

Figure 16.3: Example of completed transcription file format for the event shown in Figure 16.2.

## 0.4 Acknowledgements

UC Berkeley students Tom Fournier, Karin Spiller, Gabe Trevis, Maxwell Wilmarth, and Jennifer Epstein participated in this project and we thank them for their efforts.

This project was partially supported by the USGS funding of the Northern California Earthquake Data Center.

## 0.5 References

Bolt, B. A. and R. D. Miller, Catalog of Earthquakes in Northern California and Adjoining Areas: 1 January 1910 - 31 December 1972, *Seismographic Stations, University of California, Berkeley*, iv + 567 pp., 1975.

Habermann, R. E., Man-made changes of seismicity rates, *Bull. Seism. Soc. Am.*, 77, 141-159, 1987.

Romney, C. F. and J. E. Meeker, Bulletin of the Seismographic Stations, *University of California Press*, 18, pp. 89, 1949.

# Chapter 17

## Parkfield Research

Robert M. Nadeau, Lane R. Johnson and Tom V. McEvilly

### 0.1 Earthquake Forecasting

In its various reports since 1988, the Working Group on California Earthquake Probabilities (WGCEP) has consistently made use of statistical models of time-dependent earthquake recurrence to help estimate earthquake probabilities in California. In all WGCEP reports, the need for a larger database of earthquake recurrence intervals is emphasized. Additional data are necessary to select from competing statistical models of earthquake recurrence and to better define the model parameters. The most recent working group reports (*WG99*, 1999; *WG02*, 2002) introduced recurrence intervals from numerous small and characteristically repeating microearthquake sequences occurring along the San Andreas fault and, in particular, at Parkfield (*Ellsworth et al.*, 1999). They included only a small fraction of the Parkfield data yet that nearly doubled the available data base from which estimates of the model parameters were made. However, even this expanded data set was considered less than adequate by the working groups. At Parkfield a significantly larger set of small repeating sequences than was used by the working groups exists (184 total sequences composed of 1073 events and 889 recurrence intervals; compared to 17 Parkfield sequences of 117 events and 100 recurrence intervals used for the WG model) and many additional sequences and events have recently been identified by our research group along the central SAF between Parkfield and the southeast terminus of the Loma Prieta rupture (*Nadeau and McEvilly*, 2003). In total, our group has now identified a total of 515 sequences yielding 2079 recurrence intervals from sequences whose characteristic magnitudes range from  $M_w$ -0.7 to  $M_w$ 3.5 (Figure 17.1).

The potential of such a large data set for helping select and refine time-dependent recurrence models is considerable, yet serious questions remain regarding the use of small earthquake data for forecasting large earthquakes (e.g. Is the variance of earthquake recurrence intervals independent of magnitude, and what normalization (if any)

could be used to account for variations in magnitude among characteristic sequences?). *Nadeau and Johnson* (1998) found that the average recurrence interval of sequences scales reasonably well for sequence magnitudes ranging from -0.7 to 6 under similar fault loading conditions. However, they did not analyze the variance of intervals as a function of magnitude. *Ellsworth et al.* (1999) analyzed magnitude dependent variance for the small data used by the working groups, and noted that the variance for both the small and large sequences was comparable. However results of their analysis, admittedly based on a small data set, had a large uncertainty. Adding to the difficulties in evaluating magnitude dependent variance are problems associated with spatial and temporal variations of fault loading rates on recurrence time variance. For example if significant slip rate transients occur over time scales comparable to the recurrence intervals of sequences (as has been observed at Parkfield) the variance of the intervals should be significantly greater than for sequences whose recurrence times are long compared to the transients.

Previous efforts at variance determinations have also relied on data dependent normalizations where the intervals for each sequence were divided by the average recurrence time of the sequences (Figure 17.1, top). However as pointed out by *Matthews et al.* (2002), this significantly under estimates the variance for typical characteristic sequences where the total number of repetitions are typically small. *Matthews et al.* also point out that discrimination between competing probability models of interval variance for earthquakes is a difficult task, even when normalization is ignored and relatively large synthetic data sets are used (e.g. 50 intervals).

### 0.2 Preliminary Findings

The unique attributes of our recurrence interval data set and auxiliary geodetic measurements of fault loading rates have the potential of overcoming many of these difficulties and of greatly expanding our understanding of the time-dependent earthquake recurrence process. Since our data set is large and since recurrence times scale with magnitude, our data can also be used to establish a

scaling relationship between average recurrence time and magnitude that is relatively insensitive to the average intervals of any individual sequence. This scaling can then be used to normalize the entire recurrence interval data set in a way that is also insensitive to the average recurrence intervals. This approach effectively circumvents the small sample bias problem discussed by *Matthews et al.* The bottom panel of Figure 17.1 shows our first attempt at normalizing our data set in this way. A significantly better fit to a lognormal-like distribution is observed compared to the distribution shown in the top panel of Figure 17.1 where individual sequence average recurrence intervals are used for normalization. Also of significance is the larger intrinsic uncertainty determined for our scale normalized data (0.63 compared to 0.46). This result is entirely consistent with the remarks of *Matthews et al.*, and supports the potential of the scaled normalization for overcoming bias problems associated with the sequence average recurrence interval normalization approach. The large number of data also significantly reduces the confidence bounds of the intrinsic uncertainty estimate.

Our 2079 recurrence intervals significantly exceed the 50 used by *Matthews et al.* in their synthetic dataset used for assessing the practicality of discriminating between competing recurrence models. This leaves some hope that discrimination between models may be feasible after all using real earthquakes and a scale-normalized dataset. Further investigation of the characteristics of the recurrence-magnitude scaling and normalization will be required before reliable conclusions can be reached in these regards, but our initial results do appear promising. The spatial and temporal characteristics of fault loading rate variations are also exceptionally well characterized in the regions where most of our repeating sequences are occurring. This information can be used to remove and/or assess any bias in the variance of recurrence interval data that variations in spatial and temporal fault loading rates introduce into their distributions. Though our dataset contains only small magnitude events, the "range" in magnitude that it spans is over 4 magnitude units. This should also allow us to test (at least for small magnitudes) the validity of the hypothesis that recurrence interval variance is independent of magnitude, an implicit assumption used by *WG99* and *WG02*.

Finally, an additional attractive feature of our dataset is that it continues to increase in size as ongoing repeating events (typically repeats for each of the 515 sequences occur on the order of every few years or less). Using these ongoing events to continually add to the recurrence interval data set can not only provide more data for constraining the forecast model parameters, but it also can be used to test forecast models on real events. This can be done by making probabilistic forecasts for the future small and frequently recurring earthquakes using competing models and then by assessing the success and failure rates of

the various forecasts.

Our future research plans include integration of the auxiliary fault loading rate and recurrence interval data as discussed above, augmentation of the recurrence interval archive with the ongoing small characteristic events, parameterizing competing forecast models using our recurrence and other available recurrence interval data, making small earthquake forecasts using the competing models and comparing the forecasts' relative success rates.

### 0.3 Acknowledgements

We appreciate support for this project by the USGS NEHRP program through grant numbers 02HQGR0067 and 03HQGR0065, by NSF through award number 9814605, and by the U.S. Department of Energy (DOE) under contract No. DE-AC03-76SF00098.

### 0.4 References

- Ellsworth, W.L., M.V. Matthews, R.M. Nadeau, S.P. Nishenko, P.A. Reasenberg, and R.W. Simpson, A physically based earthquake recurrence model for estimation of long-term earthquake probabilities, U.S. Geol. Surv. Open-File Rept. 99-522, 1999.
- Matthews, M.V., W.L. Ellsworth and P.A. Reasenberg, A Brownian Model for Recurrent Earthquakes, *Bull. Seism. Soc. Am.*, 92, 2233-2250, 2002.
- Nadeau, R.M. and L.R. Johnson, Seismological Studies at Parkfield VI: Moment Release Rates and Estimates of Source Parameters for Small Repeating Earthquakes, *Bull. Seismol. Soc. Amer.*, 88, 790-814, 1998.
- Nadeau, R.M. and T.V. McEvilly, Periodic Pulsing of the San Andreas Fault, *Science*, *submitted*, 2003.
- Working Group on California earthquake Probabilities (*WG99*), Earthquake probabilities in the San Francisco Bay Region: 2000 to 2030—a summary of findings, *U.S. Geol. Surv., Open-File Rept. 99-517*, 1999
- Working Group on California earthquake Probabilities (*WG02*), Earthquake probabilities in the San Francisco Bay Region: 2003 to 2032—a summary of findings, *U.S. Geol. Surv., Open-File Rept. (to be determined)*, 2002.

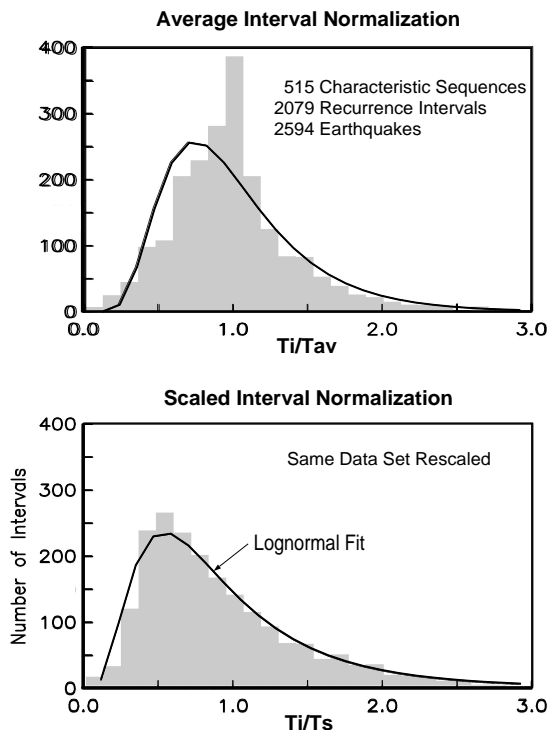


Figure 17.1: Normalized recurrence interval distributions from repeat times of 2594 characteristic small earthquakes ( $-0.8 < M_w < 3.6$ ) occurring along the central SAF from 15 km southeast to 160 km northwest of Parkfield, CA. (Top) Histogram and lognormal fit to recurrence intervals normalized by the average interval for each sequence. (Bottom) Histogram and fit for data normalized by the empirical scaling relationship of average recurrence time with magnitude for all the data. No corrections for spatial or temporal variations in fault slip rates have been applied, and all sequences, regardless of the number of member events, have been included. The exceptionally large number of characteristically repeating small earthquakes makes normalization by the scaling relationship insensitive to the biases that plague  $T_{av}$  normalized data. The surprisingly well behaved  $T_s$  scaled results and the large number of intervals available suggest it might be possible to discriminate between competing time-dependent earthquake recurrence models and to test the assumption used by the *WG99* and *WG02* recurrence model subgroup that aperiodicity of earthquake recurrence is scale independent.

## Chapter 18

# The Evolution of the Seismic-Aseismic Transition during the Earthquake Cycle: Constraints from the Time-Dependent Depth Distribution of Aftershocks

Frédérique Rolandone, Roland Bürgmann and Robert Nabelek

### 0.1 Introduction

We have demonstrated that aftershock distributions after several large earthquakes show an immediate deepening from pre-earthquake levels, followed by a time-dependent postseismic shallowing (Rolandone *et al.*, 2002). We use these seismic data to constrain the depth variations with time of the seismic-aseismic transition throughout the earthquake cycle. Most studies of the seismic-aseismic transition have focussed on the effect of temperature and/or rock composition and have shown that the maximum depth of seismic activity is well correlated with the spatial variations of these two parameters. However, little has been done to examine how the maximum depth of seismogenic faulting varies locally, at the scale of a fault segment, with time during the earthquake cycle.

The mechanical behavior of rocks in the crust is governed by frictional behavior and at greater depth by plastic flow. The coupling between the brittle and ductile layers and the depth extent and behavior of the transition zone between these two regimes is a fundamental question. Mechanical models of long-term deformation (Rolandone and Jaupart, 2002) suggest that the brittle-ductile transition is a wide zone where deformation is caused both by slip and ductile flow. Geologic observations (Sibson, 1986; Scholz, 1990; Trepmann and Stockhert, 2002) indicate that the depth of the seismic-aseismic transition varies with strain rate and therefore is also ex-

pected to change with time throughout the earthquake cycle. The maximum depth of seismogenic faulting is interpreted either as the transition from brittle faulting to plastic flow in the continental crust, or as the transition in the frictional sliding process from unstable to stable sliding. The seismic-aseismic transition therefore reflects a fault zone rheology transition or a more distributed transition from brittle to ductile deformation mechanisms.

### 0.2 Results

We investigate the time-dependent depth distribution of aftershocks in the Mojave Desert. We apply the double difference method of Waldhauser and Ellsworth (2000) to the region of the  $M$  7.3 1992 Landers earthquake to relocate earthquakes. Time-dependent depth patterns of seismicity have been identified in only few previous studies (Doser and Kanamori, 1986; Schaff *et al.*, 2002) and never quantified. This was mainly due to the problem of the accuracy of the hypocenter locations. Accurately resolving depth is the most challenging part of earthquake location. With new relocation techniques, we can investigate the time-dependent depth distribution of seismicity to reveal more intricate details in the patterns of deformation which take place during an earthquake cycle.

In this study, we focus on quantifying the temporal pattern of the deepest aftershocks. We calculate the  $d_{95}$ , the depth above which 95% of the earthquakes occur, and we also calculate the  $d_{5\%}$ , the average of the 5% of the deepest earthquakes for a constant number of events. We compare our results with the same statistics for the Hauksson relocations (catalog from Hauksson (2000) with a vertical error cutoff of 1.5 km). We specifically in-

investigate (1) the deepening of the aftershocks relative to the background seismicity, (2) the time constant of the postseismic shallowing of the deepest earthquakes. Figure 18.1 shows the time-dependent depth distribution of seismicity for the Johnson Valley fault that ruptured in the 1992 Landers earthquake. Our analysis reveals a strong time-dependence of the depth of the deepest aftershocks. In the immediate postseismic period, the aftershocks are deeper than the background seismicity, followed by a time-dependent shallowing. Figure 18.2 shows the same data but in the form of histograms and relate them to the deepening of the brittle-ductile transition after the mainshock. The temporal variations of the depth of the brittle-ductile transition reflect the strain-rate changes at the base of the seismogenic zone.

The analysis of seismic data to resolve the time-dependent depth distribution of the seismic-aseismic transition provides additional constraints on fault zone rheology, which are independent of geodetic data. Together with geodetic measurements, these seismological observations form the basis for developing more sophisticated models for the mechanical evolution of strike-slip shear zones during the earthquake cycle.

### 0.3 Acknowledgements

This research is supported by the Southern California Earthquake Center and an IGPP/LLNL grant.

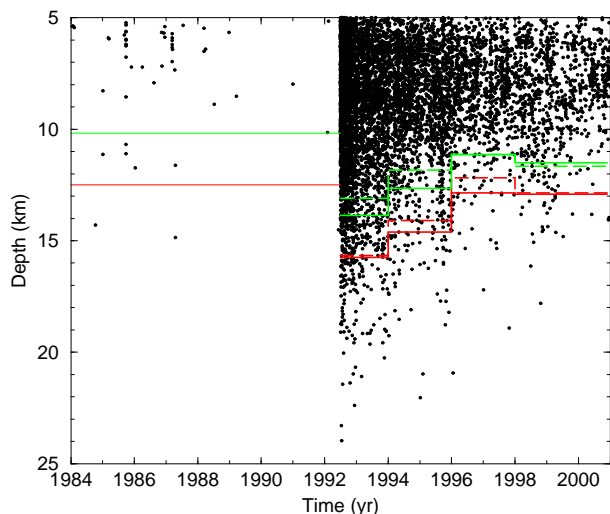


Figure 18.1: Time-dependent depth distribution of seismicity for the Johnson Valley fault. The red curve shows the statistics for the  $d_{5\%}$  and the green for the  $d_{95}$  (see text). The dashed lines show the same statistics for the Hauksson relocations and are in very good agreement with our results.

### 0.4 References

- Doser, D.I., and Kanamori H., Depth of seismicity in the Imperial Valley region (1977-1983) and its relationship to heat flow, crustal structure, and the October 15, 1979, earthquake. *J. Geophys. Res.*, *91*, 675-688, 1986.
- Hauksson, E., Crustal structure and seismicity distribution adjacent to the Pacific and North America plate boundary in southern California, *J. Geophys. Res.*, *105*, 13,875-13,903, 2000.
- Rolandone, F., and C. Jaupart, The distribution of slip rate and ductile deformation in a strike-slip shear zone, *Geophys. J. Int.*, *148*, 179-192, 2002.
- Rolandone, F., R. Bürgmann and R.M. Nadeau, Time-dependent depth distribution of aftershocks: implications for fault mechanics and crustal rheology, *Seism. Res. Lett.*, *73*, 229, 2002.
- Schaff, D.P., G.H.R. Bokelmann, G.C. Beroza, F. Waldhauser and W.L. Ellsworth, High resolution image of Calaveras Fault seismicity, *J. Geophys. Res.*, *107* (B9), 2186, doi:10.1029/2001JB000633, 2002.
- Scholz, C.H., Earthquakes and friction laws *Nature*, *391*, 37-42, 1998.
- Sibson, R.H., Earthquakes and rock deformation in crustal fault zone, *Ann. Rev. Earth Planet. Sci.*, *14*, 149-175, 1986.
- Trepmann, C.A., and B. Stockhert, Cataclastic deformation of garnet: a record of synseismic loading and postseismic creep, *J. Struct. Geol.*, *24*, 1845-1856, 2002.
- Waldhauser, F., and W. L. Ellsworth, A double-difference earthquake location algorithm: method and application to the northern Hayward fault, California, *Bull. Seismol. Soc. Am.*, *90*, 1353-1368, 2000.

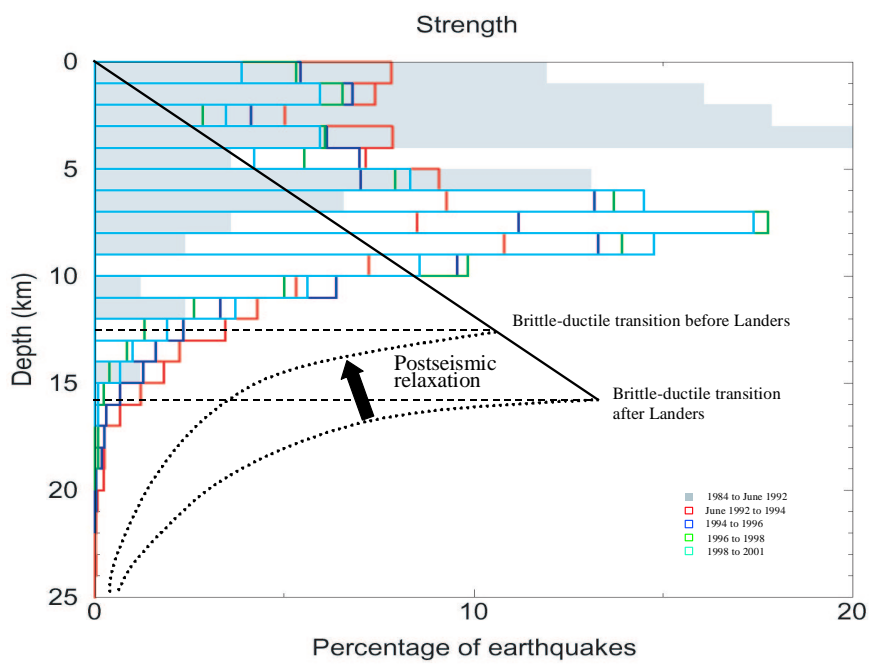


Figure 18.2: Histograms of the depth distribution of seismicity for different time periods. Overlaid is the strength of the brittle and ductile materials.

## Chapter 19

# Detection of Seismic Stress-Drop Anomalies in the Mendocino Transform Using Coda-Derived Spectra

Gilead Wurman and Douglas S. Dreger

### 0.1 Introduction

The Berkeley Digital Seismic Network (BDSN) records many regional-scale events in Northern California each year. At present, only a few of these events are assigned moment magnitudes due to the limitations of moment tensor (MT) inversion codes in use today (*Pasyanos et al.*, 1996). Complete-waveform MT inversions require good records at several stations (usually three or more) to obtain well-constrained solutions. Due to high signal to noise levels for small events such coverage is not possible, limiting the reliability of  $M_w$  estimates. In the regional context of Northern California this applies to small events with  $M_w \leq 3.5$ , and here the goal is to create a continuous  $M_w$  scale over as broad a range of magnitudes as possible. Additionally, there is interest in getting stable  $M_w$  determinations in other, sparsely instrumented regions, where reliable MT inversions cannot be done for events of even moderate magnitude.

The moment magnitude and seismic stress drop of an event can be quickly and accurately determined by fitting the decay rate of  $L_g$  or  $S_n$  phase coda via the method of *Mayeda et al.* (2003). The coda is composed of seismic waves which are multiply randomly scattered by 3-D inhomogeneities in the upper crust, and sample a broader swath than direct waves. As a result, path and distance corrections can take the form of average crustal properties and simple geometrical spreading relations, and source radiation patterns are washed out. After a station is calibrated for site response the correction holds for all future events. Because the coda method uses a continuum of arrivals rather than a small number of discrete direct arrivals a single station gives a much more robust measurement of  $M_w$  than a single station MT inversion.

In a densely instrumented region like Northern California coda-derived  $M_w$  determinations can then be made over a much broader range of earthquake sizes (from  $M_w \approx 2$  through 8). The coda method also provides stable determinations of earthquake moment-rate spectra, which can be used to examine  $E_s/M_0$  scaling in the study region.

### 0.2 Coda Decay Method

The coda method measures the narrowband envelopes of the horizontal component of ground motion and fits them to the relation (given a narrow frequency band and epicentral distance)

$$A_c(t|f,r) = A_0 \cdot H\left(t - \frac{r}{v(r)}\right) \cdot \left(t - \frac{r}{v(r)}\right)^{-\gamma(r)} \cdot e^{-b(r) \cdot \left(t - \frac{r}{v(r)}\right)}$$

where  $H$  is the Heaviside step function,  $v$  is the group velocity as a function of distance, and  $b$  and  $\gamma$  are decay functions of distance representing average crustal properties of logarithmic and power decay. These three variables are fixed by fitting theoretical functions to data from multiple calibration events at (ideally) multiple stations. Then for each event at each station the amplitude coefficient  $A_0$  can be fit, representing the power received in that narrow passband. A range of passbands is processed, providing broadband analysis. This power needs to be corrected for site response, and this is done by taking several calibration events (events with good MT solutions) and forcing level spectra at frequencies below the theoretical corner frequency for the corresponding magnitude. Making such corrections over a range of magnitudes yields overall spectra that resemble Brune-model theoretical spectra in corner frequency, DC level and  $\omega^{-2}$  falloff beyond the corner frequency (*Brune*, 1970).

When the calibration for region and individual stations is complete, any subsequent event must be processed into narrowband envelopes, and  $A_0$  must be fit at each passband.  $M_w$  can then be determined from the low fre-

quency power level (lowest two passbands), and energy release and Orowan stress drop can be calculated (Figure 19.1) by integrating the square of the moment-rate spectrum of the event (*Mayeda and Walter, 1996*).

### 0.3 Performance in the Mendocino Area

The coda method has been applied to 88 offshore events in the Mendocino transform and the Gorda plate with reasonable success. Due to possible source anomalies in transform events the list of good calibration events is fairly small (10 events). The method has been applied with more success in Northern California (*Mayeda*, unpub. data).

A significant number of events in the Mendocino transform exhibit source spectra which depart from the Brune model in characteristic ways. These events exhibit significant enrichment in low-frequency content (below 0.5 Hz) and low corner frequencies for a given  $M_w$ . These events have low Orowan stress drops and have been characterized as slow earthquakes (*Abercrombie and Ekström, 2003*), which may indicate lubrication of faults (e.g., *Okal and Stewart, 1982*).

After calibrations are performed on BDSN stations WDC and YBH, the rms magnitude discrepancy between coda and complete-waveform  $M_w$  is 0.14 above  $M_w$  3.5 for events that were not in the calibration (Figure 19.2). This scatter is probably due to uncertainties in both methods arising from the anomalous source physics noted above.

### 0.4 Real-Time Applications

The method, described briefly above, currently requires extensive user input at various stages, in particular to pick the start and end of the coda, and for quality control in the final results. The method could be modified to procedurally pick the coda based on slope, coda length and signal to noise constraints. While the calibration phase would still require human input, subsequent detections and measurement of  $M_w$  and stress drop could be done automatically, yielding results within five minutes. The coda method needs approximately 20 minutes of coda to make good measurements, and taking into account telemetry and other processing delays, a robust magnitude determination can be made within 30 minutes of an earthquake.

### 0.5 Acknowledgements

The authors gratefully acknowledge the help of Kevin Mayeda and Fumiko Tajima in creating the codes to process the raw NCEDC data into the final results. This project was funded through IGPP grant no. 03-GS-031.

### 0.6 References

- Abercrombie, R.E. and G. Ekström, Earthquake slip on oceanic transform faults, *Nature (London)*, *410*, 74-77, 2001.
- Brune, J.N., Tectonic stress and the spectra of seismic shear waves from earthquakes, *J. Geophys. Res.*, *75*, 4997-5009, 1970.
- Mayeda, K. and W.R. Walter, Moment, energy, stress drop, and source spectra of Western United States earthquakes from regional coda envelopes, *J. Geophys. Res. B*, *101*, 11,195-11,208, 1996.
- Mayeda, K., A. Hofstetter, J.L. O'Boyle and W.R. Walter, Stable and transportable regional magnitudes based on coda-derived moment-rate spectra, *Bull. Seism. Soc. Am.*, *93*, 224-239, 2003.
- Okal, E.A. and L.M. Stewart, Slow earthquakes along oceanic fracture zones: evidence for asthenospheric flow away from hotspots?, *Earth Planet. Sci. Lett.*, *57*, 75-87, 1982.
- Pasyanos, M.E., D.S. Dreger and B. Romanowicz, Towards real-time estimation of regional moment tensors, *Bull. Seism. Soc. Am.*, *86*, 1255-1269, 1996.

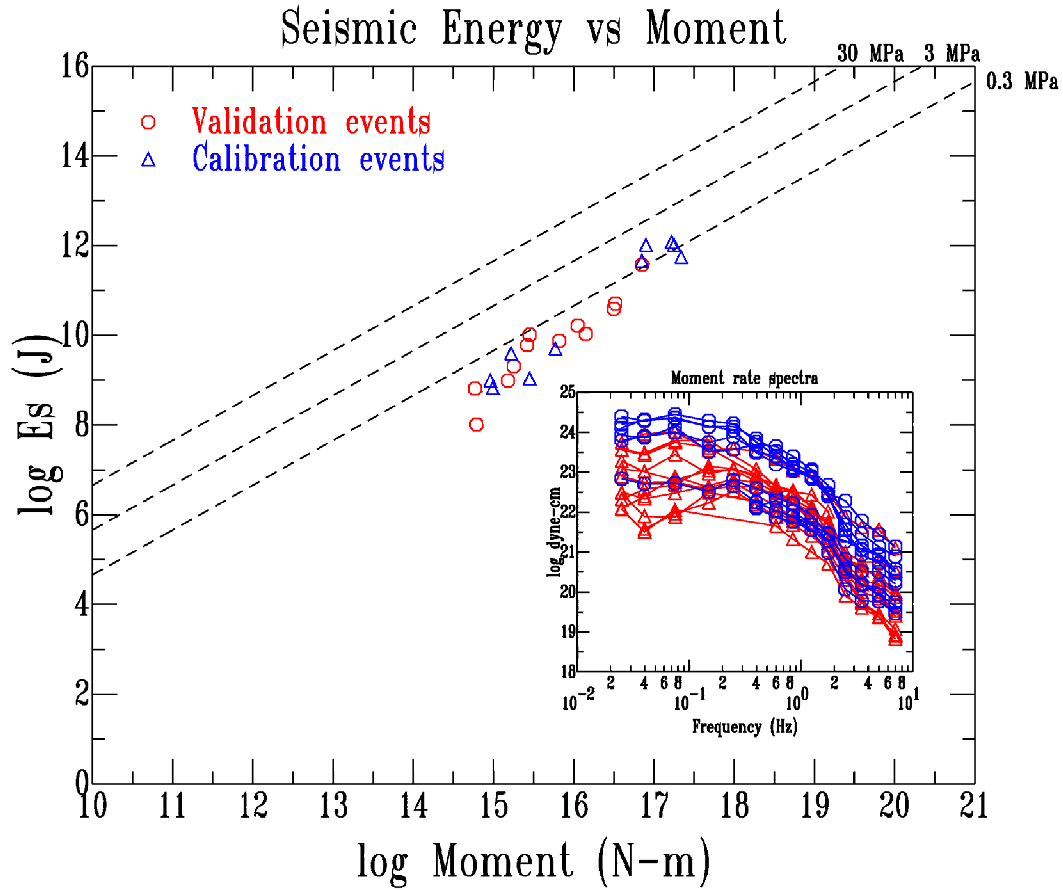


Figure 19.1: Moment-energy scaling relationship for events in the Mendocino region. Dashed lines represent constant Orowan stress drop. Inset: typical source spectra for events in the Mendocino region (averaged over stations WDC and YBH).

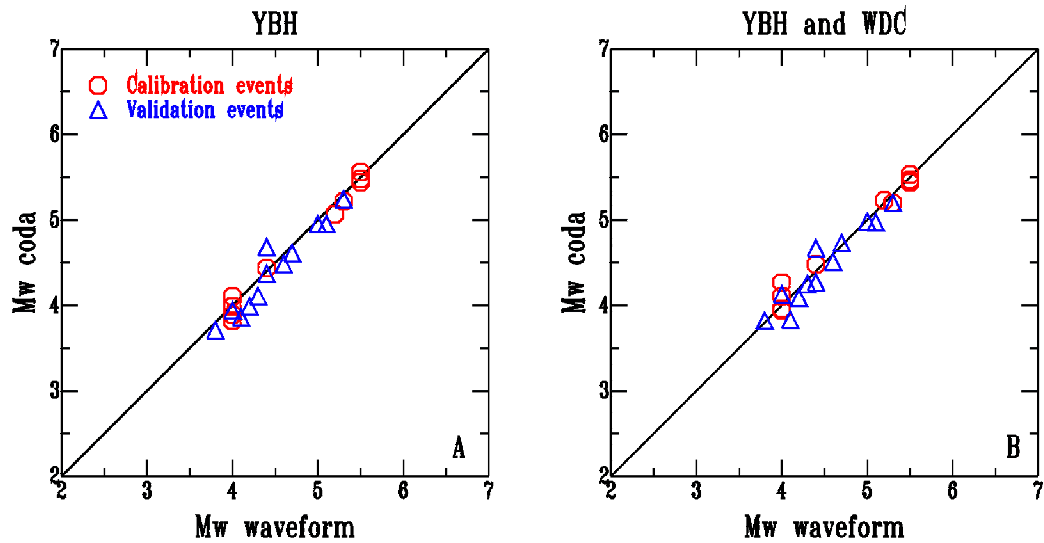


Figure 19.2: Complete-waveform  $M_w$  vs. Coda-derived  $M_w$  from station YBH (a) and averaged over stations YBH and WDC (b).

## Chapter 20

# Long-Period Microtremor Observations in the Santa Clara Valley, California

David Dolenc and Doug Dreger

### 0.1 Introduction

The 3D velocity structure of the Santa Clara Valley (SCV) was previously investigated by modeling the teleseismic P-waves (Dolenc, 2001) recorded by the 41 seismic stations of the SCV Seismic Experiment (USGS/UCB/PASSCAL, 6/98-12/98). To complement these results, we now focused on the microseisms that were recorded during the same SCV seismic experiment.

### 0.2 Results

Microseisms are generated by the pressure variations on the sea floor due to the ocean waves and can be observed in the 0.1 to 5 Hz frequency range. We first compared the noise level of several earthquake-free periods to the ocean wave heights recorded at the Santa Cruz weather buoy and showed that the two are correlated (Dolenc, 2001).

Horizontal to vertical (H/V) spectral ratios of microtremor signals for a 5-day earthquake-free period were then calculated for each station. The H/V spectral ratios for the 5-minute segments at the beginning of each hour were first calculated and then averaged over the 5 days. The results showed that the dominant period of the H/V spectral ratios in the 0.1 to 1 Hz frequency range is stable with time and is location dependent (Figure 20.1). The longer periods can be observed for the stations above the two basins and the shorter periods for the stations in-between the basins. The period of the H/V peaks as a function of the basin depth from the USGS model (Jachens, 2000) is shown in Figure 20.2.

There was no correlation between the amplitudes of the H/V spectral ratios and the USGS model basin depths.

In addition we applied the H/V method to the two local earthquakes recorded during the SCV seismic experiment (San Juan Bautista,  $M_L=5.4$ , and Gilroy,  $M_L=4.0$ ).

The results showed that for most SCV seismic stations the peaks of the H/V spectral ratios in the 0.1 to 1 Hz frequency range coincided with microseism H/V spectral ratio peaks.

The observations of the microseisms on the SCV stations show that the presence of the basins can be observed even for the time periods without earthquakes. Future work will include modeling the response of the sedimentary layers using the 1D structure from the USGS model under each SCV seismic station.

### 0.3 Acknowledgements

This research was supported by the USGS grants 99HQGR0057 and 00HQGR0048. The USGS velocity model provided by Robert C. Jachens of the U.S. Geological Survey was used. Ocean wave data were obtained from the National Data Buoy Center.

### 0.4 References

Dolenc, D., Basin structure influences on the teleseismic wave propagation in the Santa Clara Valley, California, *MS Thesis*, University of California, Berkeley, 2001.  
Jachens, R.C., Personal communications, 2000.

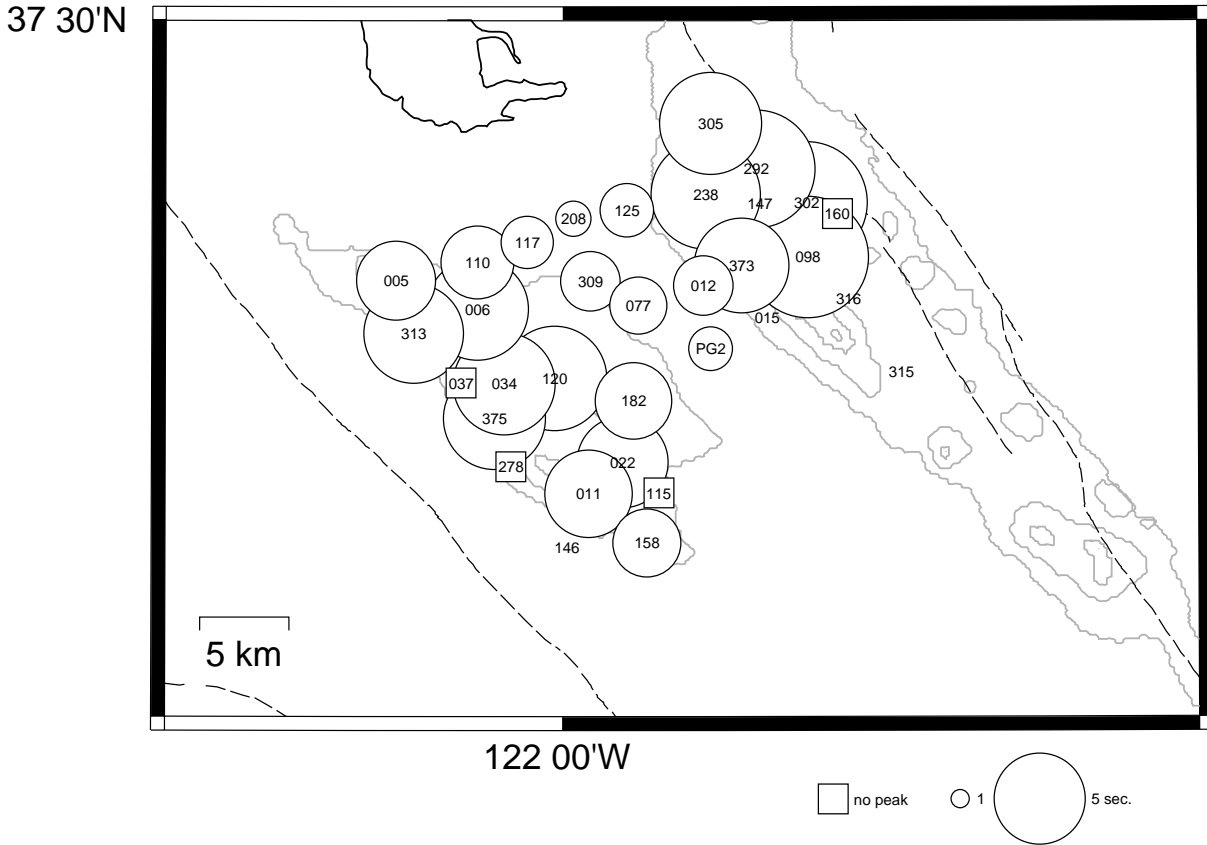


Figure 20.1: The periods of the dominant H/V spectral peaks in the 0.1 to 1 Hz frequency range. The numbers indicate locations of the SCV seismic stations and the circles indicate the periods of the H/V spectral peaks. Stations that showed no peak in the 0.1 to 1 Hz frequency range are shown by squares. Contours of the basins from the USGS model at 1 km, 3 km, 5 km, and 6 km are shown in gray. Dashed lines are the active faults in the region.

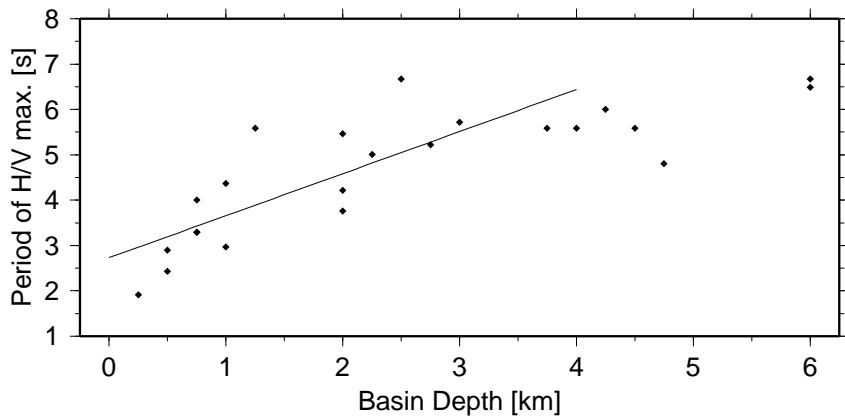


Figure 20.2: The period of the dominant H/V peaks as a function of the basin depth from the USGS model. Stations located above shallower than 4 km basins were used in regression and the resulting line fit is shown ( $y=0.93x+2.73$ ,  $R\text{-squared}=0.61$ ).

# Chapter 21

## Fluid Influenced Faulting in the Long Valley Volcanic Region

Dennise Templeton and Douglas Dreger

### 0.1 Introduction

We aim to better understand how an evolving hydrothermal system in an active volcanic region directly influences local earthquake production. Our ultimate interest is in the underlying source mechanism of these fluid influenced earthquakes and the factors that affect it. Towards that goal, we first determined the extent of fluid influenced faulting in the Long Valley volcanic region by computing moment tensor solutions from regional broadband data.

The Long Valley volcanic region, located in eastern California within the Sierra Nevada frontal fault system, includes the well-known active magmatic systems under Long Valley caldera and the Mono/Inyo Craters. For over two decades, the Long Valley caldera has been the center of unrest in the region exhibiting periods of increased seismicity, ground deformation, localized increases in concentrations of volcanic gases and subsurface magma movement (*Langbein et al.*, 1995 ; *Sorey et al.*, 1998 ). The Mono/Inyo Craters are a series of craters extending north from the caldera and are thought to have been created from a series of dikes over the past 40,000 years (*Bursik and Sieh*, 1989). To the south of the caldera is the Sierra Nevada mountain block, where there have been equivocal indications of magma existence even though there is a lack of evidence for recent volcanic or geothermal activity (*Hough et al.*, 2000 ; *Peppin et al.*, 1989).

In this study, we focused on a 100 km wide circular area centered at Long Valley caldera which includes the Mono/Inyo Craters and the seismically active Sierra Nevada block and comprehensively searched for events with coseismic volume changes.

### 0.2 Method and Results

Full moment tensor inversions solve for the complete moment tensor and can be decomposed into double-couple (DC), compensated-linear-vector-dipole (CLVD), and isotropic (i.e. volumetric) components. The presence of a significant volumetric component could indicate that fluids were involved in the source process of an earthquake. Deviatoric solutions a priori constrain the volumetric component to be zero. In this active geothermal and volcanic region, we did not wish to make this assumption. Therefore, we solved for both the deviatoric and full moment tensor solutions using three-component Berkeley Digital Seismic Network data at regional distances.

We studied 130 events with magnitudes greater than 3.5 since 1993. Seven stations were chosen for these inversions that provided the best azimuthal coverage and data quality. In practice however a solution would have a subset of these seven stations in its inversion depending on station availability and data quality issues. Green's functions were computed using the SoCal velocity model which is appropriate for the eastern California and Sierra Nevada regions (*Dreger and Helmberger*, 1993). Both data and Green's functions were bandpass filtered between 0.02 to 0.05 Hz using a causal Butterworth filter.

We used a nested F test to determine the probability that the additional volumetric component in the full moment tensor solution represented a true aspect of the source mechanism rather than being simply an added non-physical parameter in the inversion. We identified significant volumetric components if the improvement in fit to the data was at the 99 percent significance level between the deviatoric and full moment tensor solution.

Of the 130 earthquakes we originally identified, we were able to compute solutions for 83 events. The ensuing moment tensor catalog allowed us to determine the prevalence of events characterized by isotropic components. From these results we identified 17 earthquakes that had significant volumetric components as well as

good station coverage and data quality (Figure 21.1). These events all had between four and six stations in their inversions.

This investigation showed that fluid influenced earthquakes are fairly unique in the Long Valley volcanic region. The majority of these events were located within the Long Valley caldera or near the rim of the caldera. The remaining seven events were located in the seismically active Sierra Nevada block south of the caldera.

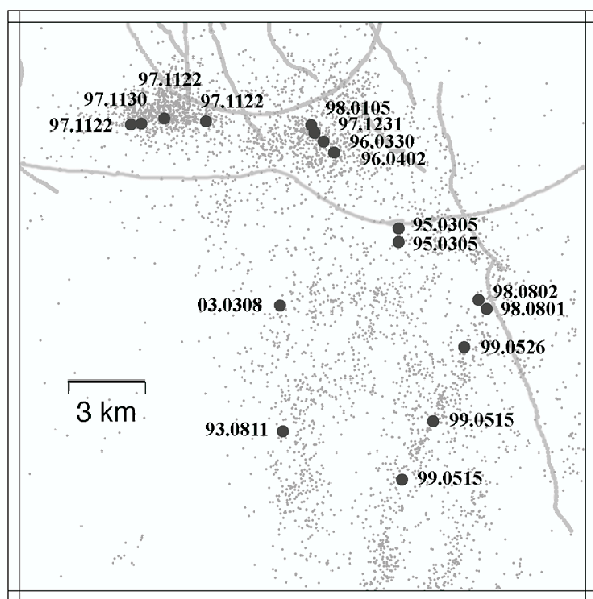


Figure 21.1: Location of events occurring between 1993-2003 with significant volumetric components labeled as YY.MMDD. Background seismicity is plotted as small gray dots. Faults, caldera rim, and resurgent dome plotted as solid gray lines.

### 0.3 Discussion

All events with significant volumetric components in the Long Valley caldera are located in the south moat or near the adjacent caldera rim. Seven of these events occurred in or near the location or time period of the November 1997 earthquake swarm. During and after this swarm there was also extensive independent evidence of magma migration from EDM, GPS, strainmeters, tiltmeters, and volcanic gas discharge rates. This magma migration could have affected the surface hydrothermal system in such a way as to cause these fluid influenced faulting events. The remaining two events were located near the epicenter of a  $M_L$ 6.1 May 1980 quake that had a large non-double couple component (*Julian and Sipkin, 1985*). It was never determined if this event had a volumetric component which would have conclusively

determined if fluids were involved. Long Valley caldera has an active geothermal system and thus it is not unexpected to find events with large isotropic components in this area (*Lachenbruch et al., 1976*).

It was surprising that earthquakes did not occur in or near the vicinity of the Mono/Inyo Craters. There is extensive evidence for the existence of magma under this volcanic chain and it is the expected location of the next volcanic eruption from this system (*Hill et al., 1985*; *Bursik and Sieh, 1989*). Perhaps this points to differences in the hydrothermal system or heat flux found in this area and with that found in the Long Valley caldera.

The most interesting result of this study was the number of fluid influenced earthquakes within the Sierra Nevada block when there has been no conclusive evidence of recent geothermal or magmatic activity in the area. However, there has been indirect evidence reported of magma bodies south of the caldera from pre-S phases and S-wave shadowing studies (*Peppin et al., 1989*). *Hough et al. (2000)* also identified several lines of equivocal evidence of magma or magmatic fluid involvement during an August 1998 earthquake sequence near the Hilton Creek fault. Earthquake activity in the Sierra Nevada block has always been assumed to be tectonic due to the absence of recent volcanism and present day geothermal features. However two major earthquakes occurring between 1978 and 1980 had large non-double couple components (*Julian and Sipkin, 1985*). Again, it was never determined if either of these events had large volumetric components.

Perhaps tectonic adjustment in the Sierra Nevada block could be providing a convenient conduit for hydrothermal fluids to migrate from their origin in the caldera to the mountain block via the north striking faults found in the area. In later studies we plan to explore the connection between fluid influenced faulting, the shallow hydrothermal system, and the deeper magmatic system.

### 0.4 Acknowledgements

We appreciate support for this project by NSF through contract EAR-0087147.

### 0.5 References

- Bursik, M. and K. Sieh, Range Front Faulting and Volcanism in the Mono Basin, Eastern California, *J. Geophys. Res.*, *94*, 15,587-15,609, 1989.
- Dreger, D.S. and D.V. Helmberger, Determination of source parameters at regional distances with three-component sparse network data, *J. Geophys. Res.*, *98*, 8107-8125, 1993.
- Hill, D.P., R.A. Bailey, and A.S. Ryall, Active tectonic and magmatic processes beneath LVC, eastern California: a summary, *J. Geophys. Res.*, *90*, 11,111-11,120, 1985.

Hough, S.E., R.S. Dollar, and P. Johnson, The 1998 earthquake sequence south of Long Valley Caldera, California: hints of magmatic involvement, *Bull. Seism. Soc. Am.*, *90*, 752-763, 2000.

Julian, B.R. and S.A. Sipkin, Earthquake Processes in the Long Valley Caldera Area, California, *J. Geophys. Res.*, *90*, 11,155-11,169, 1985.

Lachenbruch, A.H., M.L. Sorey, R.E. Lewis, and J.H. Sass, The Near-Surface Hydrothermal Regime of Long Valley Caldera, *J. Geophys. Res.*, *81*, 763-768, 1976.

Langbein, J., D. Dzurisin, G. Marshall, R. Stein, and J. Rundle, Shallow and peripheral volcanic sources of inflation revealed by modeling two-color geodimeter and leveling data from Long Valley caldera, California, 1998-1992, *J. Geophys. Res.*, *100*, 12,487-12,495, 1995.

Peppin, W.A., W. Honjas, T.W. Delaplain, and U.R. Vetter, The case for a shallow-crustal anomalous zone (magma body?) near the south end of Hilton Creek fault, California, including new evidence from an interpretation of pre-S arrivals, *Bull. Seism. Soc. Am.*, *79*, 805-812, 1989.

Sorey, M.L., W.C. Evans, B.M. Kennedy C.D. Farrar, L.J. Hainsworth, and B. Hausback, Carbon dioxide and helium emissions from a reservoir of magmatic gas beneath Mammoth Mountain, California, *J. Geophys. Res.*, *103*, 15,303-15,323, 1998.

## Chapter 22

# Source Mechanisms of Volcanic Induced Seismicity – Miyakejima, Japan, 2000

Sarah E. Minson, Douglas S. Dreger, and Roland Bürgmann (2001). In this study, all of the events were separately inverted in two frequency ranges: 0.01 to 0.033 Hz, and 0.02 to 0.05 Hz. Two types of moment tensor inversions were used: deviatoric and full moment tensor. In deviatoric inversions, the trace of the moment tensor is assumed to be zero, which implies that there is no volume change.

### 0.1 Introduction

Mount Oyama is a volcano on Miyakejima, Japan, part of the Izu Islands volcanic chain located south of Honshu. The most recent period of unrest at Mount Oyama began in June 2000, and this eruptive sequence included the largest recorded earthquake swarm in Japan (*Japan Meteorological Agency (JMA)*, 2000). More than 100,000 earthquakes were recorded in the next two months (*Ito and Yoshioka*, 2002). The seismic activity showed complex variations in space and time (*JMA*, 2000), but its most notable feature is that it migrated northwest with an offshore dike intrusion. Many of these earthquakes have large non-double-couple (NDC) components which might be indicative of fluid involvement in the seismic source process. In this study, linear moment tensor inversions in two passbands were used to establish the mechanism of eighteen of these earthquakes; GPS data were used to independently invert of the mechanism of two of these earthquakes and to forward predict the observed seismograms.

### 0.2 Moment Tensor Inversions

The methods of *Dreger et al.* (2000) and *Dreger and Woods* (2002) were used to investigate the mechanisms of eighteen events which occurred from June 29 to July 18, 2000 (UT). These eighteen events are comprised of the twelve events which the F-net network determined to have moment magnitudes of 5.5 or larger, plus six smaller events which were chosen because the F-net moment tensors had anomalous characteristics such as large NDC components or solutions with large variances.

Linear moment tensor inversions (*Pasyanos et al.*, 1996; *Dreger et al.*, 2000; *Dreger and Woods*, 2002), were used to invert complete, three-component, broadband seismograms recorded by the F-net network (Figure

22.1). In this study, all of the events were separately inverted in two frequency ranges: 0.01 to 0.033 Hz, and 0.02 to 0.05 Hz. Two types of moment tensor inversions were used: deviatoric and full moment tensor. In deviatoric inversions, the trace of the moment tensor is assumed to be zero, which implies that there is no volume change.

The depth of each event was established by performing independent moment tensor inversions at a range of depths to find which one produces the best fit to the data, and the ability of the synthetics to fit the data was assessed by the variance reduction (VR) (for example, *Dreger and Woods*, 2002), where a VR of 100% implies a perfect fit between the data and the synthetic seismograms. The stability of both the full moment tensor inversions and the deviatoric moment tensor inversions was examined by use of the jackknife test, in which data from every subset of the stations used in the original inversion are used to invert for the mechanism. Another type of source mechanism investigated was comprised only of isotropic and double-couple components (ISO+DC).

### 0.3 GPS Inversions

Data from ten GPS stations (Figure 22.1) operated by the Geographical Survey Institute of Japan (GSI) were used to determine displacements caused by EVT3 and EVT15, the two largest earthquakes in this sequence. The station located on the Izu peninsula was used as a reference station, and GPS displacements were calculated using the coordinates of each GPS station from the day before and after each earthquake. The nonlinear inversion methods of *Bürgmann et al.* (1997) were used to determine slip and rupture geometry. The length and width of the fault were constrained by the empirical scaling relationships between magnitude and rupture length and width which were reported in *Wells and Coppersmith* (1994), and the fault determined by the GPS inversion was required to be located within 5 km of the earthquake hypocenter reported by JMA.

## 0.4 Results

The majority of the events studied have large CLVD components which are consistent with the opening of a vertical crack (Figure 22.2, Figure 22.3). The results of the jackknife tests show that nearly all of the mechanisms are extremely stable. Extensional CLVD mechanisms such as the ones determined by this study have been repeatedly observed in volcanic areas and have been theorized to be the result of fluid injection (for example, *Kanamori et al., 1993; Julian and Sipkin, 1985*).

The full moment tensor inversions have an additional model parameter relative to the deviatoric inversions and ISO+DC grid searches. Therefore, it is necessary to determine whether the better fit of the full moment tensor mechanisms is statistically significant. The significance was examined by the use of multiple types of F-tests, but the partial F-test proposed by *Helsel and Hirsch (1992)* is considered to be most appropriate for this study. In the *Helsel and Hirsch (1992)* formulation, the F-test analyzes whether the specific parameter which was added to the model yields significant explanatory power in the presence of the other variables in the model. The results indicate that for at least twelve of these earthquakes, the moment tensors in both passbands have isotropic components which are statistically significant with more than 90% confidence, and half of the isotropic components are statistically significant with more than 99% confidence.

CLVD components can be caused by shear slip on two fault planes, but isotropic components cannot be formed from double-couples (*Julian et al., 1998*). Therefore, complex shear faulting can definitely be eliminated as the source of the NDC components of the mechanisms with statistically significant isotropic components. The orientation of the CLVD components of the earthquakes relative to the strike of the inferred dike (*Ito and Yoshioka, 2002; Toda et al., 2002*) and the observed seismicity indicate that these mechanisms may be consistent with tensile faulting due to opening along the dike.

The GPS data for EVT15 independently predict a mechanism that is very similar to the mechanism determined by the moment tensor inversions. Furthermore, synthetic seismograms generated using the mechanism determined by the GPS inversions fit the observed seismograms with a VR of 89.9%. This is particularly noteworthy because it shows that the GPS data can predict a completely independent data set.

The results of the GPS inversions for EVT3 are less conclusive. The GPS displacements on Miyakejima are consistent with deflation related to the magma chamber that was inferred to exist beneath the island, and they do not appear to be related to EVT3. Therefore, it was necessary to introduce a deflation source beneath the island in order to fit the GPS data, and this other deformation source probably affects the GPS inversion for the slip and geometry of the earthquake fault. The GPS data

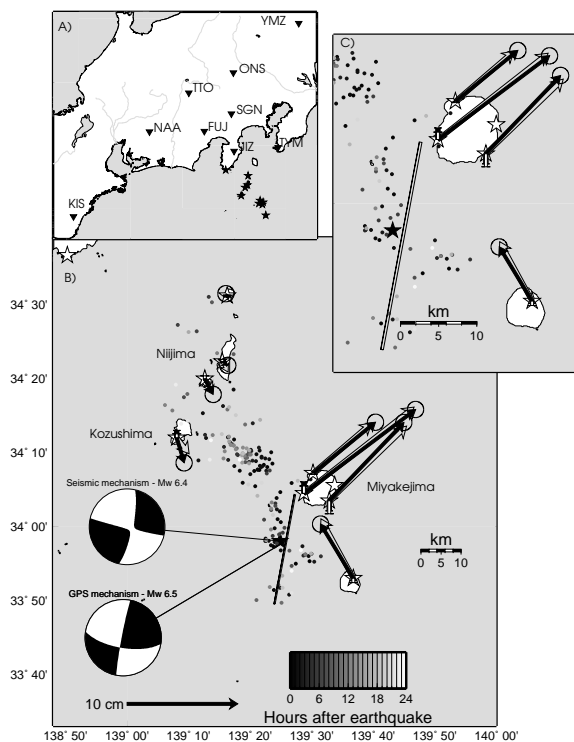


Figure 22.1: Study area and GPS inversion results for EVT15. **A.** Map showing location of F-net broadband seismograph stations and GSI GPS stations used in this study. F-net stations are denoted by triangles, and GSI stations are marked with stars. **B.** GPS inversion results for EVT15. Black arrows and vertical bar represent observed horizontal and vertical displacements, respectively. Clear arrows and yellow bars are predicted displacements. The fault determined by the GPS inversion is plotted as long with the seismicity reported in the Japan Meteorological Agency (JMA) catalog for the twenty-four hours following EVT15. The model fits the GPS data with a weighted residual sum of squares (WRSS) of 24.0053. **C.** Same as B. for the area near Miyakejima.

for EVT3 are clearly better fit by NDC mechanisms, just as the seismic data are much better fit by a NDC mechanism. However, the synthetic seismograms generated from the NDC GPS models do not fit the observed seismograms.

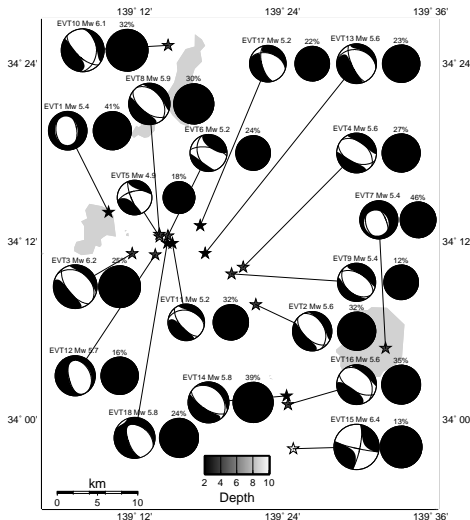


Figure 22.2: Full moment tensor mechanisms for the eighteen events in this study. The mechanisms in this figure were determined by full moment tensor inversions in the 0.02 to 0.05 Hz passband.

## 0.5 Conclusions

Moment tensor inversions for deviatoric, full moment tensor, and ISO+DC mechanisms in two frequency passbands were performed for eighteen earthquakes related to the eruption on Miyakejima, Japan in 2000. The majority of these events have large CLVD components which are consistent with the opening of a vertical crack (Figure 22.2). The orientation of these mechanisms relative to the dike intrusion and the observed seismicity indicate that these mechanisms might reflect tensile faulting related to inflation along the dike. Inversions of GPS data for EVT15 yield a slip model and fault geometry which does an excellent job of forward predicting the observed seismograms for that earthquake. However, the GPS data for EVT3 do not converge to a mechanism which fits the seismic data as well as the results of the GPS inversions for EVT15 do.

## 0.6 References

Bürgmann, R., P. Segall, M. Lisowski, and J. Svarc, Postseismic strain following the 1989 Loma Prieta earthquake from GPS and leveling measurements, *J. Geophys. Res.*, 102(3B), 4933-4955, 1997.

Dreger, D., and B. Woods, Regional distance seismic moment tensors of nuclear explosions, *Tectonophysics*, 356, 139-156, 2002.

Dreger, D. S., H. Tkalic, and M. Johnston, Dilational processes accompanying earthquakes in the Long Valley Caldera, *Science*, 288, 122-125, 2000.

Helsel, D. R., and R. M. Hirsch, *Statistical Methods in Water Resources, Studies in Environmental Science*, 49, pp. 296-299, Elsevier Science Publishers, Amsterdam, 1992.

Ito, T., and S. Yoshioka, A dike intrusion model in and around Miyakejima, Niijima, and Kozushima in 2000, *Tectonophysics*, 359, 171-187, 2002.

Japan Meteorological Agency, Recent seismic activity in the Miyakejima and Niijima-Kozushima region, Japan - the largest earthquake swarm ever recorded, *Earth Planets Space*, 52(8), i-vii, 2000.

Julian, B. R., and S. A. Sipkin, Earthquake processes in the Long Valley Caldera area, California, *J. Geophys. Res.*, 90(B13), 11,155-11,169, 1985.

Julian, B. R., A. D. Miller, and G. R. Foulger, Non-double-couple earthquakes, 1: Theory, *Rev. Geophys.*, 36(4), 525-549, 1998.

Kanamori, H., G. Ekstrom, A. Dziewonski, J. S. Barker, and S. A. Sipkin, Seismic radiation by magma injection: An anomalous seismic event near Tori Shima, Japan, *J. Geophys. Res.*, 98(B4), 6511-6522, 1993.

Pasyanos, M. E., D. S. Dreger, and B. Romanowicz, Toward real-time estimation of regional moment tensors, *Bull. Seismol. Soc. Am.*, 86(5), 1255-1269, 1996.

Toda, S., R. Stein, and T. Sagiya, Evidence from the AD 2000 Izu islands earthquake swarm that stressing rate governs seismicity, *Nature*, 419, 58-61, 2002.

Wells, D. L., and K. J. Coppersmith, New empirical relationships among magnitude, rupture length, rupture width, rupture area, and surface displacement, *Bull. Seismol. Soc. Am.*, 84(4), 974-1002, 1994.

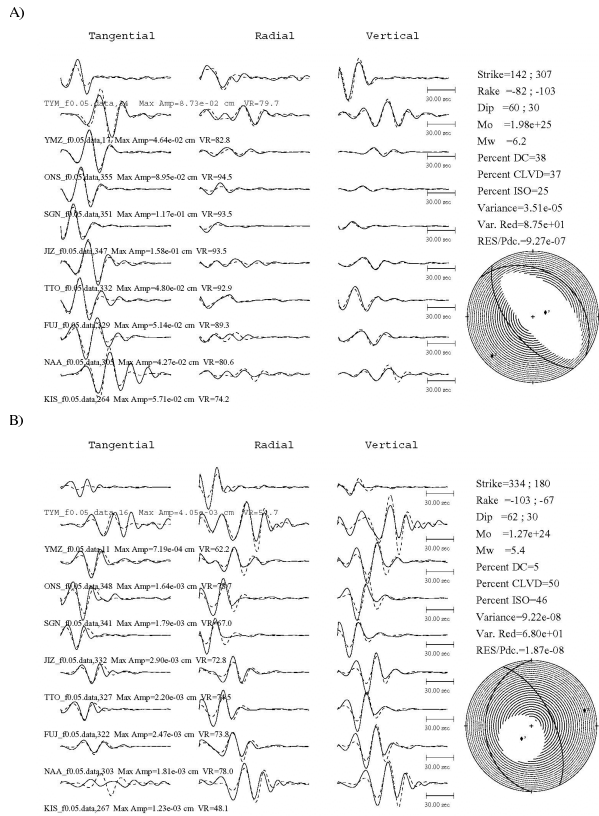


Figure 22.3: Waveform comparisons in the 0.02 to 0.05 Hz passband. **A.** Full moment tensor mechanism for EVT3. This mechanism has a large positive isotropic component which is consistent with inflation due to fluid injection. **B.** Full moment tensor mechanism for EVT7. The Phase of the Rayleigh waves does not appear to change, which is indicative of isotropic radiation. But the transverse seismogram has large amplitudes, and SH radiation should not be produced by an isotropic component. Therefore, this earthquake may have a complex mechanism consisting of both shear slip and an isotropic component, or it may have an inclined single-force mechanism. The depth of this event is unclear from the moment tensor inversions. But all three components are fit well at shallow depths which are consistent with inferred magma chamber depths. EVT7 occurred on the same day as a caldera began to form on Miyakejima, and it may be related to caldera collapse.

## Chapter 23

# Identifying and Removing Noise from the Ocean Bottom Broadband Seismic Data

David Dolenc, Barbara Romanowicz, and Bob Uhrhammer

### 0.1 Introduction

Ocean bottom broadband seismic observations show increased noise level when compared to land recordings. The signal-generated noise following the arrival of the seismic phases is one type of the observed noise, which is due to reverberations in the soft sediments and the water layer. Increased background noise, on the other hand, is generated, among others, by infragravity waves and ocean currents. Both types of noise can at least partially be removed from the seismic signal.

The data recorded at MOBB (Monterey Ocean Bottom Broadband station) were used. MOBB was installed 40 km offshore in the Monterey Bay at a water depth of 1000 m in April 2002 in a collaboration between Berkeley Seismo Lab and Monterey Bay Aquarium Research Institute (MBARI) (McGill *et al.*, 2002; Uhrhammer *et al.*, 2002). It comprises a three-component broadband seismometer with a temperature sensor, a water current meter measuring current speed and direction, and a differential pressure gauge (DPG). The station is continuously recording data which are retrieved every three months using the MBARI ROV "Ventana".

### 0.2 Signal-Generated Noise

An example of a large deep teleseism recorded at MOBB (black) and at the nearby island station FARB (gray) is shown in Figure 23.1. A strong signal-generated noise is observed at MOBB, probably due to reverberations in the mud layer in which MOBB seismometer is installed. This type of noise may be unavoidable in shallow buried installations. The transfer function describing the signal-generated noise in the sediments layer was calculated by the spectral division of the first 50 seconds of the MOBB and FARB records. The transfer function was then removed from the longer MOBB record to eliminate

the signal-generated noise (dashed).

Our future work will include analysis of other teleseismic events to obtain a robust transfer function, as well as 1D modeling of the soft sediments and water layer.

### 0.3 Background Noise

A comparison of a power spectral density (PSD) of the background noise recorded on the vertical component at MOBB and at three stations of the Berkeley Digital Seismic Network is shown in Figure 2. Data for a quiet and for a stormy day (determined from the wave height recordings from a nearby weather buoy) are shown. The background noise PSD between 30 and 500 sec is significantly different at MOBB. The observed peak is probably related to ocean currents and infragravity waves (Webb *et al.*, 1991; Webb, 1998). It is interesting that a similar peak can be observed at the island station FARB on the stormy day.

In our future work we plan to find the coherence between background noise and the ocean current, DPG data, temperature, and the ocean tides, and design filters to remove the coherent part of the noise. Previous studies successfully removed noise due to infragravity waves and ocean currents (Webb and Crawford, 1999; Crawford and Webb, 2000; Stutzmann *et al.*, 2001).

The results from this work may suggest future installation improvements for the deployment of permanent or temporary off-shore seismic broadband stations, such as have been discussed in the framework of the Ocean Mantle Dynamics (OMD) workshop (Snowbird, Fall 2002).

### 0.4 References

Crawford, W.C., and S.C. Webb, Identifying and removing tilt noise from low-frequency (<0.1 Hz) seafloor vertical seismic data, *Bull. Seism. Soc. Am.*, 90, 952-963, 2000.

McGill, P., D. Neuhauser, D. Stakes, B. Romanowicz, T. Ramirez, and R. Uhrhammer, Deployment of a long-term broadband seafloor observatory in Monterey Bay,

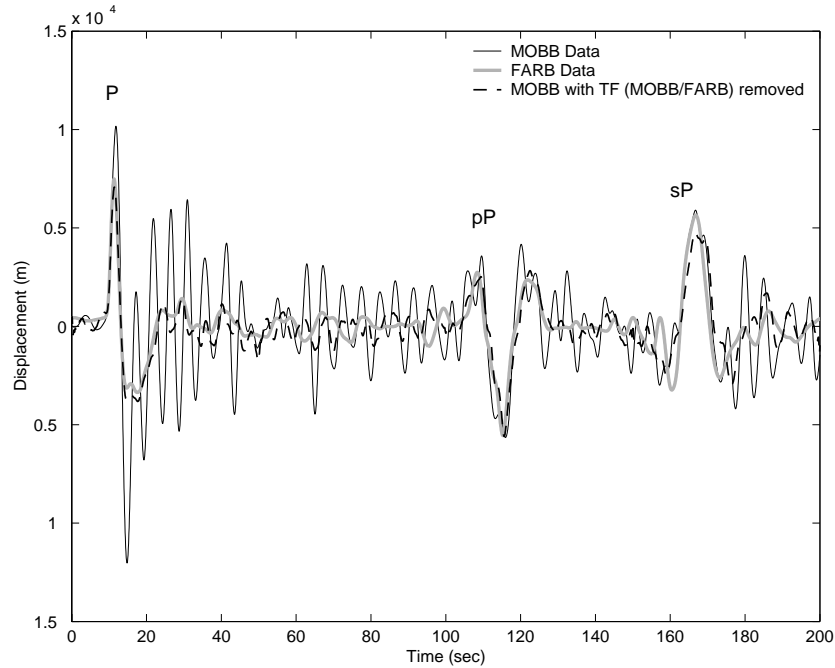


Figure 23.1: Vertical component recordings of a teleseism (Kurile Islands, 11/17/02,  $M_w=7.3$ , depth=459 km) at MOBB (black) and at the nearby island station FARB (gray). The two records were bandpass filtered between 0.03 and 0.3 Hz. Also shown is the MOBB record with the signal-generated noise removed (dashed). The arrivals of the P-, pP-, and sP-waves are indicated.

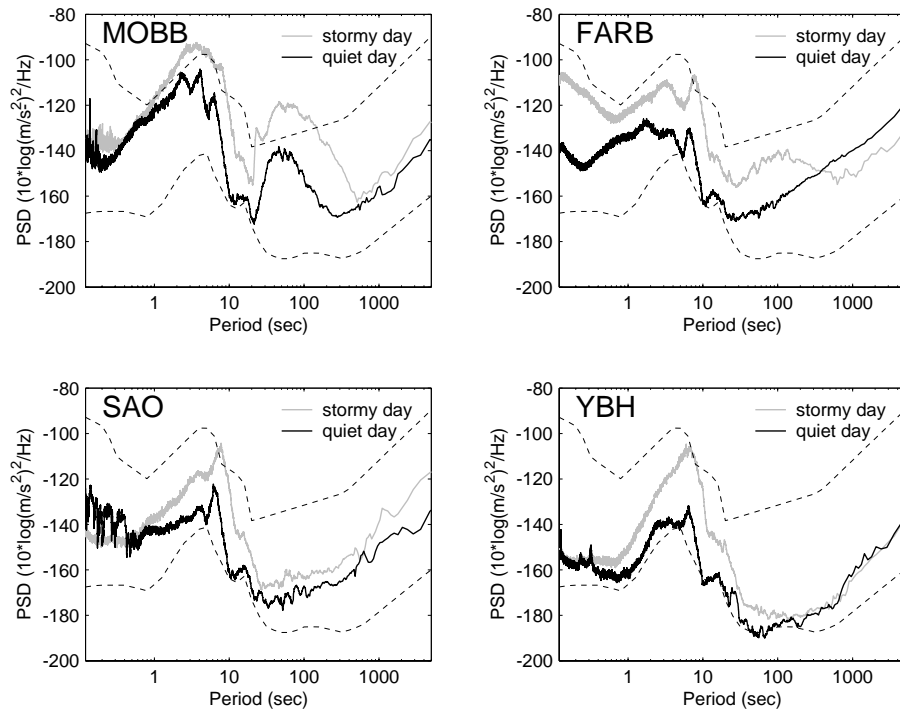


Figure 23.2: Background noise PSD observed at MOBB, FARB, SAO, and YBH vertical components. Shown are 4 hours data on a stormy (gray; 12/16/02), and on a quiet day (black; 05/23/02). The USGS high- and low-noise models for land stations are also shown (dotted).

*EOS Trans. Amer. Geophys. Un.*, 83, F1008, 2002.

Stutzmann, E., J.-P. Montagner, A. Sebai, W.C. Crawford, J.-L. Thiot, P. Tarits, D. Stakes, B. Romanowicz, J.-F. Karczewski, J.-C. Koenig, J. Savary, D. Neuhauser, and S. Etchemendy, MOISE: A prototype multiparameter ocean-bottom station, *Bull. Seism. Soc. Am.*, 91, 885-892, 2001.

Uhrhammer, R., B. Romanowicz, D. Neuhauser, D. Stakes, P. McGill, and T. Ramirez, Instrument testing and first results from the MOBB Observatory, *EOS Trans. Amer. Geophys. Un.*, 83, F1008, 2002.

Webb, S.C., X. Zhang, and W. Crawford, Infragravity waves in deep ocean, *J. Geophys. Res.*, 96, 2723-2736, 1991.

Webb, S.C., Broadband seismology and noise under the ocean, *Rev. Geophys.*, 36, 105-142, 1998.

Webb, S.C., and W.C. Crawford, Long-period seafloor seismology and deformation under the ocean waves, *Bull. Seism. Soc. Am.*, 89, 1535-1542, 1999.

## Chapter 24

# Detection of Long Period Surface Wave Energy

Junkee Rhie and Barbara Romanowicz

### 0.1 Introduction

Since the 1960s, array seismology has been developed mainly due to the need for detection of nuclear tests. Now there are many seismic arrays of various sizes in the world which are used for detecting nuclear tests, but also very weak but important seismic phases for refining fine-scale structure of the deep earth.

In this study, we are interested in weak low-frequency surface waves. Low-frequency surface waves are usually the dominant phases in waveforms generated from earthquake. They have been widely used for determining global earth structure and for the retrieval of earthquake source parameters. In addition, they can be used for detecting the existence of special types of seismic sources, such as slow/silent earthquakes (*Beroza and Jordan, 1990*), back ground free oscillations (*Ekström, 2001*) and other unknown sources. Usually, the low-frequency surface waves generated from these kinds of sources are too weak to be detected by a single station.

The main goal of this study is to detect weak energy from some low-frequency seismic sources and locate them. To do that, we need to design an optimal array method and guarantee this method to work. Hereafter we call this optimal method an array-based method.

### 0.2 An Array-Based Method

Most array methods are based on beam forming method (*Rost and Thomas, 2002*). Beam forming method can enhance the amplitudes of the same phases with an identical horizontal slowness  $\mathbf{u}$ . For body waves, each phase has a constant slowness, but surface waves are dispersive, that is, slowness is a function of frequency. Our array-based method is also based on beam forming, but it does not use constant slowness, it uses the dispersive property of surface wave. The following equation

describes the propagation of surface waves over a distance  $x$  from the source, in the frequency domain.

$$D(\omega, \theta, x) = S(\omega, \theta) \exp\left(\frac{-i\omega x}{C(\omega)}\right) \exp\left(\frac{-\omega x}{2U(\omega)Q(\omega)}\right)$$

where  $D$  is waveform in frequency domain at distance  $x$  and  $\theta$  is an azimuth.  $C$ ,  $U$  and  $Q$  are phase, group velocity and quality factor respectively. These parameters are obtained from a reference 1D model such as PREM (*Dziewonski and Anderson, 1981*). Although surface wave propagation is also affected by lateral heterogeneities, ellipticity and rotation of the Earth, PREM is a good approximation when the frequency band that we are interested in is low enough. By using the above equation we can align the surface waves with respect to a reference point within one array. The relative propagation distance is just a function of back azimuth when we assume plane wave propagation. The relation between back azimuth and waveform cannot be represented as a linear equation. Thus a model parameter search method can be used to measure back azimuth. The detailed process is as follows. We assume any back azimuth and imagine an imaginary source at 90 deg. away from the reference point (center of the array). Epicentral distances for all stations are calculated from an imaginary epicenter. We get relative distances between stations and the reference point by subtracting 90 deg. from calculated epicentral distances. The mapped waveform into reference point from each station can be calculated by using the above equation. Next process is to stack mapped waveforms to enhance coherent surface waves and reduce incoherent noise. The stacking can increase the possibility of detection by increasing the S/N ratio. Because neither do we have very dense distribution of stations nor all of them are quiet, stacking may not be able to increase the S/N ratio significantly. But in most cases, it can be helpful. The most common stacking method is a simple mean process, but we used N-th root stacking method. The advantage of this method is that it can severely reduce incoherent noises relative to a simple mean process,

but it can distort the waveforms after stacking (Muirhead and Datt, 1976). Now we have one stack from original recordings for a given back azimuth. If a given back azimuth is close to real one, amplitude of surface wave is preserved and incoherent noise is reduced. The final step is to apply moving time window and take averaged amplitude of recording in time window. The definition of averaged amplitude is

$$S\left(\frac{t_1 + t_2}{2}\right) = \sqrt{\frac{\int_{t_1}^{t_2} (v(t)w(t))^2 dt}{\int_{t_1}^{t_2} w(t)^2 dt}}$$

where  $w(t)$  is a taper function. The length and shift of time window will be different with respect to the applications and frequency content. In this study, we use a duration of 500 sec, shift of 100 sec and band pass between 50-200 sec. The above procedure is repeated for all possible back azimuths and then finally we can obtain averaged amplitudes as a function of time and back azimuth. We applied this array based method for three different arrays in the world during the period of January 2000.

### 0.3 Discussion

Our detection method is not completely established. Although we still need more refined detector which can identify signal from noise, the detection of the signal from large events ( $M_w > 6.0$ ) is obvious because they have much larger amplitudes relative to the back ground amplitude level. Figure 24.1 shows maximum averaged amplitudes in back azimuth as a function of time calculated for three different arrays - FNET (Japan), GRSN (Germany) and BDSN (Northern California). Because low-frequency displacement amplitudes are proportional to scalar seismic moment, maximum averaged amplitudes can be tied to  $M_w$  by introducing a scaling factor. Most signals due to large events can be clearly identified in all three arrays. The background noise levels are different for three arrays, GRSN shows much larger noise level than other two networks. This difference can be explained partly by different internal noise of seismometer in GRSN. GRSN consists of STS-2, but STS-1 is installed on other stations which are used in this study..

The final goal of application of array-based method is to detect and locate seismic sources. To check the reliability of the current method, we manually detect signals and compare their arrival time and back azimuth with those calculated from the earthquake catalog (Harvard CMT). There were 13 events with  $M_w$  larger than 6 in January, 2000. All 13 events are clearly detected for three arrays. Comparison result is written in following table.

As you can see in the table, all measured back azimuths are within 20 deg. from actual back azimuths and time differences between measured and calculated times are not significant. It indicates that we can locate the

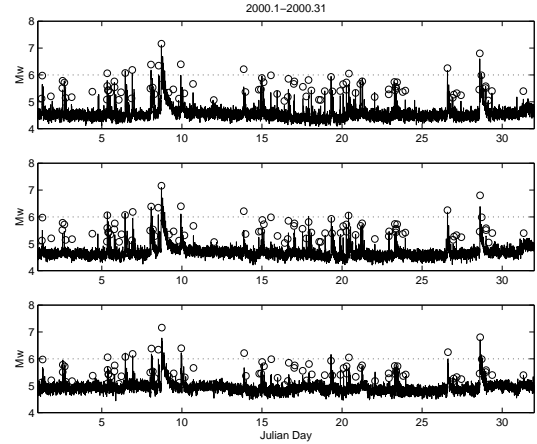


Figure 24.1: Maximum averaged amplitude plot for January, 2000. Amplitudes for FNET, BDSN and GRSN are shown from top to bottom. Small circles indicate arrival times and  $M_w$  for events listed in CMT. An arrival time is corrected by assuming group velocity of 3.8 km/sec

Event ID	Mw	Array	Time diff.	Baz1	Baz2
C010100B	6.0	FNET	-17 sec	172.20 deg	165 deg
		BDSN	-185 sec	214.64 deg	225 deg
		GRSN	249 sec	128.86 deg	115 deg
C010500C	6.1	FNET	19 sec	145.78 deg	140 deg
		BDSN	27 sec	251.38 deg	255 deg
		GRSN	92 sec	38.02 deg	40 deg
C010600C	6.1	FNET	24 sec	38.44 deg	45 deg
		BDSN	44 sec	337.46 deg	335 deg
		GRSN	121 sec	342.75 deg	345 deg
C010800A	6.4	FNET	80 sec	150.85 deg	145 deg
		BDSN	-3 sec	255.68 deg	255 deg
		GRSN	114 sec	42.74 deg	50 deg
C010800F	6.3	FNET	29 sec	69.11 deg	75 deg
		BDSN	117 sec	133.82 deg	135 deg
		GRSN	83 sec	248.76 deg	250 deg
C010800G	7.2	FNET	49 sec	130.20 deg	130 deg
		BDSN	31 sec	232.58 deg	235 deg
		GRSN	44 sec	8.06 deg	25 deg
C010900D	6.4	FNET	-39 sec	141.12 deg	135 deg
		BDSN	-165 sec	239.75 deg	240 deg
		GRSN	31 sec	28.35 deg	35 deg
C011300B	6.2	FNET	129 sec	134.42 deg	130 deg
		BDSN	-159 sec	236.03 deg	240 deg
		GRSN	165 sec	28.35 deg	15 deg
C011500C	6.0	FNET	-400 sec	137.17 deg	135 deg
		BDSN	-196 sec	233.03 deg	235 deg
		GRSN	95 sec	16.87 deg	20 deg
C012000D	6.1	FNET	-68 sec	50.73 deg	50 deg
		BDSN	21 sec	316.58 deg	300 deg
		GRSN	40 sec	331.01 deg	335 deg
C012600A	6.2	FNET	-35 sec	130.22 deg	130 deg
		BDSN	-39 sec	232.40 deg	235 deg
		GRSN	60 sec	8.23 deg	25 deg
C012800B	6.8	FNET	-88 sec	44.19 deg	50 deg
		BDSN	-64 sec	307.41 deg	305 deg
		GRSN	77 sec	31.02 deg	35 deg
C012800C	6.0	FNET	139 sec	230.22 deg	225 deg
		BDSN	-85 sec	305.34 deg	300 deg
		GRSN	38 sec	55.76 deg	55 deg

Figure 24.2: Table of detection result. Time difference means arrival time difference between observed and calculated ones. BAZ1 is back azimuth calculated from CMT and BAZ2 is measured back azimuth.

source from measured parameters. This result shows an array-based method can measure arrival time and back azimuth precisely enough to locate the source when energy released from the source is quite large. We still need to know the limit of detection and whether there is any detectable signal due to sources that are not standard events. To do that, we will apply this method on whole data of 2000 and look at other frequency bands.

## 0.4 References

Beroza, G. and T.H. Jordan, Searching for slow and silent earthquakes using free oscillations, *J. Geophys. Res.*, *95*, 2485-2510, 1990.

Dziewonski, A.M. and D.L. Anderson, Preliminary reference Earth model (PREM), *Phys. Earth Planet. Inter.*, *25*, 289-325, 1981

Ekström, G., Time domain analysis of Earth's long-period background seismic radiation, *J. Geophys. Res.*, *106*, 26,483-26,493, 2001.

Muirhead, K.J. and R. Datt, The N-th root process applied to seismic array data, *Geophys. J. R. Astr. Soc.*, *47*, 197-210, 1976.

Rost, S. and C. Thomas, Array seismology: Methods and applications, *Rev. Geophys.*, *40(3)*, 1008, doi:10.1029/2000RG000100, 2002.

## Chapter 25

# Automated Moment Tensor Software for Monitoring the Comprehensive Test Ban Treaty

Margaret Hellweg, Douglas Dreger, Barbara Romanowicz, Jeffrey Staley, and SAIC

### 0.1 Introduction

Seismology makes an important contribution toward monitoring compliance with the Comprehensive Test Ban Treaty (CTBT). An important task at the testbed of the Center for Monitoring Research (CMR, Washington DC, USA) and the International Data Center (IDC) of the Comprehensive Test Ban Treaty Organization (CTBTO, Vienna, Austria) is to detect, locate and characterize seismic events in order to distinguish between natural sources of seismic waves such as earthquakes, and other sources which might possibly be nuclear tests. For large events, this is not particularly difficult. However, small events, whether natural or man-made, present a greater challenge. While their epicenters and magnitudes can be determined fairly precisely using standard seismological methods, seismic moment tensor analysis can help in two ways. It gives information about the size and mechanism of a source in terms of its seismic moment and the moment tensor components. It provides, in addition, an estimate of the source's depth, which cannot always be reliably determined using normal location techniques. Thus, if an event has a large non double-couple component ( $> 50\%$ ) its source may be an explosion, possibly a nuclear explosion, while tectonic earthquakes typically have more than 70-80% double couple movement (*Dreger and Woods, 2002*). The source depth determined from moment tensor analysis may also help to weed out deep tectonic events from among the more than 100000 events of magnitude 4 and greater that occur annually. Only events at shallow depths need be scrutinized as part of the monitoring process of the Comprehensive Test Ban Treaty (CTBT).

This project's goal is to implement the procedure for

using seismic moment tensors routinely used in real-time at the University of California at Berkeley (UCB, *Romanowicz et al., 1993; Dreger and Romanowicz, 1994; Pasyanos et al., 1996*) on the testbed at CMR. Although the moment tensor procedure will not run in real-time on the testbed, in its final implementation it will run automatically, triggered from the Reviewed Event Bulletin (REB) and will be an additional, potentially powerful method for screening events (*Pechmann et al., 1995; Dreger and Woods, 2002*).

### 0.2 The Denali Sequence

The earthquakes which occurred in Alaska in October and November, 2002, provide an excellent opportunity for testing the moment tensor procedures. On the map in Figure 25.1A, the dots represent aftershocks in the sequence, while the locations of the mainshock, the foreshock and the four aftershocks we analyzed are shown as the large, medium-sized and small stars, respectively. We applied the CW moment tensor method to data from the foreshock on 23 Oct 2002, (FS,  $m_b(\text{NEIC})$  6.1 and  $m_b(\text{REB})$  5.5), and four aftershocks (AS1: 5 Nov, 07:50 UTC,  $m_b(\text{NEIC})$  4.9 and  $m_b(\text{REB})$  4.6; AS2: 08 Nov, 04:04 UTC,  $m_b(\text{NEIC})$  5.3 and  $m_b(\text{REB})$  5.1; AS3: 08 Nov, 17:34 UTC,  $m_b(\text{NEIC})$  5.2 and  $m_b(\text{REB})$  5.0; AS4: 08 Nov, 20:29 UTC,  $m_b(\text{NEIC})$  5.0 and  $m_b(\text{REB})$  4.7). The moment tensor calculated for the foreshock using data from three primary stations of the IMS network that had been filtered between 30 s and 100 s (mechanism south of FS) agrees well with that given in the Harvard CMT catalog. The fits between the synthetics and data are very good. It was notable that to achieve this fit, we had to use GFs for distances 100 km too short. This is very likely due to the fact that we use Greens functions calculated from the iasp91 velocity model. The actual seismic velocities under the North American continent are probably faster than those given

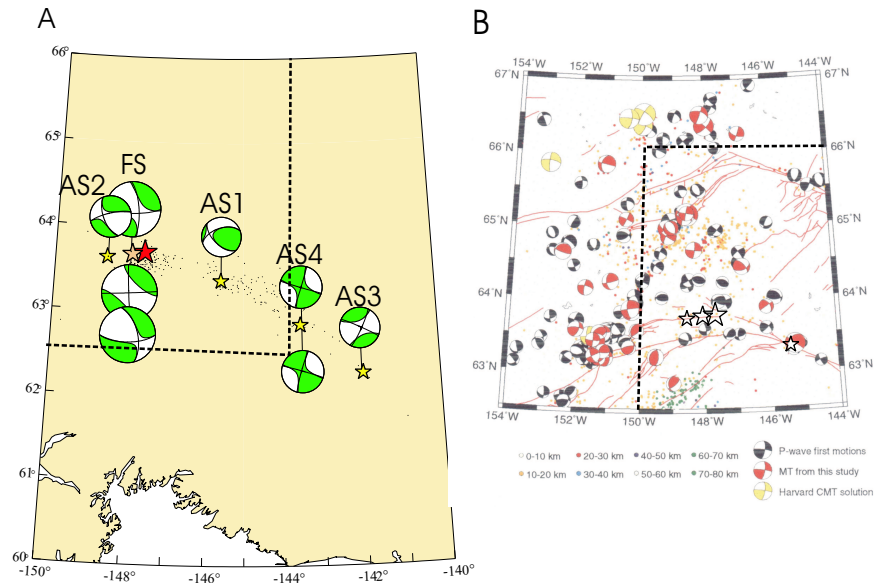


Figure 25.1: A: Epicentral locations of the Denali mainshock (large star), foreshock (medium-sized star) and the four aftershocks (small stars) analyzed. The dots show the epicenters other events in the sequence. Moment tensor solutions north of the epicenters were calculated using data filtered between 20 s and 50 s, those to the south were calculated from data filtered between 30 s and 100 s. The second solution south of FS was calculated using data for all stations. B: Mechanisms for recent Alaska seismicity given by *Ratchkovski and Hanson (2002)*. The dotted lines mark the areas of overlap between the two maps. Stars mark the locations of the mainshock, foreshock and the two aftershocks in the region of overlap.

in the model. *Ratchkovski and Hanson (2002)* have investigated recent seismicity in Alaska, producing mechanisms of many events in a region overlapping with some of the seismicity from the Denali sequence. Figure 25.1B shows their results. Both the foreshock and two of the aftershocks lie within the limits of their study. It is notable that the mechanisms north of the epicenters in Figure 25.1A, determined using data and GFs filtered between 20 and 50 s agree very well with the solutions for previous events located along the Denali Fault.

### 0.3 Acknowledgements

This research is sponsored by the Defense Threat Reduction Agency under contract DTRA01-00-C-0038.

### 0.4 References

Dreger, D. and B. Romanowicz, Source characteristics of events in the San Francisco Bay Region, *USGS Open-file report, 94-176*, 301-309, 1994.

Dreger D. and B. Woods, Regional Distance Seismic Moment Tensors of Nuclear Explosions, *Tectonophysics*, 356, 139-156, 2002.

Pasyanos, M., D. Dreger, and B. Romanowicz, Toward real-time estimation of regional moment tensors, *Bull. Seism. Soc. Am.*, 86, 1255-1269, 1996.

Pechmann, J.C., W.R. Walter, S.J. Nava, and W.J. Arabasz, The February 3, 1995,  $M_L$  5.1 seismic event in the Trona mining district of southwestern Wyoming, *Seis. Res. Lett.*, 66, 25-34, 1995.

Ratchkovski, N.A., Hansen, R.A., New Evidence for Segmentation of the Alaska Subduction Zone, *Bull. Seism. Soc. Am.*, 92, 1754-1765, 2002.

Romanowicz, B., M. Pasyanos, D. Dreger, and R. Uhrhammer, Monitoring of strain release in central and northern California using broadband data, *Geophys. Res. Lett.*, 20, 1643-1646, 1993.

## Chapter 26

# The Bay Area Velocity Unification (BĀVŪ); Bringing Together Crustal Deformation Observations from throughout the San Francisco Bay Area

Matthew A. d'Alessio, Ingrid A. Johanson, Roland Bürgmating, and the UC Berkeley Active Tectonics Group

### 0.1 Introduction

In an effort to put together the most comprehensive picture of crustal deformation in the San Francisco Bay Area, The UC Berkeley Active Tectonics Group has begun work on the Bay Area Velocity Unification (BĀVŪ “Bay-View”). This dataset unites campaign GPS data for nearly 180 GPS stations throughout the greater San Francisco Bay Area from Sacramento to San Luis Obispo. The BĀVŪ dataset includes data collected from 1991 to 2003 by U. C. Berkeley, the U.S. Geological Survey, the California Department of Transportation, Stanford University, U. C. Davis and the Geophysical Institute in Fairbanks, AK. These are combined with continuous GPS data from the BSL’s Bay Area Regional Deformation (BARD) network. The BĀVŪ dataset will form a consistent velocity field that will serve as the basis for monitoring fault slip and strain accumulation throughout the greater San Francisco Bay region.

### 0.2 Technical Overview of GPS Data Collection and Processing

#### Data Collection

At UC Berkeley we occupy each benchmark in our campaign GPS networks yearly. When possible, we collect data for at least two continuous 24 hour sessions, with some occupations spanning as long as seven days. However, much of the study area is in urban or suburban

unattended and limiting the occupation time to the logistical limits of the human operator. For these sites, occupations may be as short as 6 hours or as long as 12 hours, depending upon the time it takes to travel to the site and the efficiency of the operator. We usually repeat surveys of these sites at least once. Other agencies contributing data to the BĀVŪ dataset generally follow the same guidelines and provide at least 6 hours of data per site per day.

#### Processing Baselines

We process campaign GPS data using the GAMIT/GLOBK software package developed at the Massachusetts Institute of Technology, which uses double-difference phase observations to determine baseline distances and orientations between ground-based GPS receivers. Along with campaign data, we process five global stations from the International GPS Service (IGS) network and four to six nearby continuous stations from the BARD network. Cycle slips are automatically identified and fixed using the AUTCLN routine within GAMIT. We use standard models for satellite radiation pressure and tropospheric delay. Ambiguities are fixed using the widelane combination followed by the narrowlane, with the final position based on the ionospheric free linear combination (LC or L3). For baselines shorter than 500 meters, we calculate an additional solution using only L1 data. Baseline solutions are loosely constrained (100 m) until they are combined together.

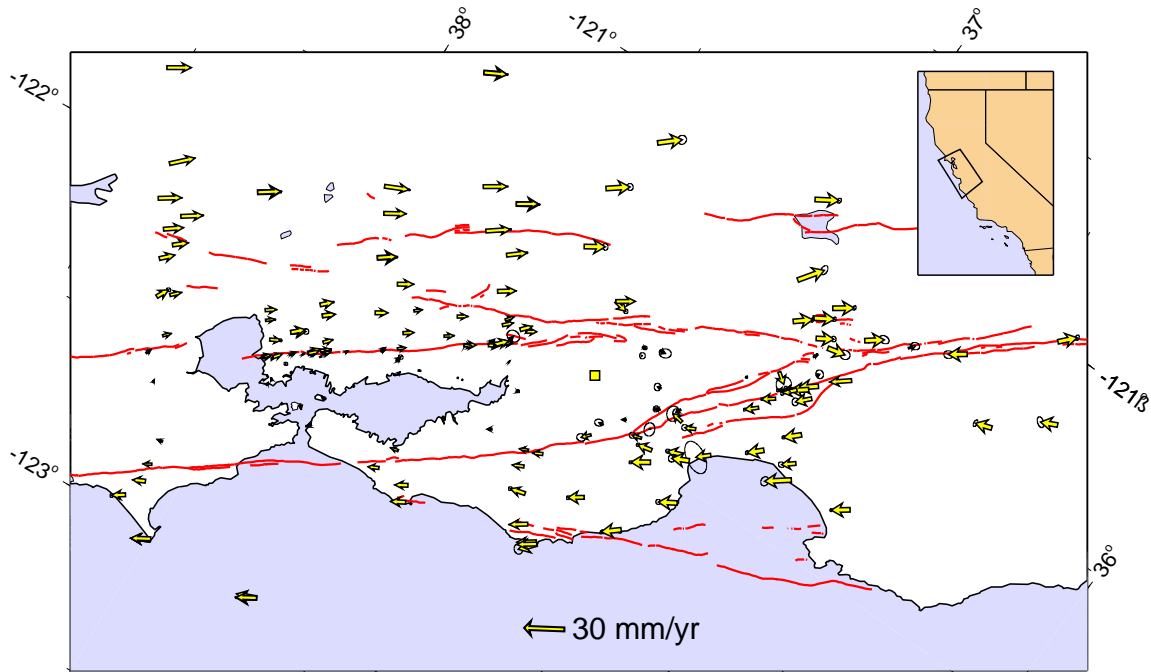


Figure 26.1: Map of the San Francisco Bay area in a Pacific Plate–Sierra Nevada block projection with GPS Velocities from 1994–2003 relative to station LUTZ in the Bay Block (yellow square). Velocities consistent with a small circle path predicted from the Euler pole of the Pacific Plate–Sierra Nevada block rotation show up as horizontal arrows.

### Combining Solutions

We combine daily ambiguity-fixed, loosely constrained solutions using the Kalman filter approach implemented by GLOBK. Within a given day, we include data processed locally as well as solutions for the full IGS and BARD networks processed by and obtained from SOPAC at the University of California, San Diego. During this combination, we weight each solution file relative to the other solution files for that day proportionally to the pre-fit chi-squared for the file when run through the Kalman filter independently. We uniformly scale the covariances of the entire combination so that the prefit chi-squared for the combined daily solution is approximately 1.0. Using the Kalman filter, we combine all daily solutions with equal weight to estimate the average linear velocity of each station in the network. We fix the final positions and velocities into the global reference frame using the GLOBK stabilization routine, allowing for rotation and translation of the network. Our final covariance matrix and the uncertainty estimates derived from it are scaled by the a posteriori chi-squared for the full combination. GLOBK also allows for the modeling of uncertainty using a benchmark wobble, but our current solutions have not included this effect.

### 0.3 GPS Results

Figure 26.1 shows GPS velocities for the entire BÄVÜ dataset relative to station LUTZ on the Bay Block. Be-

tween UC Davis and the Farallon Islands, we observe  $33\text{mm}\text{yr}^{-1}$  of relative displacement between the Pacific plate and the Sierra Nevada–Great Valley block of the North American plate. The Bay block shows up as a relatively undeformed block with many of the stations having velocities relative to LUTZ that are so small that they plot as dots in the figure.

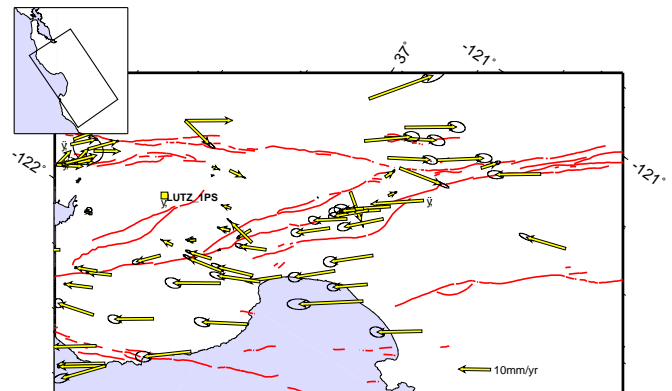


Figure 26.2: Map of deformation near the transition zone of the San Andreas Fault. Velocities relative to LUTZ on the Bay block.

## Southern Bay Area

The southern section of the BÄVÜ dataset includes the region affected by postseismic deformation following the Loma Prieta earthquake (Fig. 26.2). To avoid "contamination" of the regional deformation pattern by transient processes, we have not included data in this area collected before 1994. The southern Bay Area exhibits mostly fault-parallel right-lateral motion, with no indication of the fault-normal compression observed in the Foothills thrust belt immediately after the Loma Prieta Earthquake (Bürgmann, 1997). Other transient processes such as several slow earthquakes on the Central San Andreas fault are captured by the dataset, but their effect is likely small when spread over several years. The future inclusion of InSAR data in the BÄVÜ dataset will allow the identification of some transient deformation events that the GPS networks are too sparse to capture. It should also improve our ability to measure surface creep.

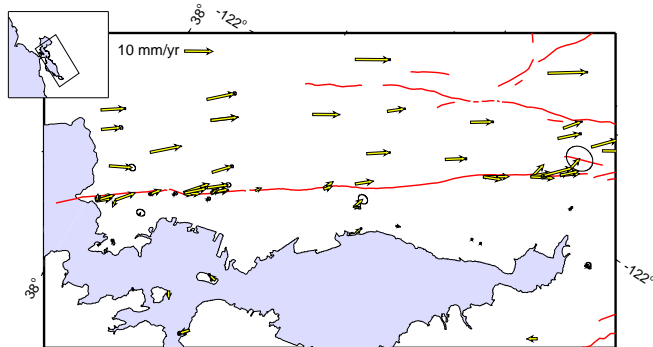


Figure 26.3: Map of deformation near the Hayward fault. Velocities relative to LUTZ on the Bay block.

## Hayward Fault

BÄVÜ includes 64 stations within 15 km of the Hayward fault distributed along strike and in profiles perpendicular to the fault (Fig. 26.3). Creep along the Hayward fault allows the Bay block to slide past the East Bay Hills block with only minimal internal deformation and strain accumulation within either block. The BÄVÜ model allows us to quantify the exact creep rate and place relative displacement across the fault in a regional context to quantify strain accumulation. Figure 26.4 shows observed variations in creep rate along strike of the Hayward fault.

These variations reflect both the spatial distribution of strain accumulation and temporal variations in creep rate. This is highlighted by comparisons between the BÄVÜ GPS data and trilateration and triangulation collected by the US Geological Survey for the past several decades (grey lines in Fig. 26.4). Places where BÄVÜ deviates most from the long-term observations by the USGS are places where the USGS indeed shows different

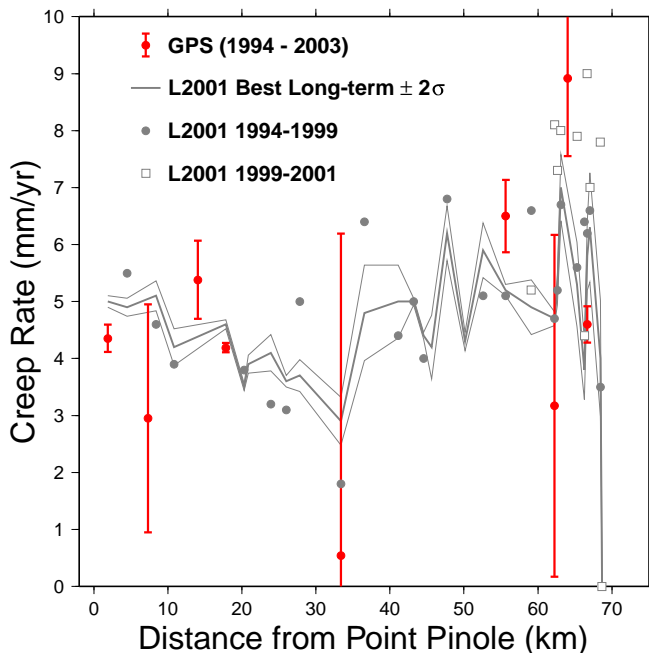


Figure 26.4: Variations in surface creep rate as a function of distance along strike of the Hayward fault. GPS data from the BÄVÜ model agree fairly well with the terrestrial geodetic results of Lienkaemper, 2001 ("L2001"). Note how the creep rate from L2001 is different for different time periods. Because BÄVÜ and L2001 cover slightly different time periods, some of the differences between the two results likely reflects actual temporal fluctuations in creep rate.

creep rates on shorter time scales (grey circles and open squares in Fig. 26.4). Observations from five to ten year periods (such as the nine-years covered in BÄVÜ) can deviate from longer-term observations by more than  $2\sigma$ . These fluctuations in creep rate must therefore be considered when using observations from BÄVÜ to estimate long-term elastic strain accumulation and probabilistic earthquake magnitudes.

## 0.4 References

- Bürgmann, R., L. P. Segall, M. Lisowski, and J. Svarc, Postseismic strain following the 1989 Loma Prieta earthquake from GPS and leveling measurements, *J. Geophys. Res.*, 102(B3), 4933-4955, 1997.
- Lienkaemper, J.J., J.S. Galehouse, and R. W. Simpson, Long-term monitoring of creep rate along the Hayward fault and evidence for a lasting creep response to 1989 Loma Prieta earthquake, *Geophys. Res. Lett.*, 28 (11), 2265-2268, 2001.

## Chapter 27

# Crustal Deformation Along the Northern San Andreas Fault System

Mark H. Murray

### 0.1 Introduction

The San Andreas fault system in northern California includes three sub-parallel right-lateral faults: the San Andreas, Ma'acama, and Bartlett Springs. This northernmost segment is the youngest portion of the fault system, forming in the wake of the northwestwardly propagating Mendocino triple junction where the Pacific, North America, and Gorda (southern Juan de Fuca) plates meet. The Pacific plate moves about 35-40 mm/yr relative to central California across a broad  $\sim 100$ -km zone in northern California. Additional deformation in eastern California and the Basin and Range province contribute to the total relative Pacific-North America motion of  $\sim 50$  mm/yr. The San Andreas fault itself has been essentially aseismic and accumulating strain since it last ruptured in the great 1906 San Francisco earthquake, and no major earthquakes have occurred during the historical record on the more seismically active Ma'acama, and Bartlett Springs faults, which are northern extensions of the Hayward-Rodgers Creek and Calaveras-Concord-Green Valley faults in the San Francisco Bay area.

In *Frey Mueller et al.* (1999) we used GPS data collected in 1991-1995 along two profiles crossing the faults near Ukiah and Willits (Figure 27.1). GPS velocities from these profiles constrain the total deep slip rate on the San Andreas fault system to be  $39.6^{+1.5}_{-0.6}$  mm/yr (68.6% confidence interval). Although deep slip rates on the individual faults are less well determined due to high correlations between estimated slip rates and locking depths, and between slip rates on adjacent faults, the slip rate on the Ma'acama fault ( $13.9^{+4.1}_{-2.8}$  mm/yr) implies that it has now accumulated a slip deficit large enough to generate a magnitude 7 earthquake and therefore poses a significant seismic hazard.

In this renewed and ongoing study, we are resurveying

the original profiles and adding two new profiles to the north and south (Covelo and Healdsburg, respectively, in Figure 27.1). Most of the monuments were last observed in 1993 or 1995, so the new observations significantly improve the velocity estimates, and we expect they will improve models of average interseismic strain accumulation, including possible spatial variations along the fault system. These 10-station profiles every 50 km from Pt. Reyes to Cape Mendocino form a primary monitoring network for future observations to detect temporal variations in deformation. We plan to survey 40 additional stations in the southern portion of the network in Fall 2003 to provide better monitoring along the Rodgers Creek and Ma'acama faults.

### 0.2 Geodetic Measurements

The survey of the 4 primary profiles was conducted during January-March 2003 after verifying the benchmarks were still suitable for GPS observations, and picking or installing substitutes at the few that were not. Most of the stations were occupied for 6.5-8 hours on two different days. Some sites in the Central Valley or in the higher portions of the Coast Ranges that were not occupied due to weather or logistical considerations will be included in the Fall 2003 survey. Altogether, 43 site positions were measured during 94 session occupations, with the assistance of students and staff of the BSL.

We processed the data using GAMIT/GLOBK software using many of the same techniques used to process the BARD observations (*Murray and Segall*, 2001). These distributed processing methods allow the solutions to be combined in a self-consistent fashion with other solutions, such as for the BARD network, and for more global networks provided by the SOPAC analysis center, using Kalman filtering techniques, providing a well-defined velocity reference frame with respect to the stable North America. We are now reprocessing the older observations in GAMIT/GLOBK to tie all the northern California observations together in a self-consistent manner.

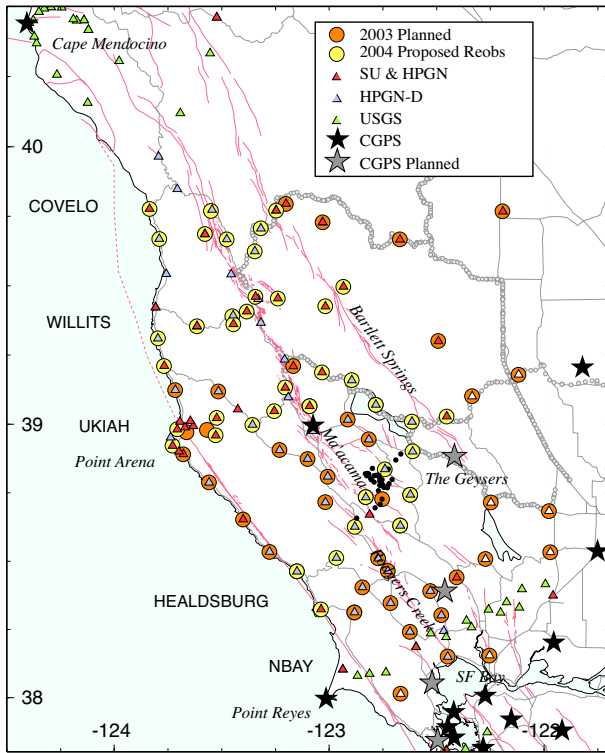


Figure 27.1: GPS sites along the northern San Andreas fault system. Light circles, sites that were observed in early 2003. Dark circles, stations with planned occupations in Fall 2003. Profile names are capitalized. USGS conduct surveys along the NBAY profile and near Cape Mendocino. Only one continuous GPS station (HOPB) currently operates in this region.

These data sets include Stanford surveys of the profiles, NGS surveys of the HPGN network, USGS surveys of the Covelo profile, and Caltrans surveys of the HPGN-Densification sites.

### 0.3 Deformation

Figure 27.2 shows site velocities for the 1994-2003 period relative to stable North America, as defined by a set of 20 fiducial stations. Most of the velocities were derived from data spanning 8-10 years, whereas those with the largest error ellipses include data from only a 4 year span (most of these stations will be reoccupied in Fall 2003). The easternmost stations exhibit motions typically associated with Sierran-Great Valley block (ORLA: 12.5 mm/yr NW). The westernmost sites are moving close to the Pacific plate rate (PTAR: 45.9 mm/yr NW). Fault-normal contraction is observed east of the Ma'acama fault, in the region of the Coast Ranges near the Central Valley where similar contraction has been observed elsewhere (e.g., Murray and Segall, 2001).

The North America reference frame used in this anal-

ysis is an improvement over the single-station approach used in the Freymueller *et al.* (1999) study, and allows us to apply angular velocity-fault backslip modeling techniques (e.g., Murray and Segall, 2001) to account for both far-field plate motions and interseismic strain accumulation. We are modifying a set of algorithms provided by Brendan Meade of MIT that sums backslip on rectangular dislocations to extend our simple 2D method to more complex, 3D fault systems (including subduction zones and extensional provinces). We are currently testing it on a variety of problems, such as the Adriatic region with M. Battaglia and R. Bürgmann, and it appears to be well suited to study the northern San Andreas fault system and its transition to the Cascadia subduction zone.

The velocity orientations do not closely follow the mapped traces of the faults in the northernmost section, as one might expect from pure elastic strain accumulation on the faults. We will assess whether this is a result of the Sierran-Great Valley block impinging on the San Andreas fault system, or a strain effect caused by the Mendocino fracture zone. We will determine realistic uncertainties of our strain accumulation models using the bootstrap techniques, and test methods for adding geologic and other information using Bayesian techniques to test whether the additional information can reduce the correlations and provide better resolution on other parameters. For example, the slip-rate and locking depth (10.5-22.6 mm/yr and 4.7-44.6 km, 95% confidence) on the San Andreas fault should be much better resolved by applying constraints derived from other seismic, geodetic, and paleoseismic observations.

### 0.4 Acknowledgements

We appreciate support for this project by the USGS NEHRP through grant numbers 02HQGR0064 and 03HQGR0074. We thank André Basset, Maurizio Battaglia, Dennise Templeton, and especially Todd Williams for assistance conducting the survey.

### 0.5 References

- Freymueller, J. T., M. H. Murray, P. Segall, and D. Castillo, Kinematics of the Pacific-North America plate boundary zone, northern California, *J. Geophys. Res.*, *104*, 7419-7442, 1999.
- Murray, M. H., and P. Segall, Modeling broadscale deformation in northern California and Nevada from plate motions and elastic strain accumulation, *Geophys. Res. Lett.*, *28*, 4315-4318, 2001.

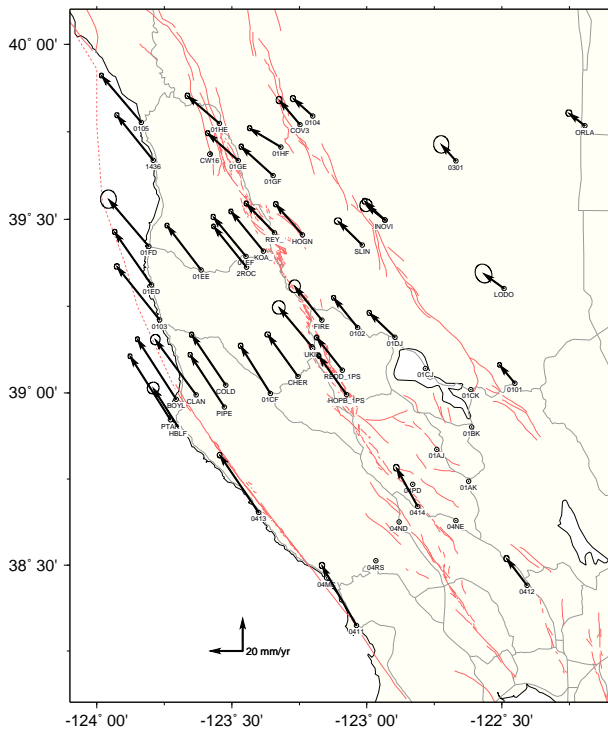


Figure 27.2: Velocities of sites in the Coast Ranges relative to North America, with 95% confidence regions assuming white-noise process only. Sites without velocities were observed in early 2003; data from their initial occupation in 1994 or 1999 is currently being processed.

## Chapter 28

# Surface Creep Measurements from a Slow Earthquake on the San Andreas Fault Using InSAR

Ingrid A. Johanson and Roland Bürgmann

### 0.1 Introduction

The ubiquity of slow earthquakes (SEQs) on faults (both dip-slip and strike-slip), suggests that they are a fundamental mode of strain release. The fact that they characteristically occur in the transition region between steadily slipping and locked faults may allow us to draw general conclusions about the mechanism by which faults transition between locked and creeping. To date, the San Andreas Fault near San Juan Bautista is the only location where slow earthquakes have occurred on an accessible strike-slip fault. The slip in these events was much closer to the surface than in the typical subduction zone events, making it a unique and potentially very effective location to study the mechanics of slow slip. Three slow earthquakes occurred along the SAF in 1992, 1996 and 1998; each with moment magnitude close to that of the largest seismic earthquakes in the area ( $M_w$ 5.5). In this report we focus on the 1998 SEQ, whose shallow depth (less than 5 km) and compact size of the slow earthquakes (relative to subduction zone SEQs), provides the opportunity to apply the high spatial resolution and good precision of InSAR to observing the deformation pattern of SEQs (Johanson and Bürgmann, 2002).

### 0.2 1998 SEQ

The 1998  $M_w$ 5.0 slow earthquake was immediately preceded by the  $M_w$ 5.1 San Juan Bautista earthquake (Uhrhammer *et al.*, 1999) (Large blue circle in Fig. 28.1). The two events were located in the same region, with the slow earthquake rupturing the portion above 5km (Gwyther *et al.*, 2000). The earthquake and SEQ ruptures were of comparable size and resulted in similar

amounts of slip. An interferogram spanning from Aug. 18 1997 to Oct. 12 1998 contains adequate coherent data along the central San Andreas to observe near fault movement (Fig 28.2). The interferogram contains a sharp phase gradient aligned with the fault trace. If the range-change signal is attributed to purely strike-slip motion on the San Andreas Fault, then the interferogram indicates right-lateral slip of about the same amount observed by creepmeters. It is expected, however, that the measured range change will contain some vertical motion and may also contain atmospheric errors. We are working on incorporating ascending track frames and increasing the total number of available interferograms to account for these effects.

### 0.3 Near Field Fault Motion

Fig. 28.3 compares surface creep measurements made using InSAR to those from creepmeters. Red points were obtained by averaging phase values every 350 meters along strike and 50 meters away from each side of the fault. Pairs of average phase measurements were differenced and converted to San Andreas parallel strike-slip movement. Error bars are the standard deviations of values in each bin. Though the InSAR and creepmeter data match well, the InSAR data suggest that fault movement is much more variable than would be inferred from creepmeters alone. However, the variability may be the result of a poorly defined fault trace. Figure 28.3 also makes it apparent that the contribution of the slow earthquake to surface slip during the time spanned by the interferogram is small; the difference between the blue and green triangles. The contribution of interseismic creep must therefore be accounted for before slip is attributed to the SEQ. The variability in the InSAR data makes it a requirement that we use interseismic creep rates with similar spatial sampling. We are working on creating interferogram stacks using a patch-work method that will

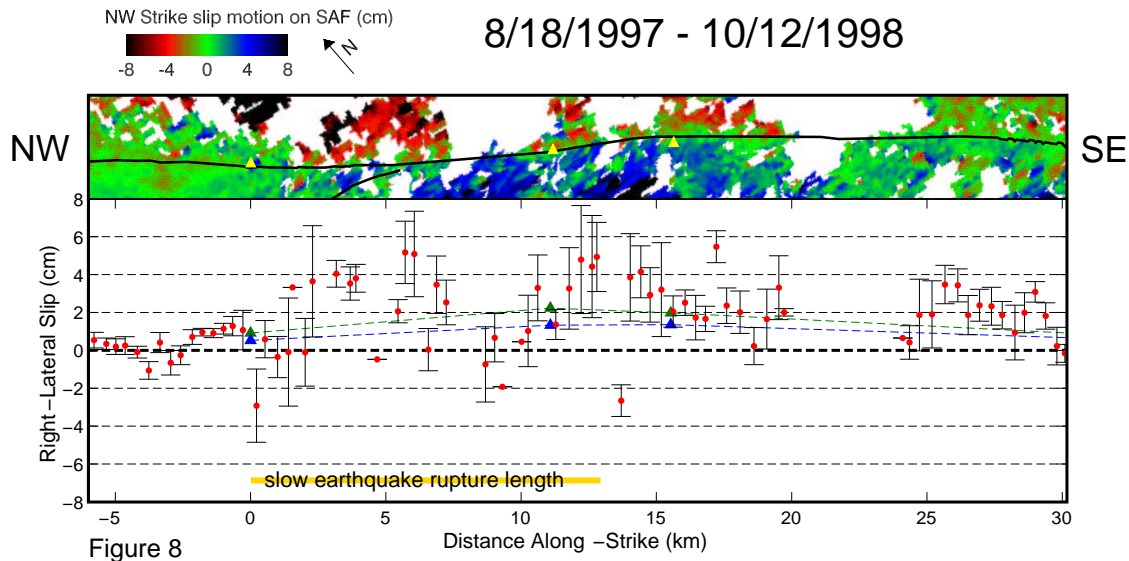


Figure 28.3: Comparison of near field motion measured using InSAR and creepmeters XSJ, XHR and CWN. Green triangles are the total amount of creep measured by creepmeters during the time span of the interferogram and includes secular creep, the 1998 slow earthquake and the San Juan Bautista earthquake. Blue triangles are the amount of creep expected without the 1998 slow earthquake or San Juan Bautista earthquake. The interferogram shown is a subset of Track 299 Frame 2861; its location is shown in Figure 28.1.

allow us to define average creep rates along the San Andreas.

### 0.4 Conclusions

InSAR is capable of measuring small scale movement such as creep. The interferogram shown here suggests that creep along the Central San Andreas varies considerably along strike. Future modelling of the fault system will benefit from the dense spatial sampling of InSAR. However, the contribution of the 1998 San Juan Bautista slow earthquake to the total range change is very subtle and will require careful removal of the interseismic signal.

### 0.5 References

Gwyther, R. L., C. H. Thurber, M. T. Gladwin, and M. Mee, Seismic and aseismic observations of the 12th August 1998 San Juan Bautista, California M5.3 earthquake, *3rd San Andreas Fault Conference*, Stanford University, 209-213, 2000

Johanson, I. A. and R. Bürgmann, An investigation of slow earthquakes on the San Andreas Fault using InSAR, *EOS Transactions, AGU*, 83(47), 357, 2002

Uhrhammer, R., L. S. Gee, M. H. Murray, D. Dreger and B. Romanowicz, The  $M_w$ 5.1 San Juan Bautista, California earthquake of 12 August 1998, *Seismological Research Letters*, 70(1), 1999.

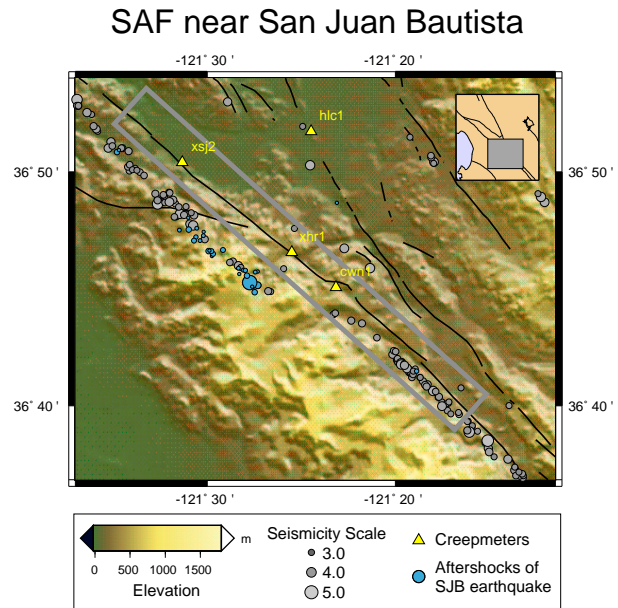
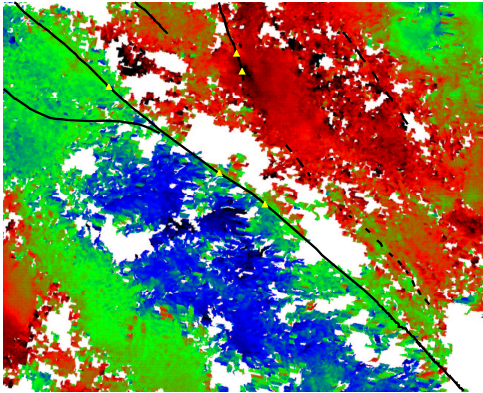


Figure 28.1: Location map of the Central San Andreas Fault showing local background seismicity and creepmeter locations. Also shown is the main and aftershocks of the 1998 San Juan Bautista earthquake (in blue). The grey box outlines the profile shown in Figure 28.3.

8/18/1997 - 10/12/1998



Time Span = 1.15 yrs  
⊥ Baseline = 69 m

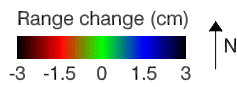


Figure 28.2: Subset of an interferogram from Track 299 Frame 2861 corresponding in area to the location map in figure 28.1. The interferogram contains significant topography correlated signal which are probably atmospheric errors. However, creep occurs on a scale much smaller than most atmospheric errors

## Chapter 29

# Evidence of Powerlaw Flow in the Mojave Mantle

Andrew Freed and Roland Bürgmann

### 0.1 Introduction

Laboratory experiments suggest that rocks in the lower crust and upper mantle (shallower than 200 km) should deform by dislocation creep, characterized by a strain rate proportional to stress raised to a power,  $n$  (e.g., Kirby and Kronenberg, 1987; Carter and Tsepp, 1987). Dislocation creep has not yet been confirmed by geodetic observations. We use GPS campaign and continuous time-series data associated with 1992 Landers and 1999 Hector Mine earthquakes to infer rheologic properties of the Mojave lithosphere in southern California. The coupled nature of these earthquakes (20 km and 7 years apart) makes them ideal for a stringent rheology study in that a candidate rheologic model must satisfy the postseismic observations associated with both events. To infer the nature of viscous flow we developed a finite element model of this earthquake sequence that simulates coseismic slip associated with both events (Wald and Heaton, 1994; Dreger and Kaverina, 2000), a regional background strain rate (Savage and Svarc, 1997), and temperature dependent powerlaw rheologies (Hirth et al., 2001; Kronenberg and Tullis, 1984; Shelton and Tullis, 1981; Jaoul et al., 1984; Hansen and Carter, 1982). We consider a range of powerlaws (for felsic and mafic, wet and dry rocks) reflecting uncertainty in the mineralogy of the lithosphere and in the extrapolation from laboratory to geologic conditions. Thermal gradients are constrained from surface heat flow measurements (Williams, 1996) and regional seismic velocities (Melbourne and Helmberger, 2001). For comparison purposes, we also consider models with a Newtonian (strain rate linearly proportional to stress) rheology.

### 0.2 Results

Our results show that the spatial and temporal evolution of transient surface deformation following the Landers and Hector Mine earthquakes can be successfully explained by powerlaw flow ( $n = 3.5$ ), predominantly in a warm and wet upper mantle. These results are characterized by model and data comparisons shown in Figure 29.1. We can rule out Newtonian flow as a reasonable explanation of both the spatial and temporal patterns of postseismic transient motions, implying that the common assumption of Newtonian flow in numerical models of ductile deformation within the crust and upper mantle (e.g., Thatcher et al., 1980; Miyashita, 1987; Deng et al., 1998; Pollitz et al., 2001, 2002) may be invalid. These results suggest that recovery-controlled dislocation creep is the dominant mechanism of viscous flow following earthquakes. The model results also preclude significant flow in the lower crust, supporting the contention that, at least beneath the Mojave Desert, the mantle is the weaker region.

The stress dependence of powerlaw flow inferred by our calculations means that the viscosity of the upper mantle changes as a function of time after an earthquake. This has implications for models of regional stress changes and fault interaction. For example, the influence of earthquake induced stress changes on neighboring faults will evolve more rapidly early on, but will last many decades longer than would be inferred from a Newtonian model. Furthermore, as viscosities are lowest where stresses are highest, a powerlaw rheology leads to a more localized shear zone beneath faults where coseismic stresses are highest. For example, our calculations show that a Newtonian model of post-Landers relaxation leads to a broad, diffuse shear zone in the mantle beneath the Landers rupture zone about 250-300 km wide. In contrast, post-Landers relaxation of a powerlaw rheology leads to a relatively narrow shear zone 70-90 km wide, with much of the shear concentrated in a central zone only 15 km wide.

### 0.3 Acknowledgements

Funding provided by NSF grant #EAR 0207617

### 0.4 References

Carter, N. L. and M. C. Tsenn, Flow properties of continental lithosphere, *Tectonophysics*. 136, 27-63, 1987.

Deng, J., M. Gurnis, H. Kanamori, E. Hauksson, Viscoelastic flow in the lower crust after the 1992 Landers, California, earthquake, *Science* 282, 1689-1692, 1998.

Dreger, D. and A. Kaverina, Seismic remote sensing for the earthquake source process and near-source strong shaking; a case study of the October 16, 1999 Hector Mine earthquake, *Geophys. Res. Lett.*, 27, 1941-1944, 2000.

Hansen, F.D. and N.L. Carter, Creep of selected crustal rocks at 1000 MPa, *Trans. Amer. Geophys. Union* 63, 437, 1982.

Hirth, G., C. Teyssier, W. J. Dunlap, An evaluation of quartzite flow laws based on comparisons between experimentally and naturally deformed rocks, *Int. J. Earth Sci.* 90, 77-87, 2001.

Hudnut, K.W., N.E. King, J.G. Galetzka, K.F. Stark, J.A. Behr, A. Aspiotes, S. van-Wyk, R. Moffitt, S. Dockter, F. Wyatt, Continuous GPS observations of postseismic deformation following the 16 October 1999 Hector Mine, California, earthquake ( $M_w = 7.1$ ), *Bull. Seismo. Soc. Amer.* 92, 1403-1422, 2002.

Jaoul, O., J. A. Tullis, A. K. Kronenberg, The effect of varying water contents on the creep behavior of Heavittree Quartzite, *J. Geophys. Res.* 89, 4298-4312, 1984.

Kirby, S.H. and A.K. Kronenberg, Rheology of the lithosphere; selected topics, *Rev. Geophys.* 25, 1219-1244, 1987.

Kronenberg, A. K. and J. A. Tullis, Flow strengths of quartz aggregates; grain size and pressure effects due to hydrolytic weakening, *J. Geophys. Res.* 89, 4281-4297, 1984.

Melbourne, T. and D. Helmberger, Mantle control of plate boundary deformation, *Geophys. Res. Lett.*, 28, 4003-4006, 2001.

Miyashita, K., A model of plate convergence in Southwest Japan, inferred from leveling data associated with the 1946 Nankaido earthquake, *J. Phys. Earth* 35, 449-467, 1987.

Pollitz, F.F., G. Peltzer, and R. Brügmann, Mobility of continental mantle; evidence from postseismic geodetic observations following the 1992 Landers earthquake, *J. Geophys. Res.*, 105, 8035-8054, 2000.

Pollitz, F.F., C. Wicks, and W. Thatcher, Mantle flow beneath a continental strike-slip fault; postseismic deformation after the 1999 Hector Mine earthquake, *Science* 293, 1814-1818, 2001.

Savage, J.C. and J.L. Svarc, Postseismic deformation associated with the 1992  $M (sub w) = 7.3$  Landers earth-

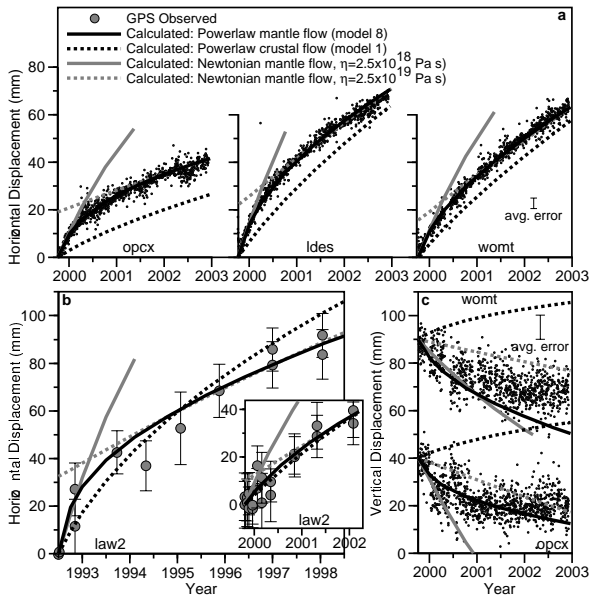


Figure 29.1: Comparison of representative observed and calculated postseismic displacement time-series following the 1992 Landers and 1999 Hector Mine earthquakes. (a) Horizontal displacements at 3 continuously monitored GPS stations following 1999 Hector Mine earthquake. (b) Horizontal displacements at campaign GPS station law2 following the 1992 Landers quake (22). Inset shows campaign data at station law2 following the Hector Mine quake. (c) Vertical motions at 2 continuously monitored stations following 1999 Hector Mine earthquake. Powerlaw mantle flow model (solid black curves) is a model of aplite and wet olivine. Powerlaw crustal model (dotted black curves) is a model of wet quartzite and dry olivine. Newtonian models consider purely mantle flow with low viscosity ( $2.5 \times 10^{18}$  Pa s, solid grey curves) and an order of magnitude higher viscosity (dotted grey curves) that match early and late time-series slopes, respectively. Curves associated with the high viscosity Newtonian model have been raised to show where the slopes match the observed time-series. These results show that a powerlaw model of flow in the mantle can satisfy that time-series data, but not a model of lower crustal or Newtonian flow.

quake, Southern California, *J. Geophys. Res.*, *102*, 7565-7577, 1997.

Shelton, G. and J. A. Tullis, Experimental flow laws for crustal rocks, *Trans. Amer. Geophys. Union* *62*, 396, 1981.

Thatcher, W., T. Matsuda, T. Kato, and J. B. Rundle, Lithospheric loading by the 1896 Riku-u earthquake, northern Japan; implications for plate flexure and asthenospheric rheology *J. Geophys. Res.*, *85*, 6429-6435, 1980.

Wald, D.J. and T. H. Heaton, Spatial and temporal distribution of slip for the 1992 Landers, California, earthquake, *Bull. Seismol. Soc. Am.*, *84*, 668-691, 1994.

Williams, C.F., Temperature and the seismic/ aseismic transition; observations from the 1992 Landers earthquake, *Geophys. Res. Lett.*, *23*, 2029-2032, 1996.

# Chapter 30

## Intraplate Strain Accumulation in the New Madrid Seismic Zone

Mark H. Murray, Mark D. Zoback (Stanford University), Paul Segall (Stanford University)

### 0.1 Introduction

The New Madrid seismic zone (NMSZ) in the central United States is the most seismically active intraplate region in North America. It includes two SW-NE-trending zones of right-lateral strike-slip faulting on subvertical faults and a zone of thrust faulting on  $30^\circ$  SW-dipping plane at a left step-over between the strike-slip fault zones (Figure 30.1). Three widely felt magnitude  $\sim 7$ – $8$  earthquakes occurred in the  $\sim 250$  km zone in the the winter of 1811–1812, and the central thrust zone was sufficiently displaced during the 7 February 1812 event to create a waterfall on the Mississippi river.

The NMSZ is located within a failed rift that was active about 600 million years ago, followed by period of magmatic reactivation and igneous intrusion of mafic plutons 80 to 60 million ago. These episodes of activity introduced heterogeneities into the crust that may act as stress concentrators for the late Holocene seismicity, possibly initiated by the most recent deglaciation event (*Grolimund and Zoback, 2001*). Paleoseismic evidence indicates that 1811–1812 sized events have occurred throughout the late Holocene, most recently around 1450 and 900 A.D., but the small cumulative fault offsets inferred from seismic reflection data suggest that the current high level of seismic activity initiated recently, and there is scant paleoseismic evidence for more than 4 episodes prior to the historic events.

Low rates of strain and the lack of apparent active surface tectonics suggest that the central and eastern U.S. are within the stable interior of the North America plate. Geodetic studies of broadscale deformation within this region generally find that relative station velocities are consistent ( $< 1$  mm/yr) with a rigid plate with strain rates not significantly differing from zero. High strain rates ( $\sim 100$  nanostrain/yr) were reported within a network spanning the southern NMSZ based on a 1991 GPS

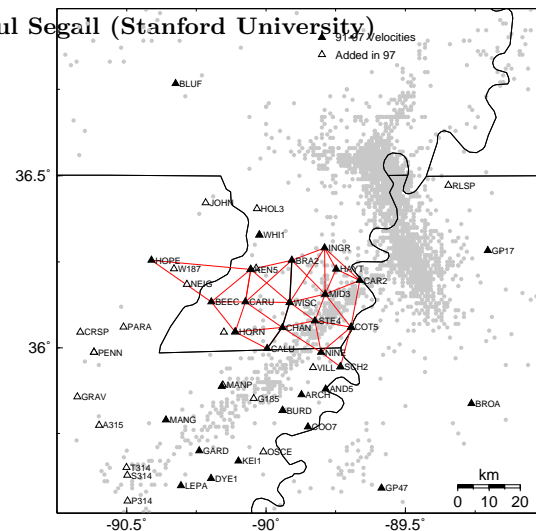


Figure 30.1: GPS and triangulation networks along the southern New Madrid seismic zone. Circles are earthquake epicenters. Solid triangles are sites occupied in the 1991, 1993, and 1997 surveys with estimated velocities. Open triangles are sites installed in the 1997 survey. Thin lines connecting some of the sites represent the triangulation network that was occupied in the 1950's. *Liu et al.* [1992] estimated uniform shear strain rates for the entire network, as well as the east and west portions divided by the bold line.

survey and triangulation data collected in the 1950's (*Liu et al., 1992*). We present new strain rate estimates within this southern NMSZ network from GPS surveys conducted in 1993 and 1997 that show the recent deformation rates are not significantly greater than zero.

### 0.2 Geodetic Measurements

The primary network consists of triangulation benchmarks installed in the mid-1950's that were reoccupied

using GPS in 1991 by NGS. Enough of the benchmarks had survived to allow 40-year averaged shear-strain rates to be estimated. This network was reoccupied by GPS in 1993 and 1997 and stations were added to better span the southern seismic zone and the western rift boundary (Figure 30.1).

We processed the data from the 3 GPS surveys using GAMIT/GLOBK software using many of the same techniques used to process the BARD observations (*Murray and Segall, 2001*). Definition of a self-consistent reference frame is complicated by major changes to the global fiducial network that occurred between the 1991 and 1993 surveys. To better define the velocity frame throughout this period, we included SOPAC global solutions obtained for 45 days, at 64-day intervals, between March 1991 and December 1998. These solutions provide sufficient observations to estimate the positions and velocities of the fiducial stations included in our NMSZ analysis during each interval between significant changes of the station equipment and reference monuments. We defined a North America frame by minimizing the horizontal velocities of 15 stations, which had an rms deviation of 3.5 mm in position and 0.5 mm/yr in velocity.

### 0.3 Deformation

The velocities of 32 sites in the NMSZ region are well determined with respect to the North America frame (Figure 30.2). The average horizontal velocity of the 32 stations relative to North America is  $1.7 \pm 0.8$  mm/yr at  $N8^\circ E$ , which significantly differs from zero (all quoted uncertainties are 95% confidence). The apparent average northward motion is due primarily to stations located in the interior of the network, whereas the average motion of the outlying stations (BLUF, HOPE, GP47, BROA, GP17) is  $1.0 \pm 1.4$  mm/yr,  $N10^\circ E$ , consistent with their being on stable North America.

We estimated strain rates using 1950's triangulation data to compare with the *Liu et al. (1992)* results. Because triangulation data are relatively insensitive to distances and the scale of the network, we estimated engineering shear strain rates,  $\dot{\gamma}_1 = \dot{\epsilon}_{EE} - \dot{\epsilon}_{NN}$  and  $\dot{\gamma}_2 = \dot{\epsilon}_{EN} + \dot{\epsilon}_{NE}$ , from which the maximum shear-strain rate  $\dot{\gamma}$  and direction of maximum contraction can be derived. *Liu et al. (1992)* found that shear-strain rates in a 22-station network (Figure 30.1) were significantly greater than zero, particularly in the western half of the network that spans the rift boundary, with  $\dot{\gamma} = 248 \pm 140$  nanoradian/yr. Using the same stations, but including GPS data from all 3 years, we find the estimated shear strain rates in all cases do not significantly differ from zero. For example,  $\dot{\gamma}$  using all or just the western stations is  $64 \pm 68$  or  $134 \pm 140$  nanoradian/yr, respectively. Therefore, in contrast to the 1992 study, we find no evidence for high strain rates in the southern New Madrid seismic zone.

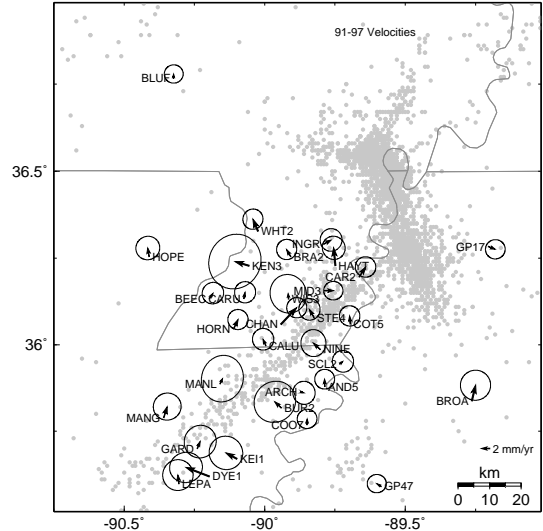


Figure 30.2: Velocity of stations relative to stable North America estimated from the 1991, 1993, and 1997 surveys. The error ellipses represent 95% confidence regions that assume formal errors scaled by the misfit scatter plus  $2 \text{ mm yr}^{-1/2}$  random walk to account for possible benchmark instability, which could be significant for the shallowly anchored benchmarks in 500-m deep Mississippi embayment sediments.

The average motion of the interior stations relative to the outlying stations is  $1.0 \pm 0.6$  mm/yr,  $N6^\circ E$ , with the most central stations tending to have velocities slightly elevated above this level. The spatial coherence of this pattern suggests that some deformation—albeit marginally significant—may be present in the region. Projecting the average motion onto the  $N45^\circ E$  seismic trend yields  $0.7$  parallel and  $-0.6$  mm/yr perpendicular components, which is opposite of that predicted by simple elastic strain dislocation models that assume zero far-field deformation and backslip on the faults defined by seismic and paleoseismic studies. We are currently investigating alternative explanations for this tantalizing signal, such as from a gravitational instability of the underlying rift pillow (*Pollitz et al., 2002*), or from the relaxation of a weakened lower crustal zone proposed by *Kenner and Segall (2000)*. This latter model, which predicts low rates of strain consistent with our geodetic observations, shows that low strain rates do not necessarily preclude the possibility of repeating large intraplate earthquakes, and that the seismic hazards in the NMSZ are still likely to be high.

### 0.4 Acknowledgements

We appreciate previous support for this project by the NSF. We thank Stacy Kerkela, Stephanie Prejean, and the staff and students of CERI in Memphis, Tennessee

for assistance conducting the 1997 survey.

## 0.5 References

Grollimund, B., and M. D. Zoback, Did deglaciation trigger intraplate seismicity in the New Madrid seismic zone?, *Geology*, 29, 175-178, 2001.

Kenner, S. J., and P. Segall, A mechanical model for intraplate earthquakes: Application to the New Madrid seismic zone, *Science*, 289, 2329-2332, 2000.

Liu, L. B., M. D. Zoback, and P. Segall, Rapid intraplate strain accumulation in the New Madrid seismic zone, *Science*, 257, 1666-1669, 1992.

Murray, M. H., and P. Segall, Modeling broadscale deformation in northern California and Nevada from plate motions and elastic strain accumulation, *Geophys. Res. Lett.*, 28, 4315-4318, 2001.

Pollitz, F. F., L. Kellogg, and R. Bürgmann, Sinking mafic body in a reactivated lower crust: A mechanism for stress concentration in the New Madrid Seismic Zone, *Bull. Seismol. Soc. Am.*, 91, 1882-1897, 2002.

## Chapter 31

# The Adriatic Region: An Independent Microplate within the Africa-Eurasia Collision Zone

Maurizio Battaglia, Mark H. Murray and Roland Bürgmann

model of regional deformation. This approach incorporates the secular velocities from GPS, fault geometry estimates and elastic-strain accumulation, making possible to determine how different tectonic hypothesis are compatible with geodetic data.

### 0.1 Introduction

In this study we use surface velocities recorded by GPS measurements and block modeling to investigate the active deformation of the Adriatic region, a component of the zone of distributed deformation between the African and Eurasian plates. The region includes the relatively stable Adriatic area (Po Valley, Adriatic Sea and Apulia), surrounded on the eastern, northern and western margins by a mountain belt which includes the Albanides, the Dinarides, the Alps and the Apennines. The southern margin of the Adriatic region, representing the boundary with the African plate, is still undefined. This study was prompted by a need to resolve the uncertainty surrounding the tectonic representation of this area, alternatively viewed as a promontory of North Africa or as a microplate within the Africa-Eurasia plate boundary.

The absence or low level of seismic activity in the Adriatic Sea indicates that its behavior is that of a relatively rigid plate within a deforming region. The bulk motion of the plate can be described as rigid rotation about an Euler pole in North Italy. Fault plane solutions suggest that the motions at the boundaries of the Adriatic area may not reflect directly Africa-Eurasia convergence. Some authors question the existence of an independent Adriatic plate, suggesting that a counterclockwise rotation of the Adriatic block, driven by impingement of the Africa plate against the Calabrian Arc, may explain the major tectonic events in the region, such as the opening of the Tyrrhenian basin, the evolution of the Apenninic-Maghrebian chain, the extension in the northern Ionian basin, and the shortening process along the Alps-Dinarides-Ellepidonides. On order to test the competing tectonic models proposed, we plan to develop a block

### 0.2 Deformation Velocities

We employ publicly available GPS observations made at 30 stations of the European Reference Permanent Network (EUREF) and the Italian Space Agency (ASI) continuous GPS networks to estimate deformation in the Adriatic region (Figure 31.1). We analyze the data using the GAMIT/GLOBK software in a three step approach described by (*McCluski et al*, 2000). To improve the realization of a stable reference frame for the velocity solution, additional sites from the International GPS Service (IGS) and EUREF networks are included through the publicly available global regional loosely constrained solutions performed by the Scripps Orbit and Permanent Array Center (SOPAC). Given the small velocities (from 2 to 5 mm/yr) recorded along the Italian peninsula, the choice of the appropriate definition of a stable Eurasian frame of reference may be critical.

The velocities shown in Figure 1 are referenced to the stable Eurasian frame, based on 15 stable sites in Europe and Asia (*McCluski et al*, 2000). All together, our solution includes data spanning 4 years from 138 stations, including 45 in the Mediterranean area. We incorporate 50 additional sites from publicly available solutions (*McCluski et al*, 2000) to resolve the deformation in the Eastern Mediterranean and Caucasus. To better assess the real uncertainties of the GPS solutions, we scale the covariances of the daily and monthly average to be consistent with the internal residual scatter of their combinations (i.e., chi-square statistics are approximately 1). These scalings do not compensate for systematic reference frame biases, possible non-Gaussian errors or pos-

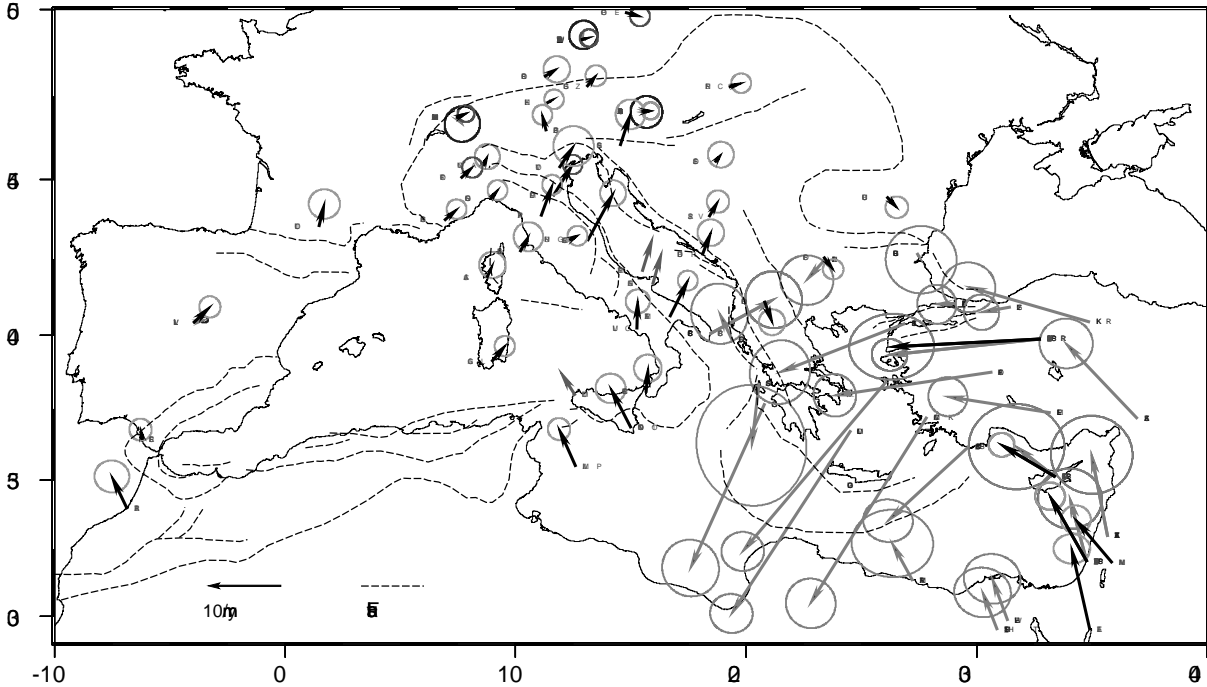


Figure 31.1: GPS horizontal velocities and their 95% confidence ellipses in a Eurasia-fixed reference frame for the period 1999-2002. Black arrows: velocities from this study. Gray arrows: publicly available velocities (McCluski et al., 2000). Dark gray arrows: velocities by E. Serpelloni (INGV, personal communication)

sible correlations between solutions. Monthly combinations of daily solutions, which tests suggest have white-noise characteristics, provide sufficient observations to obtain robust chi-square statistics on the residuals about the linear trends to properly weight the velocities. We compute velocity solutions using the monthly combinations, and scale the formal errors by the square root of chi-square of the solution. We allow a random walk of 1 mm/yr to take into account possible monument instability.

The active deformation in the Adriatic region (Figure 31.1) is highly variable with velocities decreasing from south ( $\sim 5$  mm/yr) to north ( $\sim 2$  mm/yr). Preliminary motion estimates (1999-2002) for stations located on the northern edge of the African plate (RABT, LAMP, NOTO, MATR, HELW and MEST) show a north-westward motion (N  $23 \pm 2$  W) at  $6 \pm 1$  mm/yr. Sites in Corsica (AJAC) and North-western Italy (ELBA, GENO, TORI, NOVA, UNPG) show no significant deformation, while the stations on the Italian peninsula close to the Adriatic sea (VOLT, VENE, CAME, TREM, ANGE, MATE, SPEC) are characterized by a north-eastward motion (N  $29 \pm 3$  E) at  $5 \pm 1$  mm/yr. Stations located on the eastern edge of the Adriatic Sea (GSR1, DUBR, SRJV) move in the same direction (N  $23 \pm 7$  E) at a somewhat slower rate ( $3 \pm 1$  mm/yr). The northward displacement (N  $3 \pm 4$  E at  $3 \pm 1$  mm/yr) of sites in the

southern Italian peninsula (TGRC, VLUC) may reflect a transition between the African plate and the Adriatic region.

### 0.3 Acknowledgements

This work has been partially funded by the Istituto Nazionale di Oceanografia e Geofisica Sperimentale (OGS), Udine, Italy.

### 0.4 References

McCluski et al., Global Positioning Constraints on plate kinematics and dynamics in the eastern Mediterranean and Caucasus, *J. Geophys. Res.*, 105, 5695, 2000.

# Chapter 32

## Global Waveform Tomography with Spectral Element Method

Yann Capdeville, Barbara Romanowicz, Yuang-Cheng Gung

### 0.1 Introduction and Research Objectives

Because seismogram waveforms contain much more information on the earth structure than body wave time arrivals or surface wave phase velocities, inversion of complete time-domain seismograms should allow much better resolution in global tomography. In order to achieve this, accurate methods for the calculation of forward propagation of waves in a 3D earth need to be utilized, which presents theoretical as well as computational challenges.

In the past 8 years, we have developed several global 3D S velocity models based on long period waveform data, and a normal mode asymptotic perturbation formalism (NACT, *Li and Romanowicz, 1996*). While this approach is relatively accessible from the computational point of view, it relies on the assumption of smooth heterogeneity in a single scattering framework. Recently, the introduction of the spectral element method (SEM) has been a major step forward in the computation of seismic waveforms in a global 3D earth with no restrictions on the size of heterogeneities (*Chaljub, 2003*). While this method is computationally heavy when the goal is to compute large numbers of seismograms down to typical body wave periods (1-10 sec), it is much more accessible when restricted to low frequencies ( $T > 150\text{sec}$ ). When coupled with normal modes (e.g. *Capdeville et al., 2000*), the numerical computation can be restricted to a spherical shell within which heterogeneity is considered, further reducing the computational time.

Here, we present a tomographic method based on the non linear least square inversion of time domain seismograms using the coupled method of spectral elements and modal solution. SEM/modes are used for both the forward modeling and to compute partial derivatives. The parameterization of the model is also based on the spec-

tral element mesh, the "cubed sphere", which leads to a 3D local polynomial parameterization. This parameterization, combined with the excellent earth coverage resulting from the full 3D theory used for the forward modeling, leads to a very stable inversion scheme. Synthetic tests show that, with a limited number of events (between 50 and 100), using long period records ( $>150\text{s}$ ) and representative background seismic noise, it is possible to recover both amplitude and phase of the earth model with high accuracy.

### 0.2 Method

Our aim is to find the "best" Earth model that explain our seismic data set. Let assume we wish to solve the inverse problem with a classical least square inversion with a complete modeling theory that is the Spectral Element Method (SEM) applied to the wave equation. Classical inversion processes require to compute the partial derivative matrix

$$\mathbf{A} = \left[ \frac{\partial \mathbf{f}(\mathbf{x})}{\partial \mathbf{x}} \right]_{\mathbf{x}}. \quad (32.1)$$

where  $\mathbf{x}$  the set of parameters which describe the model, and  $\mathbf{f}$  is the "function" that produce a synthetic data set  $\mathbf{d}$  for a given set of model parameters  $\mathbf{x}$ .

In most of the classical tomographic methods, the forward problem is solved using the Born approximation within the normal modes framework which leads to a linear relation between the set of parameters and the synthetic data, and this relation matrix is  $\mathbf{A}$ . Our case is different since there is no way to compute directly the partial derivative matrix or kernel with the SEM but using brute force with a finite differences formula:

$$\left[ \frac{\partial \mathbf{f}(\mathbf{x})}{\partial \mathbf{x}} \right]_{\mathbf{x}=\mathbf{x}_0} \simeq \frac{\mathbf{f}(\mathbf{x}_0 + \delta \mathbf{x}) - \mathbf{f}(\mathbf{x}_0)}{\delta \mathbf{x}}. \quad (32.2)$$

Therefore, in order to compute the partial derivative matrix, one need to compute the whole data set, that is as many runs as the number of sources, for each parameter of the model. This will be obviously the most expensive

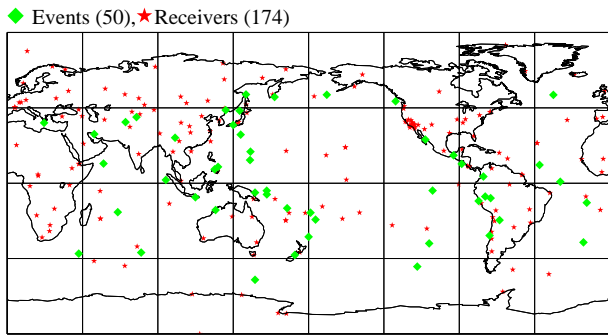


Figure 32.1: Distribution of the sources and stations used in this experiment.

part of the inversion. An estimation of the computing time shows that computing the partial derivative matrix might takes years, even on large computers.

Here we used a scheme that reduce the computation by a factor equal to the number of sources and make the process possible within a reasonable amount of time.

We now show a synthetic inversion to test the scheme. The “data” are produced with the SEM in a known model that we try to retrieve. The source-receiver distribution is shown on Figure 32.1. The parameterization used here to describe the model is based of the spectral element mesh. We use here a mesh roughly equivalent to a degree 8 in spherical harmonics as shown on Figure 32.3 . We show results of the 2 first iterations of the inversion on Figure 32.2. The model is represented in a linear way: the velocity contrast are shown as a function of the parameter number. It is sorted such that the left part is the lower mantle and the right part is the upper mantle. The residual between the wanted model an the obtained model shows an excellent agreement.

A description of the coupled method with illustrations can be found on <http://www.seismo.berkeley.edu/~yann>

### 0.3 Acknowledgements

Most of the computation were made using the computational resources of the NERSC, especially the IBM SP, under repo mp342.

### 0.4 References

Capdeville, Y., B. Romanowicz and A. To (2003). Coupling Spectral Elements and Modes in a spherical earth: an extension to the “sandwich” case. *Geophys. J. Int.* Vol 154, pp 44-57

Chaljub, E. Capdeville, Y. and Vilotte, J.P. (2003) Solving elastodynamics in a solid heterogeneous 3D-sphere: a parallel spectral element approximation on non-conforming grids. *J. Comp Phy.* Vol. 183 pp. 457-

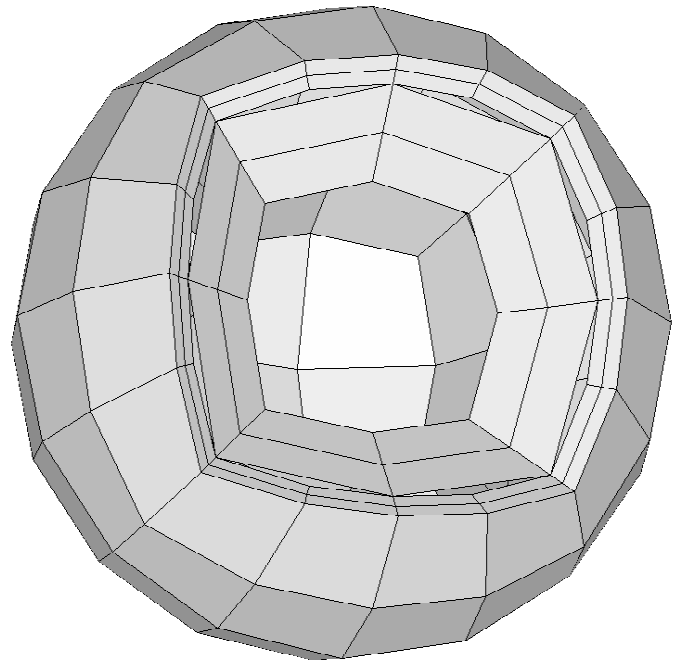


Figure 32.2: Mesh used for the parameterization of the experiment

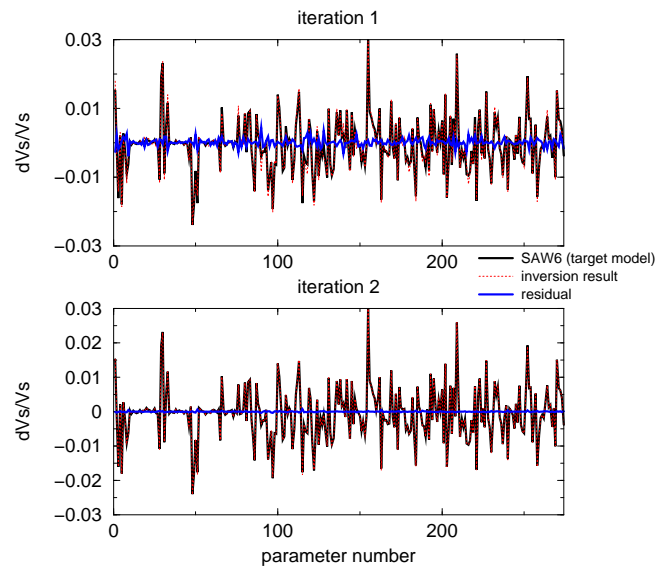


Figure 32.3: Synthetic inversion model results of the two first iterations in a linear representation (see text). The residual between the wanted model an the obtained model shows an excellent agreement

Capdeville Y., E. Chaljub, J.P. Vilotte and J.P. Montagner (2003). Coupling the Spectral Element Method with a modal solution for Elastic Wave Propagation in Global Earth Models. *Geophys. J. Int.*, Vol 152, pp 34–66

Capdeville Y., C. Larmat, J.P. Vilotte and J.P. Montagner (2002) Numerical simulation of the scattering induced by a localized plume-like anomaly using a coupled spectral element and modal solution method. *Geoph. Res. Lett.* VOL. 29, No. 9, 10.1029/2001GL013747

Capdeville Y., E. Stutzmann and J. P. Montagner (2000). Effect of a plume on long period surface waves computed with normal modes coupling. *Phys. Earth Planet. Inter.*, Vol 119 pp. 57–74.

Li, X. B. and Romanowicz, B. (1996) . Global mantle shear velocity model developed using nonlinear asymptotic coupling theory *J. Geophys. Res.* Vol 101, pp 11,245–22,271.

## Chapter 33

# Global Anisotropy and the Thickness of Continents

Yuancheng Gung, Mark Panning and Barbara Romanowicz

### 0.1 Introduction

For decades there has been a vigorous debate about the depth extent of continental roots (*Jordan, 1975*) The analysis of heat flow (*Jaupart et al., 1998*), mantle xenoliths (*Rudnick et al., 1998*) and electrical conductivity (*Hirth, 2000*) indicate that the coherent, conductive part of continental roots is not much thicker than 200-250 km. Some global seismic tomographic models agree with this estimate but others indicate much thicker zone of fast velocities under continental shields, reaching at least 400km in depth. This is manifested by a drop in correlation between some models from  $\sim 0.80$  at 100km to less than 0.45 at 300 km depth (Figure 33.1a), which casts some doubt on the ability of global tomography to accurately resolve upper mantle structure.

However, although global  $V_S$  models differ from each other significantly in the depth range 200-400km under the main continental shields, these differences are consistent when they are classified into three categories, depending on the type of data used to derive them: *SV* (mostly vertical or longitudinal component data, dominated by Rayleigh waves in the upper mantle), *SH* (mostly transverse component data, dominated by Love waves), and (3)*hybrid* (three component data). *SH* and *hybrid* models are better correlated with each other than with *SV* models. This difference is accentuated when the correlation is computed only across continental areas, as shown in Figure 33.1b. The reduced correlation in the depth range 250-400 km between *SH* and *hybrid* models and *SV* models is strongly accentuated over continents.

On the other hand, global tomographic studies that account for seismic anisotropy, either by inverting three component data for  $V_{SV}$  and  $V_{SH}$  using isotropic kernels (*Ekström and Dziewonski, 1998*), or in the framework of more general anisotropic theory (*Montagner and Tani-moto, 1991*), have documented significant lateral varia-

tions in the anisotropic parameter  $\xi (= (V_{SH}/V_{SV})^2)$  on the global scale. Until now, attention has mostly focused on the strong positive  $\delta \ln \xi (= 2(\delta \ln V_{SH} - \delta \ln V_{SV}))$  observed in the central part of the Pacific Ocean in the depth range 80-200 km. The presence of this anisotropy has been related to shear flow in the asthenosphere, with a significant horizontal component. Deeper anisotropy was suggested, but not well resolved in these studies, either because the dataset was limited to fundamental mode surface waves, or because of the use of inaccurate depth sensitivity kernels. In particular, it is important to verify that any differences in  $V_{SV}$  and  $V_{SH}$  observed below 200km depth are not an artifact of simplified theoretical assumptions, which ignore the influence of radial anisotropy on depth sensitivity kernels.

### 0.2 Results

We have developed an inversion procedure for transverse isotropy using three component surface and body waveform data, in the framework of normal mode asymptotic coupling theory (*Li and Romanowicz, 1995*), which in particular, involves the use of 2D broadband anisotropic sensitivity kernels appropriate for higher modes and body waves.

Figure 33.2 shows the distributions of  $\delta \ln \xi$  in the resulting degree 16 anisotropic model *SAW16AN*. At 175 km depth, the global distribution of  $\delta \ln \xi$  confirms features found in previous studies, and is dominated by the striking positive  $\delta \ln \xi > 0$  ( $V_{SH} > V_{SV}$ ) anomaly in the central Pacific and a similar one in the Indian Ocean. However, at depths greater than 250 km, the character of the distribution changes: positive  $\delta \ln \xi$  emerges under the Canadian Shield, Siberian Platform, Baltic Shield, southern Africa, Amazonian and Australian cratons, while the positive  $\delta \ln \xi$  fades out under the Pacific and Indian oceans. At 300 km depth, the roots of most cratons are characterized by positive  $\delta \ln \xi$ , which extend down to about 400 km. These features are emphasized in depth cross sections across major continental shields (Figure 33.3), where we compare  $V_{SH}$  and  $V_{SV}$  distri-

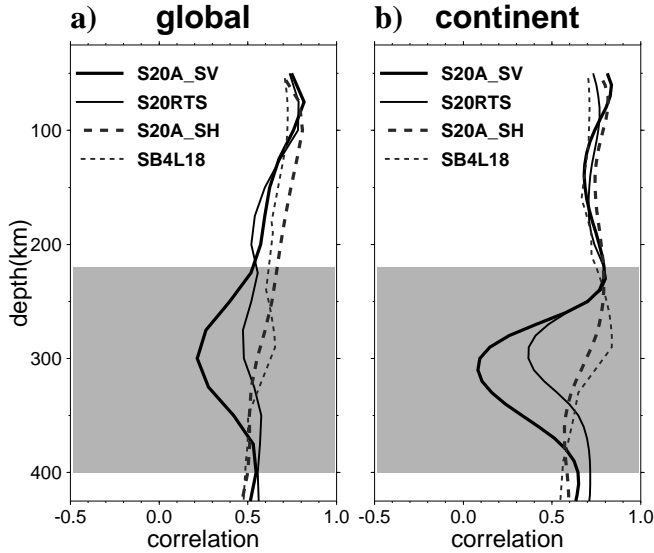


Figure 33.1: Correlation coefficient as a function of depth between model *SAW24B16* (Mégnin and Romanowicz, 1999), an *SH* model, and other global tomographic *S* velocity models. (a) over the whole globe; (b) over continental areas only. *S20ASH* (Ekström and Dziewonski, 1998) is an *SH* model, *SB 4L18* (Masters et al., 1996) is a hybrid model and *S20ASV* (Ekström and Dziewonski, 1998) and *S20RTS* (Ritsema et al., 1999) are both *SV* models.

butions, consistently showing deeper continental roots in  $V_{SH}$ . Interestingly, the East Pacific Rise has a signature with  $\delta \ln \xi < 0$  down to 300km, indicative of a significant component of vertical flow. At 400km depth, we also note the negative  $\delta \ln \xi$  around the Pacific ring, consistent with quasi-vertical flow in the subduction zone regions in the western Pacific and south America.

### 0.3 Discussions

Temperatures in the 250-400 km depth range exceed  $1000^\circ\text{C}$ , and are therefore too high to allow sustained frozen anisotropy in a mechanically coherent lithospheric lid on geologically relevant time scales (Vinnik et al., 1992). Therefore we infer that the  $V_{SH} > V_{SV}$  anisotropy under continental roots we describe here must be related to present day flow-induced shear, with a significant horizontal component.

We note the similarity of the character of  $V_{SH} > V_{SV}$  anisotropy, in the depth range 200-400km under cratons, and 80-200km under ocean basins, and we suggest that both are related to shear in the asthenosphere, the difference in depth simply reflecting the varying depth of the asthenospheric channel. Although our inference is indirect, it reconciles tomographic studies with other geophysical observations of lithospheric thickness based on

heat flow, xenoliths and mantle electrical conductivity.

Another contentious issue is the nature of the Lehmann discontinuity ( $L$ ), and in particular the puzzling observation that it is not a consistent global feature, but is observed primarily in stable continental areas and not under oceans (Gu et al., 2001). Since the  $V_{SH} > V_{SV}$  anisotropy under continental cratons is found deeper than 200 km, we propose that  $L$  actually marks the top of the asthenospheric layer, a transition from weak anisotropic lowermost continental lithosphere to anisotropic asthenosphere. Under oceans, the lithosphere is much thinner, and the lithosphere/asthenosphere boundary occurs at much shallower depths. There is no consistently observed discontinuity around 200-250 km depth. On the other hand, a shallower discontinuity, the Gutenberg discontinuity ( $G$ ), is often reported under oceans and appears as a negative impedance reflector (Revenaugh and Jordan, 1991). The difference in depth of the observed  $\delta \ln \xi > 0$  anisotropy between continents and oceans is consistent with an interpretation of  $L$  and  $G$  as both marking the bottom of the mechanically coherent lithosphere, in areas where it is quasi-horizontal (Figure 33.4).

### 0.4 Conclusion

Thus, the inspection of radial anisotropy in the depth range 200-400 km allows us to infer that continental roots do not extend much beyond 250km depth, in agreement with other geophysical observations. The part of the mantle under old continents that translates coherently with plate motions need not be thicker than 200-250km. Tomographic models reveal the varying depth of the top of the anisotropic asthenospheric channel, marked by a detectable seismic discontinuity called  $L$  under continents (about 200-250km depth), and  $G$  under oceans (about 60-80km depth). Finally, seemingly incompatible tomographic models obtained by different researchers can thus also be reconciled: the relatively poor correlation between different models in the depth range 250-400 km is not due to a lack of resolution of the tomographic approach, but rather to the different sensitivity to anisotropy of different types of data.

### 0.5 Acknowledgements

We thank the National Science Foundation for support of this research.

### 0.6 References

- Ekström, G., and A.M. Dziewonski, The unique anisotropy of the Pacific upper mantle, *Nature*, 394, 168-171, 1998.
- Gu, Y., A.M. Dziewonski, W.-j. Su, and G. Ekström, Models of the mantle shear velocity and discontinuities in

the pattern of lateral heterogeneities, *J. Geophys. Res.*, *106*, 11,169-11,200, 2001.

Gung, Y., M. Panning and B. Romanowicz, Global anisotropy and the thickness of continents, *Nature*, *422*, 707-711 2003.

Jordan, T.H., The continental lithosphere, *Rev. Geoph. Space Phys.*, *13*, 1-12, 1975.

Hirth, G., Evans, R.L. and Chave A. D. Comparison of continental and oceanic mantle electrical conductivity: Is the Archean lithosphere dry?, *Geochem. Geophys. Geosyst.*, *1*, 2000GC000048, 2000.

Jaupart, C., Mareschal, J.C. and Guillou-Frottier, L., Heat flow and thickness of the lithosphere in the Canadian Shield, *J. Geophys. Res.*, *103*, 15,269-15,286, 1998.

Li, X.-D. and B. Romanowicz, Comparison of global waveform inversions with and without considering cross-branch modal coupling, *Geophys. J. Int.*, *121*, 695-709, 1995.

Masters, G., S. Johnson, G. Laske, and H. Bolton, A shear-velocity model of the mantle, *Phil. Trans. R. Soc. London*, *354* 1,385-1,410, 1996.

Mégnin, C., and B. Romanowicz, The 3D shear velocity structure of the mantle from the inversion of body, surface and higher mode waveforms, *Geophys. J. Int.*, *143*, 709-728, 2000.

Montagner, J.P., and T. Tanimoto, Global upper mantle tomography of seismic velocities and anisotropies, *J. Geophys. Res.*, *96*, 20,337-20,351, 1991.

Revenaugh, J. and Jordan, T.H., Mantle layering from ScS reverberations, 3. The upper mantle, *J. Geophys. Res.*, *96*, 19781-19810, 1991.

Ritsema, J., van Heijst, H. and Woodhouse, J. H., Complex shear wave velocity structure imaged beneath Africa and Iceland, *Science*, *286*, 1925-1928, 1999.

Rudnick, R., McDonough, W. and O'Connell, R. Thermal structure, thickness and composition of continental lithosphere, *Chem. Geol.*, *145*, 395-411, 1998.

Vinnik, L.P., Makeyeva, L.I., Milev, A. and Usenko, Y., Global patterns of azimuthal anisotropy and deformations in the continental mantle, *Geophys. J. Int.*, *111*, 433-447, 1992.

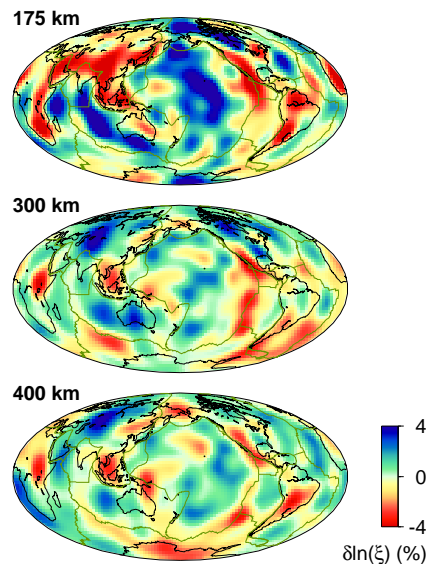


Figure 33.2: Maps of relative lateral variations in  $\xi$  of model *SAW16AN* at 3 depths in the upper mantle. Lateral variations are referred to reference model *PREM*, which is isotropic below 220km depth, but has significant  $\delta \ln \xi > 0$  at 175km depth.

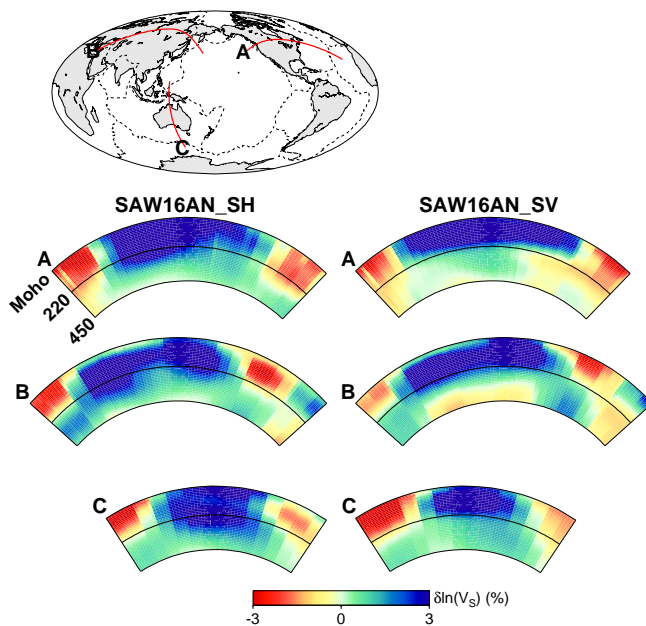


Figure 33.3: Depths cross-sections through 3 continents showing the *SH* (left) and *SV* (right) components of anisotropic model *SAW16AN*. The *SH* sections consistently indicate fast velocities extending to depths in excess of 220 km, whereas the *SV* sections do not.

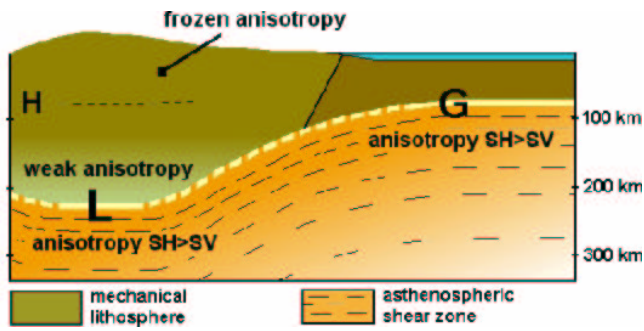


Figure 33.4: Sketch illustrating our interpretation of the observed anisotropy in relation to lithospheric thickness, and its relationship to Lehmann ( $L$ ) and Gutenberg ( $G$ ) discontinuities. The Hales discontinuity ( $H$ ) is also shown.  $H$  is generally observed as a positive impedance embedded within the continental lithosphere in the depth range 60-80km.  $H$  and  $G$  may not be related.

# Chapter 34

## Large Scale Anisotropy Near the Core-Mantle Boundary from Global Waveform Inversion

Mark Panning and Barbara Romanowicz

### 0.1 Introduction

The Earth's core-mantle boundary (CMB) is both a thermal and chemical boundary layer between the solid silicate mantle and the fluid iron outer core. The mantle-side portion of this layer ( $D''$ ), is therefore the site of dynamic processes that may involve both thermal and chemical heterogeneity at various scales. Additionally, this area also functions as a mechanical boundary layer for the convection of the overlying mantle, leading to intense deformation. This deformation can lead to detectable seismic anisotropy, either through the alignment of anisotropic crystals in the strain field or through the alignment of layering or inclusions of materials with strongly contrasting elastic properties (Karato, 1998; Kendall and Silver, 1996).

Anisotropy in  $D''$  has been well established in several regions, including under the Pacific, northern Asia, Alaska, and central America, from the observation of S waves diffracting ( $S_{diff}$ ) or reflecting ( $S_{cS}$ ) at the CMB (Vinnik *et al.*, 1989; Kendall and Silver, 1996; Lay *et al.*, 1998). However, these studies only sample limited areas of  $D''$ , and therefore interpretation is difficult. A more global picture of long-wavelength anisotropic  $D''$  structure would clearly aid interpretation both in terms of dynamic flow modeling as well as mineral physics.

With this in mind we have adapted our global waveform tomography approach (Méglin and Romanowicz, 2000) to develop a 3D model of radial anisotropy throughout the mantle using a large dataset of three component time-domain waveforms of both surface and body waves.

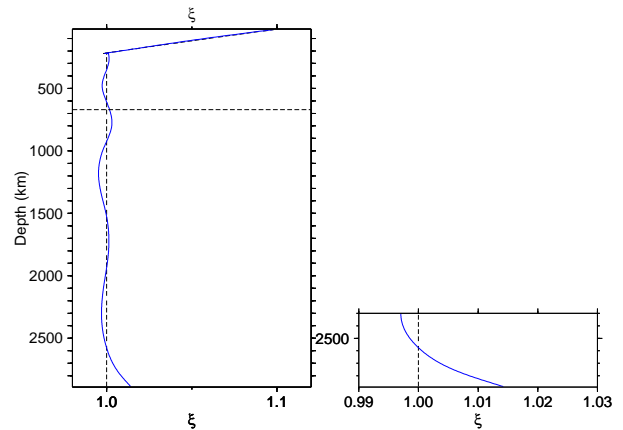


Figure 34.1: Radially symmetric values of  $\xi$  as a function of depth in the model. The values for PREM, the starting model, are shown by the dashed line, and the 670 discontinuity is shown by the dotted line. Notice the strong increase at the base of the mantle, similar but smaller in magnitude to that seen in the upper mantle.

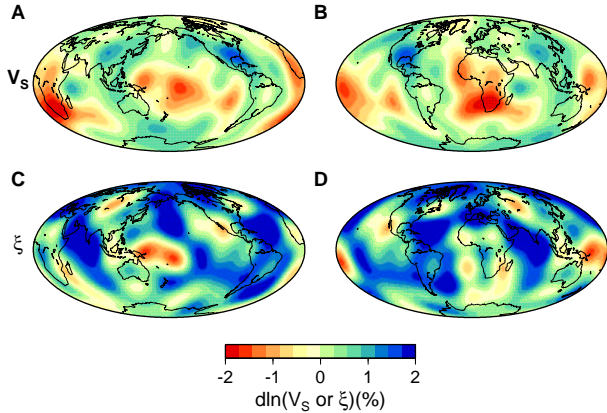


Figure 34.2:  $\delta \ln V_S$  (A and B) and  $\delta \ln \xi$  (C and D) shown at a depth of 2800 km. Slices are shown centered under the Pacific (A and C) and Africa (B and D).

## 0.2 D'' Anisotropic Model

The model is parameterized in terms of isotropic  $V_S$  and the anisotropic  $\xi$  parameter ( $\xi = V_{SH}^2/V_{SV}^2$ ), which is directly related to radial anisotropy in shear velocity. In our model, D'' is characterized by a strong radially symmetric signature of radial anisotropy, as seen in the uppermost mantle in previous anisotropic models such as PREM (*Dziewonski and Anderson, 1981*). Similar to the uppermost 200 km of the mantle, this signature is a positive  $\delta \ln \xi$ , indicating that horizontally polarized shear velocity,  $V_{SH}$ , is faster than vertically polarized shear velocity,  $V_{SV}$  (Figure 34.1).

The 3D isotropic velocity imaged in D'' in this study is consistent with earlier tomographic models of shear velocity in this depth range (*Masters et al., 1996; Mégnin and Romanowicz, 2000*), and is characterized by a strong degree 2 component representing a fast ring surrounding two low velocity features (often called superplumes) centered beneath the central Pacific and Africa (Figure 34.2, A and B). In the  $\xi$  model, the strong degree 0 component appears to be limited to the lowermost 300 km (Figure 34.1, inset), but the regions that differ most from this average structure correlate well with the locations of the superplumes, with reduced values of  $\delta \ln \xi$  under the central Pacific, Africa, and the south Atlantic, including patches with negative values ( $V_{SV} > V_{SH}$ ).

The long-wavelength anisotropic features imaged in our model generally agree with more localized studies of D'' anisotropy. Specifically, these studies imaged areas with positive  $\delta \ln \xi$  beneath central America and Alaska. The central Pacific appears to be more variable with some areas showing negative  $\delta \ln \xi$  (*Lay et al., 1998*).

## 0.3 Conclusions

Our study extends to a global scale the results obtained so far for limited regional sampling of D''. The dominant  $V_{SH} > V_{SV}$  found as one approaches the CMB suggests that the anisotropy observed in D'' is related to the dominant horizontal flow in a mechanical boundary layer, analogous to the larger signal observed in the uppermost 200 km of the mantle. As one approaches regions of upwelling, the direction of flow changes and results in a different signature of anisotropy, as manifested in our study under the central Pacific and Africa. In reality, anisotropy in these regions bordering the large scale upwellings may be much more complex and include tilting of the vertical axis of symmetry assumed in our modeling. This could lead to azimuthal anisotropy which we do not yet attempt to model.

Although our model does not determine the microscopic causes of the observed anisotropy, the results clearly suggest that the dynamics of D'' correspond with what would be expected in a boundary layer dominated by horizontal flow, and emphasize the unique character of the two superplume regions. Although mineral physics data are not yet available for the pressure and temperature conditions at the base of the mantle, our results suggest that similar relationships between anisotropic signature and flow prevail in the uppermost and lowermost mantle.

## 0.4 References

- Dziewonski, A.M., and D.L. Anderson, Preliminary reference Earth model, *Phys. Earth Planet. Int.*, 25, 297-356, 1981.
- Karato, S.-I., Some remarks on the origin of seismic anisotropy in the D'' layer *Earth, Planets, Space*, 50, 1019-1028, 1998.
- Kendall, J.-M. and P.G. Silver, Constraints from seismic anisotropy on the nature of the lowermost mantle, *Nature*, 381, 409-412, 1996.
- Lay, T., Q. Williams, E.J. Garnero, L. Kellogg, and M. Wyession, Seismic wave anisotropy in the D'' region and its implications, in *The core-mantle boundary region*, M. Gurnis, M.E. Wyession, E. Knittle, B.A. Buffett, Eds., Amer. Geophys. Union, pp. 219-318, 1998.
- Masters, G., H. Bolton, and G. Laske, Joint seismic tomography for P and S velocities: How pervasive are chemical anomalies in the mantle? *EOS Trans. AGU*, 80 S14, 1999.
- Mégnin, C., and B. Romanowicz, The 3D shear velocity of the mantle from the inversion of body, surface, and higher mode waveforms, *Geophys. Jour. Intl.*, 143, 709-728, 2000.
- Vinnik, L., V. Farra, and B. Romanowicz, Observational evidence for diffracted SV in the shadow of the Earth's core, *Geophys. Res. Lett.*, 16, 519-522, 1989.

## Chapter 35

# Towards Forward Modeling of 3D Heterogeneity in D'' region

Akiko To, Yann Capdeville and Barbara Romanowicz

### 0.1 Introduction

The presence of strong lateral heterogeneity in D'' is now well documented, and represents a problem for seismic modeling, when using standard ray or mode approaches, because of the theoretical limits of validity of these methods. Consequently, present tomographic models are only able to represent the large scale, smooth features of the structure. They may also not reflect the amplitudes of lateral variations accurately. We use a coupled normal mode/Spectral Element Method (SEM) (Capdeville *et al.*, 2003) to compute synthetic seismograms of Sdiff in the D'' part of a 3D tomographic model (SAW24B16, Mégnin and Romanowicz, 2000) down to a corner frequency of 1/12s. This coupled method is much faster than standard SEM, as the numerical part of the computation is restricted to the D'' region. The rest of the mantle is assumed 1D, and there the wavefield is computed using efficient normal mode summation.

### 0.2 Comparison between Observed and Synthetic Waveforms

We compare the synthetics thus obtained with observed waveforms for a collection of 16 deep earthquakes in the Western Pacific. The results from one of the events are shown in Figure 35.1 and Figure 35.2. For deep earthquakes, the effect of strong heterogeneity in the crust and upper mantle is avoided. Observed and synthetic travel time trends are very consistent, although in most cases the observed residuals are significantly larger. Waveform amplitudes are less consistent.

We manually modify the original SAW24b16, and by trial and error try to make a better model which fit the observations (Figure 35.3). The fit becomes better in a few traces, but in many cases it is difficult to fit both amplitude and travel times (Figure 35.4).

### 0.3 Modification of the Velocity Model by a Genetic Algorithm

We try to apply a genetic algorithm to travel time or waveform modeling in the D''. The advantages of GAs are that there is no damping and the output models are less controlled by the starting model. These properties are appropriate for modeling strong and complex heterogeneity in the D''. The defect of the method is the high computational cost. By limiting the target to a small local region on the CMB, we reduce the number of model parameters. We use ray theory, which is the most expedient method, to calculate travel times, and examine whether a GA is useful for modeling D''.

We choose a region of 28 x 28 degree in Northern Pacific, where 58 Sdiff ray paths diffract on CMB. We divided the region to 25 boxes. The number of initial ensemble of models is 30. After 15 to 16 generations, the model converged. We were able to get 35% of variance reduction. In future, we want to apply this method using NACT with the focusing and defocusing effect.

### 0.4 Comparison of Travel Time between Ray Theory and Coupled Mode/SEM

We compared the predicted Sdiff travel time between ray theory and Coupled Mode/SEM (Figure 35.5). Ray theory is a most expedient way to calculate travel times. However, it is an infinite frequency approximation and not appropriate to handle diffracting waves.

For negative residuals, both residuals are almost the same. They distribute around  $y=x$  with in 1 to 2 second differences. However, for positive residuals, the predictions from ray theory give larger values by up to 4 seconds. This is consistent with theoretical predictions for the wave front healing effect (e.g. Nolet and Dahlen, 2000).

## 0.5 Acknowledgements

We thank the National Science Foundation for support of this research.

## 0.6 References

Capdeville Y., B. Romanowicz and A. To, Coupling Spectral Elements and Modes in a spherical earth: an extension to the “sandwich” case. *Geophys. J. Int.*, 154, 44-57, 2003

Capdeville Y., E. Chaljub, J.P. Vilotte and J.P. Montagner, Coupling the Spectral Element Method with a modal solution for Elastic Wave Propagation in Global Earth Models, *Geophys. J. Int.*, 153, 34-66, 2003

Dziewonski A.M., and D.L. Anderson, Preliminary reference Earth model, *Phys. Earth Planet. Inter.*, 25, 297-356, 1981.

Mégnin, C., and B. Romanowicz, The shear velocity structure of the mantle from the inversion of of body, surface and higher modes waveforms, *Geophys. J. Int.*, 143, 709-728, 2000

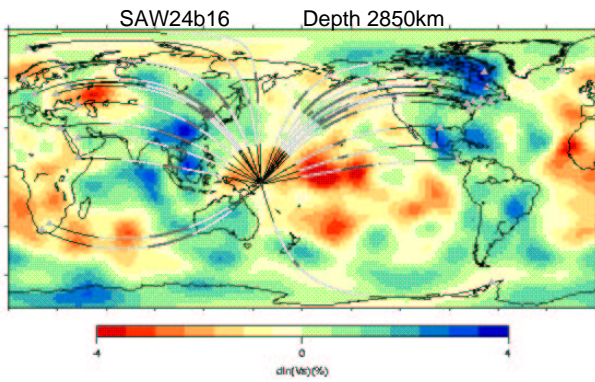


Figure 35.1: The ray paths distribution of Sdiff phase whose waveforms are shown in Figure 35.2. The event is 511.2km deep. Dark gray line: the diffracting part. Light gray line: The ray paths at the bottom 370km of the mantle, where 3D heterogeneity is included in synthetic waveform calculation.

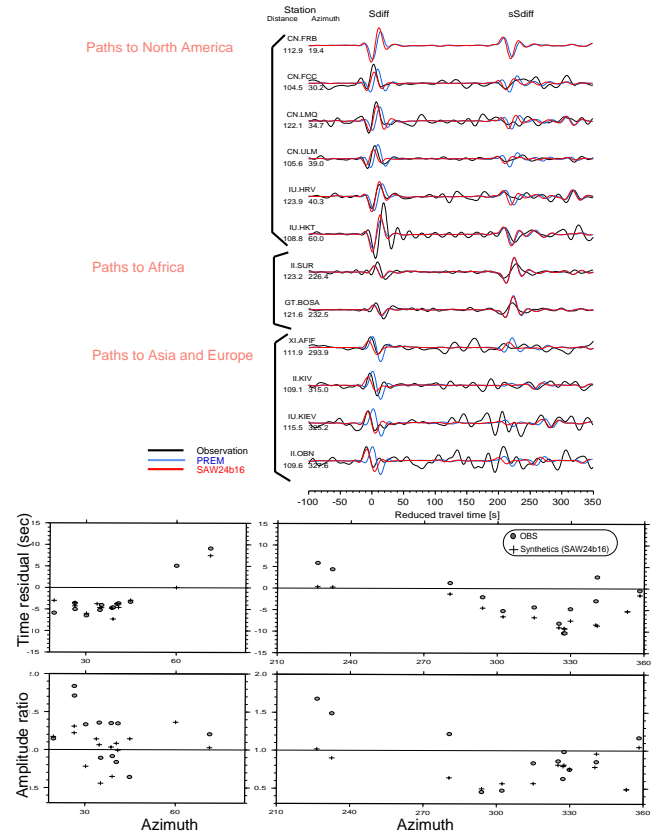


Figure 35.2: Top: Comparison of selected waveforms. Synthetic waveforms are made by couple model/SEM 3D models of the D” layer. The contribution of heterogeneity from rest of the mantle is calculated by ray theory. Bottom: Travel time residuals and maximum amplitude ratio relative to PREM (*Dziewonski and Anderson, 1981*) for all traces.

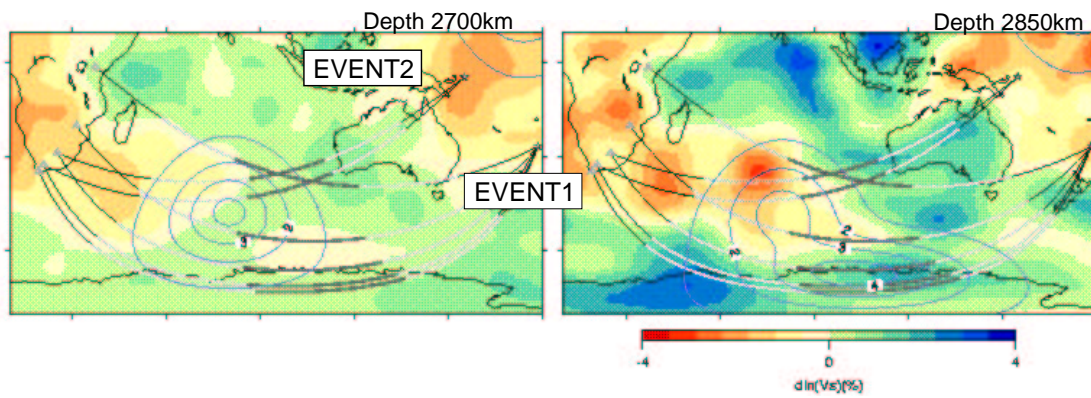


Figure 35.3: The background model is SAW24b16. The blue line shows the region where the anomaly is amplified in each depth. Numbers on the blue line show the factor of amplification. The waveforms calculated from this model is shown in Figure 35.4

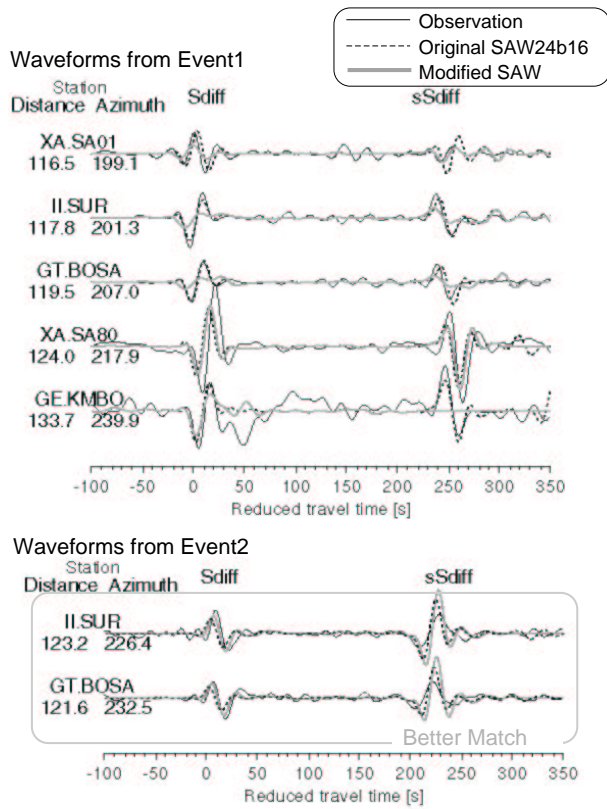


Figure 35.4: Waveforms from modified model as indicated in Figure 35.3. The two waveforms from Event2 show better fit between synthetics from the modified model and the observations. However, the fit between observation and synthetics become worse in the modified model for most of the waveforms from Event1.

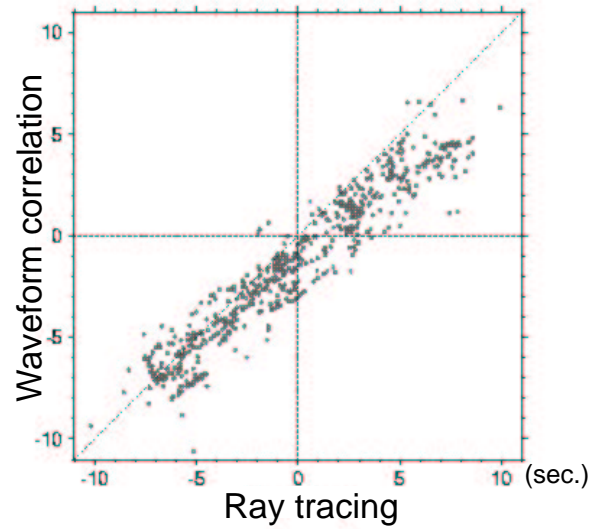


Figure 35.5: Synthetic travel time residuals with respect to PREM for 800 globally distributed Sdiff phase. The 3D velocity model used in the comparison is SAW24b16. The model has 3D heterogeneity in the bottom 370km of the mantle. The travel time residuals calculated using Coupled Mode/SEM are on Y axis. We cross correlated the waveforms constructed from the 3D model and PREM.

## Chapter 36

# Constraints on Density and Shear Velocity Contrasts at Inner Core Boundary

Aimin Cao and Barbara Romanowicz

### 0.1 Introduction

Density and shear velocity contrasts at the Inner Core Boundary (ICB) likely play a significant role in the character of the Earth's geodynamo and the evolution of the inner core. While studies of geodynamo have been made remarkable progress in the past decades (e.g., *Hewitt et al.*, 1975; *Backus*, 1975; *Gubbins*, 1977; *Loper*, 1978; *Mollett*, 1984; *Buffet et al.*, 1996; *Labrosse et al.*, 1997; *Stacey and Stacey*, 1999), the density and shear velocity contrasts at ICB are still controversial issues.

So far there are basically three distinct ways to constrain the density and shear velocity contrasts at the ICB. The first one is using the normal modes which are sensitive to the inner core structure (*Gilbert et al.*, 1973; *Gilbert and Dziewonski*, 1975; *Masters*, 1979). This technique suggested a density jump of 0.5-0.6  $gcm^{-3}$  and a shear velocity jump of 3.45  $kms^{-1}$  at the ICB.

The second one is using the body wave amplitude and waveform modeling of PKP and PKiKP. This technique suggested a density jump of 0-1.2  $gcm^{-3}$  (*Hage*, 1983) and shear velocity jumps of 2.5-3.0  $kms^{-1}$  (*Hage*, 1983), 2-4  $kms^{-1}$  (*Cummins and Johnson*, 1988) at the ICB.

The third one is using body wave amplitude ratio of PKiKP to PcP. *Bolt and Qamar* (1970) first demonstrated this technique and estimated a maximum density jump of 1.8  $gcm^{-3}$  at the ICB. *Souriau and Souriau* (1989) further constrained the density jump in the range of 1.35-1.6  $gcm^{-3}$ . The latest estimation using this method was conducted by *Shearer and Masters* (1990) who suggested the density jump to be less than 1.0  $gcm^{-3}$  and shear velocity jump to be greater than 2.5  $kms^{-1}$  at the ICB.

Compared with the results derived from normal modes,

the constraint on the density contrast from body waves is much more rough and scattered. Therefore, right now the simulations of geodynamo usually refer to the density contrast derived from normal modes.

Nevertheless, a recent geodynamo study (*Stacey and Stacey*, 1999) explicitly pointed out that the inner core would not have existed 2 billion years ago if based on the density contrast at the ICB in the current Earth models. This is obviously against the paleomagnetic evidence, which shows that the Earth has sustained a magnetic field for at least 3 billion years (*McElhinny and Senanayake*, 1980). And the magnetic field is induced by the geodynamo that is powered by energy mainly associated with the cooling and gradual solidification of the core (*Gubbins*, 1977; *Loper*, 1978, 1991; *Gubbins et al.*, 1979). Fortunately this conflict can be readily settled if the density contrast at the ICB is somewhat higher than the assumed value in the seismic inner core models, because the energies of the geodynamo are proportional to the assumed density contrast (*Stacey and Stacey*, 1999). In this study, we try to constrain the density and shear velocity contrasts at the ICB by means of body wave PKiKP/PcP amplitude ratio taking advantage of the availability of recent high quality broadband data.

### 0.2 Data, Method, and Results

We systematically downloaded all of the broadband vertical component data in the epicentral distance range between 10° and 70°, from 1990 to 1999, stored in IRIS Data Management Center (DMC). Before searching for PKiKP and PcP arrivals, the event original time and hypocentral parameters were modified with the relocated earthquake catalog (*Engdahl et al.*, 1998) at first, and then theoretical arrivals (PcP, PKiKP, P, pP, PP, PPP, S, SS, and ScS) were labeled with reference to ak135 model (*Kennett et al.*, 1995) after the corrections for ellipticity. The additional 7 theoretical arrivals are the most

potential interfering sources for PcP and PKiKP phases. Then the seismograms were filtered in band pass 0.7-3 Hz (PKiKP phase is typically with 1 Hz frequency).

The picking quality is classified into three categories A, A-, and B. Quality A means there are very clear PKiKP and PcP phases within 5 seconds of their theoretical arrivals, there is no other theoretical arrival 20 seconds preceding the identified PKiKP or PcP phases (unless the potential interfering arrival can be verified from nodal plane), and the average peak-to-peak signal-to-noise ratio is less than 40%. Quality A- means there are clear PKiKP and PcP phase within 5 seconds of their theoretical arrivals, there is no other theoretical arrival 20 seconds preceding the identified PKiKP or PcP, and the average peak-to-peak signal-to-noise ratio is larger than 40%. Quality B means there is no observable PKiKP phase within 5 seconds of its theoretical arrival, but there is also no any other theoretical arrival 50 seconds preceding the theoretical PKiKP arrival, and PcP phase is very clear within 5 seconds of its theoretical arrival.

Based on above criteria, we collected 5, 16, and 62 Quality A, A-, and B data, respectively. One of the Quality A data is shown in Figure 36.1. The final measurements of PKiKP/PcP ratios were conducted directly with the peak-to-peak amplitudes of the identified PKiKP and PcP phases for Quality A and Quality A- data. For Quality B data, the maximum peak-to-peak amplitude 5 seconds around PKiKP theoretical arrival was read as the upper limit of the PKiKP amplitude (Figure 36.2).

### 0.3 Acknowledgements

We are grateful to the IRIS Data Management Center (DMC) and the network or station operators who contributed data to the DMC.

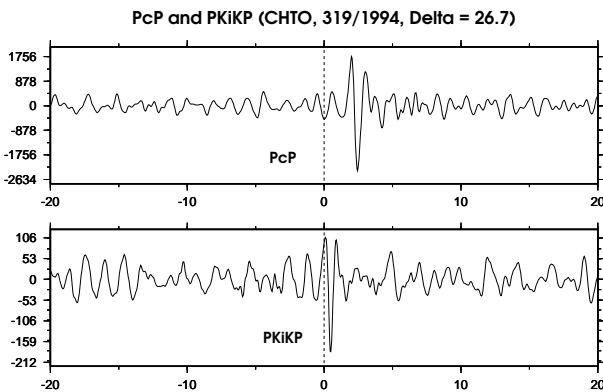


Figure 36.1: A Quality A example with very clear PKiKP and PcP phases. Dashed lines are the theoretical arrivals. The PKiKP/PcP ratio is 0.071.

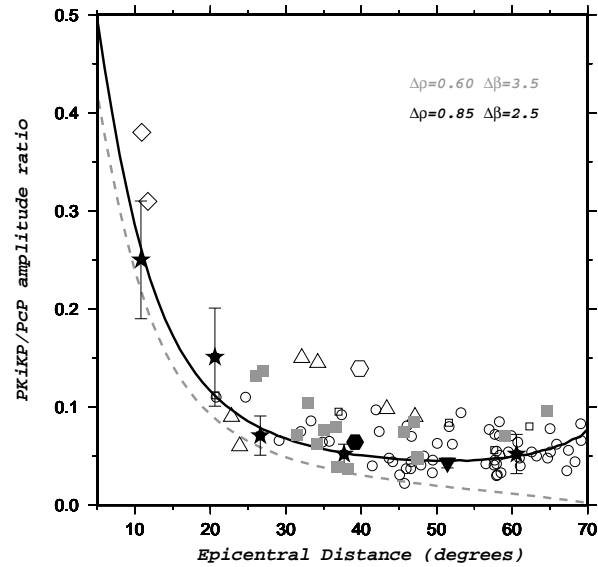


Figure 36.2: Measurements of PKiKP/PcP ratios. The stars denote the Quality A data; the grey squares denote the Quality A- data; and the open dots are the Quality B data. The curves are the theoretical functions of PKiKP/PcP with respect to PREM. Other open symbols are data from previous studies. Our current estimates favor a somewhat larger density jump at the ICB than for PREM

## 0.4 References

Backus, G.E., Gross thermodynamics of heat engines in deep interior of Earth, *Nat. Acad. Sci. USA*, *72*, 1555-1558, 1975.

Bolt, B.A., and A. Qamar, Upper bound to the density jump at the boundary of the Earth's inner core, *Nature*, *228*, 148-150, 1970.

Buffet, B.A., H.E. Huppert, J.R. Lister, and A.W. Woods, On the thermal evolution of the Earth's core, *J. Geophys. Res.*, *101*, 7989-8006, 1996.

Cummins, P., and L.R. Johnson, Short-period body wave constraints of properties of the Earth's inner core boundary, *J. Geophys. Res.*, *93*, 9058-9074, 1988.

Gilbert, F., A.M. Dziewonski, and J.N. Brune, An informative solution to a seismological inverse problem, *Proc. Natl. Acad. Sci.*, *70*, 1410-1413, 1973.

Gilbert, F., and A.M. Dziewonski, An application of normal mode theory to the retrieval of structural parameters and source mechanisms from seismic spectra. *Phil. Trans. R. Soc. Lond.*, *A278*, 187-269, 1975.

Gubbins, D., Energetics of the Earth's core, *J. Geophys.*, *43*, 453-464, 1977.

Hage, H., Velocity constraints for the inner core inferred from long-period PKP amplitudes, *Phys. Earth Planet. Inter.*, *31*, 171-185, 1983.

Hewitt, J.M., D.P. McKenzie, and N.O. Weiss, Dissipative heating in convective flows, *J. Fluid Mech.*, *68*, 721-738, 1975.

Labrosse, S., J.P. Poirier, and J.L. LeMouel, On cooling of the Earth's core, *Phys. Earth Planet. Int.*, *99*, 1-17, 1997.

Loper, D.E., The gravitationally powered dynamo, *Geophys. J. R. Astron. Soc.*, *54*, 389-404, 1978.

Masters, G., Observational constraints on the chemical and thermal structure of the earth's deep interior. *Geophys. J. R. Astron. Soc.*, *57*, 507-534, 1979.

Mollett, S., Thermal and magnetic constraints on the cooling of the Earth, *Geophys. J. R. Astron. Soc.*, *76*, 653-666, 1984.

Souriau, A., and M. Souriau, Ellipticity and density at the inner core boundary from sub-critical PKiKP and PcP data, *Geophys. J. Int.*, *98*, 39-54, 1989.

Stacey, F.D., and C.H.B. Stacey, Gravitational energy of core evolution: implications for thermal history and geodynamo power, *Phys. Earth Planet. Int.*, *110*, 83-93, 1999.

## Chapter 37

# Investigating Mantle's Density Resolution Using the Neighborhood Algorithm

Sébastien Rousset and Barbara Romanowicz

### 0.1 Introduction

Unlike travel times or waveform data, normal mode data are directly sensitive to density. However, the sensitivity kernels for density are much smaller than those for velocities, so the controversy about the possibility of resolution of the mantle's density is still vivid, especially since the publication of model SPRD6 (*Ishii and Tromp, 1999*). Several authors (*Resovsky and Ritzwoller, 1999, Romanowicz, 2001, Kuo and Romanowicz, 2002*) objected that density cannot yet be constrained and the controversy is still going.

However the inversion processes used by previous studies all rely on least-square inversions and require the use of a starting model, the choice of which is critical for the reliability of the results. Unlike this simple inversion scheme whose result is one "best" model, stochastic methods sample the parameter space, and their result is a set of models whose statistical properties reflect the likelihood function. In this study, in order to investigate the resolution, we use the Neighborhood Algorithm (*Sambridge 1999a,b*). The first step of the algorithm generates a set of models that samples the parameter space preferentially where the fit is better. The second step approximates the posterior probability density (ppd) in the parameter space using the previously generated set and quantitative information is extracted from this approximate ppd by a Bayesian approach.

### 0.2 Data Set and Parameterization

Our data set consists in a set of splitting coefficients (*Giardini and al., 1988*) inverted from normal mode spectra. These coefficients are linearly related to the aspheri-

cal structure of the Earth considered as a perturbation  $\delta x$  of the elastic parameter  $x$  of our reference model PREM, integrated over depth:

$$C_{st} = \int_0^a \left(\frac{\delta x}{x}\right)_{s,t}(z) K_s^x(z) dz \quad (37.1)$$

where  $s, t$  are degree and order in spherical harmonic expansion and  $a$  the Earth's radius. The sensitivity kernel  $K_s^x$  is calculated for the reference model and depends only on the degree  $s$  of the expansion.

A first data set used 63 well constrained modes (*He and Tromp, 1996* and *Resovsky and Ritzwoller, 1998*), corrected for the contribution of the crust; tests proved that the choice of the crustal model has little impact on the correction. Another data set adds a large number of upper mantle modes (*Widmer, 2002*); these modes are less well constrained but may improve the resolution in the upper mantle.

### The Model Parameter Space

We search the degree 2 of the spherical harmonic expansion of the perturbation, with five coefficients  $C_{2,0}$ ,  $C_{2,1}$ ,  $S_{2,1}$ ,  $C_{2,2}$  and  $S_{2,2}$ . After trying various parameterizations for the radial variations of the perturbations, we selected a 7 (8 when more modes are included) cubic splines parameterization that gives naturally smooth variations.

To further reduce the number of parameters, only the shear velocity structure is fully discretized by splines. The bulk velocity and density structures are scaled to shear velocity structure with 3 scaling coefficients: lower mantle (bottom 2 splines), the middle mantle (3 splines) and one for the upper mantle (2 or 3 splines). Note that we are allowing lateral variations in the scaling coefficient as the scaling coefficients can be different for different spherical harmonic coefficients. Finally, the contribution of the topography of the CMB to the splitting of the

modes is also included. Parameter space dimension is then 14 (resp. 15).

### 0.3 Results

#### Sampling the Parameter Space

The neighborhood algorithm sampler (*Sambridge* 1999a) produces a set of models that sample the parameter space preferentially where the fit is good. Figure 37.1 shows 300 of the  $C_{2,0}$  models for an exploration with 7 splines,  $V_p$  and  $\rho$  being scaled as described previously. While most models appear similar to the best model, a secondary minimum of misfit also appears that would be missed by a least square inversion. Note how the density in the uppermost mantle is poorly constrained in this case with a broad variety of values.

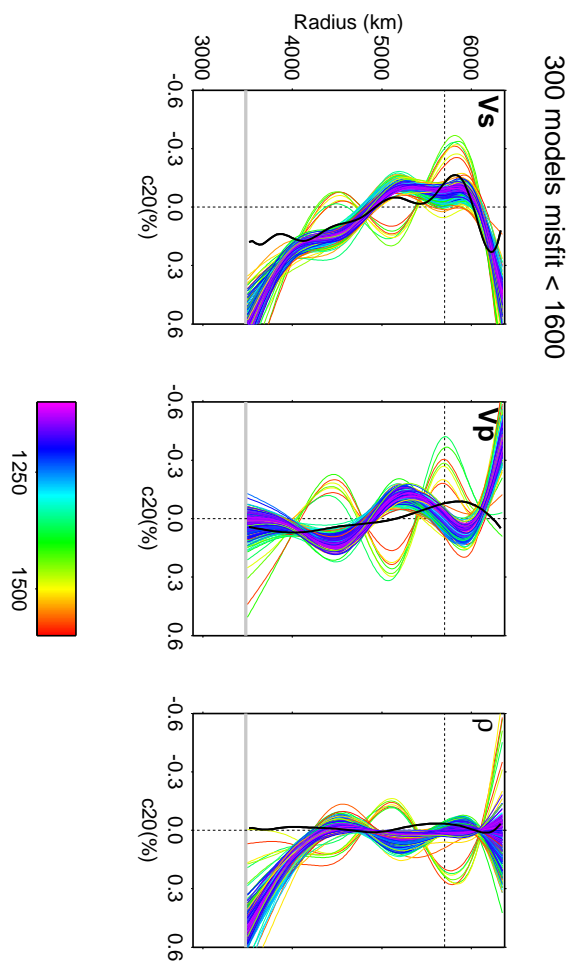


Figure 37.1: 300 good (low misfit), randomly selected  $C_{2,0}$  models. The black line in front is the SPRD6 model, color/grey is given by the misfit between synthetic coefficients and data.

#### Quantitative Results from the Bayesian Integrals

The second program, the appraiser (*Sambridge* 1999b) uses a set of models to approximate the posterior probability density in the parameter space, and computes Bayesian integrals over this approximate ppd, allowing a quantitative use of the set of models. It is then possible to get the marginal probability for each parameter - or quantities based on these parameters. Such quantities have been estimated and are shown in Figure 37.2. The spherical harmonic coefficient shown is  $S_{2,2}$ , for a parameterization with 8 splines, scaling and topography of CMB. Note how the scaling values in the middle mantle (depth range 670 to 1800 km) are more poorly constrained than values in the lowermost and upper mantle. While the average shear velocity anomaly at these depths noted  $\langle V_s \rangle_{mm}$  is well constrained, the scaling coefficient for bulk velocity anomaly  $V_p/V_s$  (for  $d(\ln V_p)/d(\ln V_s)$ ) and density  $Rho/V_s$  can take a broad range of values.

#### 0.4 Perspectives

Further work will include stability tests for the method. Preliminary tests show that the confidence intervals may not be completely reliable (!), especially for some parameters for which convergence of the Bayesian integrals is slow and/or currently insufficient. The addition of the modes of Widmer (*Widmer*, 2002) seems to help to constrain the perturbation in the upper mantle but the effect on other values remains to be investigated.

#### 0.5 Acknowledgements

Special thanks to Malcolm Sambridge for making the NA software package available. This package, its very helpful online help and a short description of the algorithm can be found at <http://rses.anu.edu.au/~malcolm/na/na/html>. Figure 37.2 was made using a plotting utility of the package.

#### 0.6 References

Giardini, D., X.D. Li and J. Woodhouse, Splitting functions of long-period normal modes of the Earth, *Jour. Geophys. Res.*, 93 B11, 1988.  
 He, X. and J. Tromp, Normal-mode constraints on the structure of the Earth, *J. Geophys. Res.*, 102, 17981-17994, 1996.  
 Ishii, M. and J. Tromp, Normal-Mode and Free-Air Gravity Constraints on Lateral Variations in Velocity and Density of Earth's Mantle, *Science*, 285, 1231-1236, 1999.  
 Kuo, C. and B. Romanowicz, On the resolution of density anomalies in the Earth's mantle using spectral fitting of normal mode data, *Geophys. J. Inter.*, in press  
 Romanowicz, B, Can we resolve 3D density heterogeneity in the lower mantle ?, *Geophys. Res. Lett.*, 28, 15, 1107-1110, 2001.

Resovsky, J. and M. Ritzwoller, Regularization uncertainty in density model estimated from normal mode data, *Geophys. Res. Lett.*, 26, 15, 2319-2322, 1999.

Resovsky, J. and M. Ritzwoller, New and refined constraints on 3D Earth structure from normal modes below 3mHz., *J. Geophys. Res.*, 103, 783-810, 1998.

Sambridge, M., Geophysical inversion with a neighborhood algorithm I - Searching a parameter space, *Geophys. J. Int.*, 138, 479-494, 1999.

Sambridge, M., Geophysical inversion with a neighborhood algorithm II - Appraising the ensemble, *Geophys. J. Int.*, 138, 727-746, 1999.

Widmer-Schmidrig, R., Application of regionalized multiplet stripping to retrieval of aspherical structure constraints, *Geophys. J. Int.*, 148, 1-18, 2002.

## 2-D Marginals

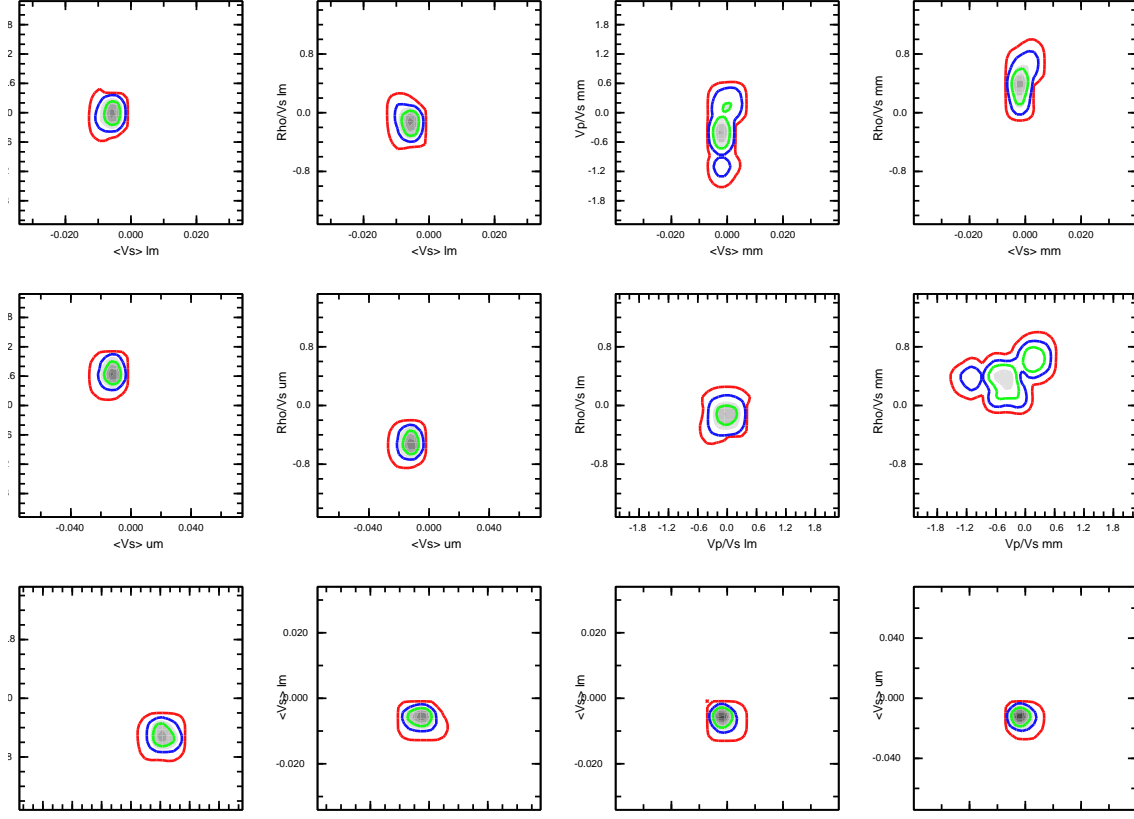


Figure 37.2: 2D marginal probabilities for the  $S_{2,2}$  anomalies. Average of the shear velocity anomaly is noted  $\langle V_s \rangle$ ; scaling coefficient from  $V_s$  to density (resp.  $V_p$ )  $\rho/\nu_s$  (resp.  $V_p/V_s$ ).  $lm$  stands for a value in the lower mantle,  $mm$  middle and  $um$  upper mantle.

## Chapter 38

# Thermochemical Convection Models of Lunar Evolution

Dave Stegman, Mark Richards, Mark Jellinek, John Baumgardner (LANL) yield a definite onset time at 4 Ga for the lunar core dynamo.

### 0.1 Introduction

We consider the early thermo-chemical history of the Moon and specifically address the question of how the Moon could have had an internally generated magnetic field suddenly 'switch-on' somewhat late in its evolution and then just as quickly 'switch-off'. It is commonly assumed the Moon never underwent mantle convection, given the majority of the surface geology is likely the original crust formed nearly simultaneous with the Moon. This can partially be explained by the fact that thermal evolution may well occur under the regime of stagnant-lid convection. Furthermore, there are a few tantalizing clues that perhaps the Moon possessed a brief, internally generated magnetic field (*Cisowski et al.*, 1983) and by implication, that the interior of the Moon was once convecting. Lunar samples returned from the Apollo missions provide a few which may contain a remnant thermal magnetism, possibly acquired during the Moon's 'magnetic era' (*Cisowski et al.*, 1983). These samples also reveal the near side of the Moon contains large areas flooded with volcanic material, the lunar mare. These mare (Latin for sea), erupted during a pulse of magmatism beginning 0.5 billion years after the Moon had formed and mostly ended after 1 billion years of activity. We have recently shown (*Stegman et al.*, 2003) that chemical overturn models suggested to explain the eruption of the Maria basalts may also account for the hitherto unexplained existence of a lunar magnetic field (core dynamo) at about the same time (3-4 billion years ago). We have chosen the approach of parallel computing to solve governing equations using the 3-D spherical finite element model (for which a considerable amount of effort was spent implementing a Lagrangian tracer algorithm). Our convection models bring together the main features of early lunar post-magma-ocean history, and carry an important testable prediction - that further analysis of

### 0.2 Generating an Early Lunar Dynamo

The Moon presently has no internally-generated magnetic field (i.e. core dynamo). However, paleomagnetic data combined with radiometric ages of Apollo samples record the existence of a magnetic field from approximately 3.9 to 3.6 Ga ('magnetic era') possibly due to an ancient lunar dynamo (*Cisowski et al.*, 1983; *Collinson*, 1993). A dynamo during this time period is difficult to explain (*Collinson*, 1993; *Stevenson*, 1983), because current thermal evolution models for the Moon (*Konrad and Spohn*, 1997) yield insufficient core heat flux to power a dynamo after 4.2 Ga. In Figure 38.1, we show that a transient increase in core heat flux following an overturn of an initially stratified lunar mantle may explain the existence and timing of an early lunar dynamo. Using a 3-D spherical convection model (*Baumgardner*, 1985), we show that a dense layer, enriched in radioactive elements ("thermal blanket"), at the base of the lunar mantle initially prevents core cooling, thereby inhibiting core convection and magnetic field generation. Subsequent radioactive heating progressively increases the buoyancy of the thermal blanket, ultimately causing it to rise back into the mantle. The removal of the thermal blanket, proposed to explain the eruption of thorium and titanium-rich lunar Mare basalts (*Hess and Parmentier*, 1995), plausibly results in a core heat flux sufficient to power a short-lived lunar dynamo.

### 0.3 Acknowledgements

We thank B. Buffett, C. Johnson, R. Jeanloz, M. Manga, and H-P. Bunge for helpful discussions. This work was supported by IGPP LANL, NASA CT project, NSF, Miller Institute for Basic Research. We dedicate this work to the memory of the late Stephen Zatman.

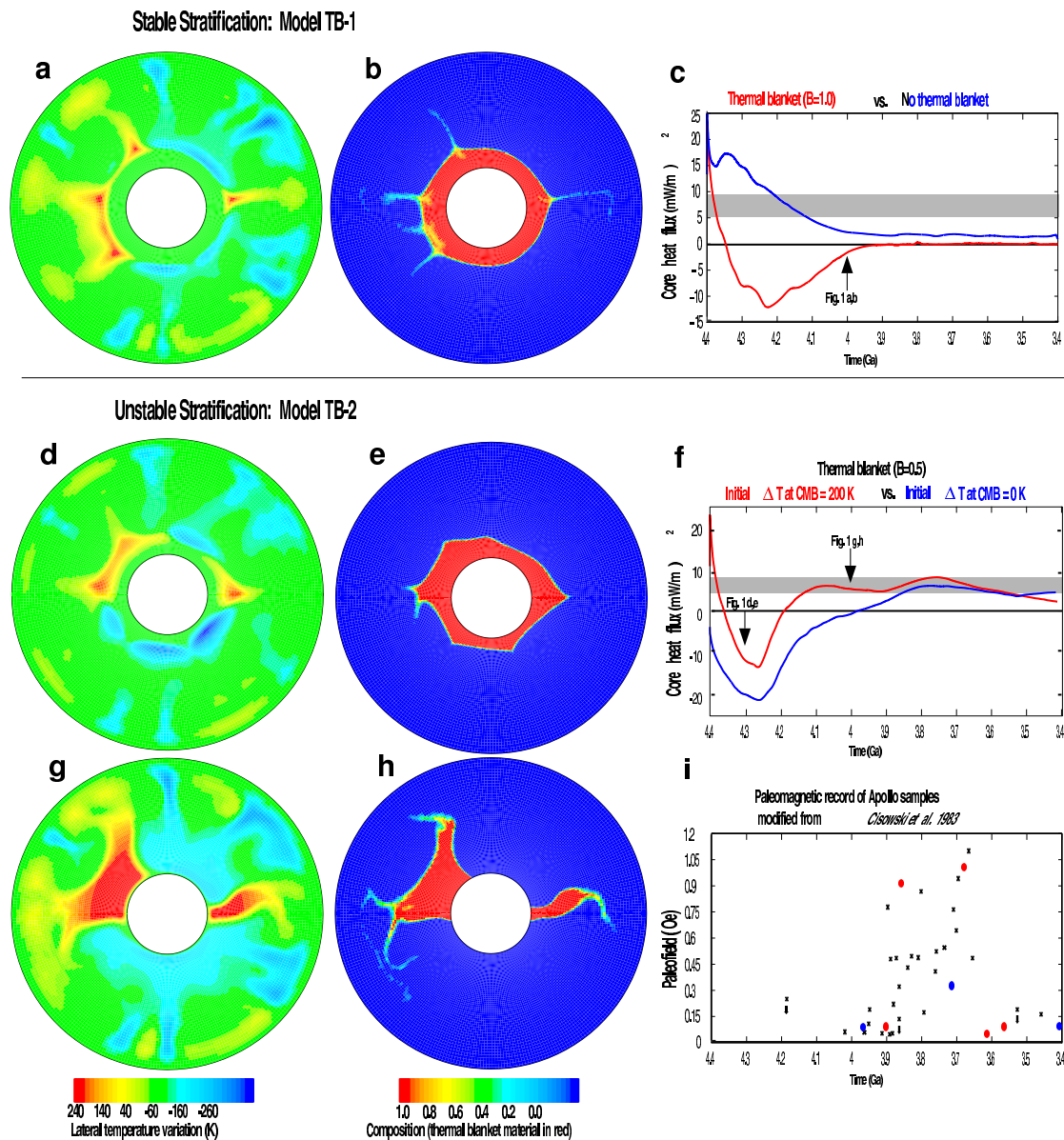


Figure 38.1: Thermochemical evolution models in stable (a-c) and unstable (d-h) thermal blanket regimes as seen in temperature (a,d,g), composition (b,e,h) and core heat flux (c,f) compared with paleomagnetic data (i). The equatorial cross-sections of (a) temperature and (b) composition for model TB-1 at 400 million years show thermal blanket material is too dense to become buoyant, but some entrainment occurs. However, equatorial cross-sections of temperature and composition for model TB-2 show a marginally stable thermal blanket interacting with mantle convection at 100 million years (d,e) and that by 400 million years (g,h) has sufficient thermal buoyancy to rise back towards lunar surface. Core thermal history (c) for reference model TB-0 shows heat flux values (blue line) well below adiabatic core heat flux (shaded region) while model TB-1 (red line) has nearly zero heat flux (black line). Such core heat flux values ranging between the black line and shaded region indicates a thermally stratified core, in which all core heat loss is by conduction and no dynamo is supported. A core heat flux equal to or above the shaded region indicates core convection and likely occurrence of a dynamo, as seen in models TB-2,3 (f). Paleointensity measurements (i) from Apollo samples (modified from Cisowski et al. 1983) where dots indicate absolute paleointensity measurements (Thellier-Thellier method in red, other techniques in blue) and crosses indicate scaled normalized relative paleointensities. In our models, asymmetric thermal blanket removal leads to a localized distribution of partially-molten thermal blanket material at relatively shallow mantle depths, confirming a plausible explanation for the eruption of high-Th, high-Ti mare basalts, similar to the models of *Zhong et al.*, 2000. Our models make no attempt to evaluate melt transport to the surface.

## 0.4 References

Collinson, D. W., Magnetism of the Moon - A lunar core dynamo or impact magnetization? *Surv. Geophys.*, *14*, 89-118, 1993.

Stevenson, D.J., Planetary magnetic fields, *Rep. Prog. Phys.*, *46*, 555-557, 1983.

Hess, P.C. and E.M. Parmentier, A model for the thermal and chemical evolution of the Moon's interior: implications for the onset of mare volcanism, *Earth Planet. Sci. Lett.*, *134*, 501-514, 1995.

Konrad, W. and T. Spohn, Thermal history of the moon - Implications for an early core dynamo and post-accretional magmatism, *Adv. Space Res.*, *19*, 1511-1521, 1997.

Baumgardner, J.R., Three dimensional treatment of convective flow in the Earth's mantle, *J. Stat. Phys.*, *39*, 501-511, 1985.

Stegman, D.R., A.M. Jellinek, S.A. Zatman, J.R. Baumgardner, and M.A. Richards, An early lunar core dynamo driven by thermochemical mantle convection, *Nature*, *421*, 143-146, 2003.

Zhong, S., E.M. Parmentier, and M.T. Zuber, A dynamic origin for the global asymmetry of lunar mare basalts, *Earth Planet. Sci. Lett.*, *177*, 131-140, 2000.

# Part IV

## Appendices

